

Symbiotic starburst-black hole AGN – I. Isothermal hydrodynamics of the mass-loaded ISM

R.J.R. Williams¹★ A.C. Baker^{2,3,4}★ & Judith J. Perry²★

¹Department of Physics and Astronomy, The University, Leeds, England LS2 9JT

²Institute of Astronomy, Madingley Road, Cambridge, England CB3 0HA

³Service d’Astrophysique, C. E. A. Saclay, Orme des Merisiers Bât. 709, F91191 Gif-sur-Yvette CEDEX, France

⁴Department of Physics and Astronomy, Cardiff University, PO Box 913, Wales CF2 3YB

Received **INSERT**; in original form **INSERT**

ABSTRACT

Compelling evidence associates the nuclei of active galaxies and massive starbursts. The symbiosis between a compact nuclear starburst stellar cluster and a massive black hole can self-consistently explain the properties of active nuclei. The young stellar cluster has a profound effect on the most important observable properties of active galaxies through its gravity, and by mass injection through stellar winds, supernovae and stellar collisions. This mass-loss, injected throughout the nucleus, creates a hot nuclear interstellar medium (nISM). The cluster both acts as an optically-thin fuel reservoir and enriches the nISM with the products of nucleosynthesis. The nISM flows under gravitational and radiative forces until it leaves the nucleus or is accreted onto the black hole or accretion disc.

The radiative force exerted by the black hole–accretion disc radiation field is not spherically symmetric. This results in complex flows in which regions of inflow can coexist with high Mach number outflowing winds and hydrodynamic jets. We present two-dimensional hydrodynamic models of such nISM flows, which are highly complex and time variable. Shocked shells, jets and explosive bubbles are produced, with bipolar winds driving out from the nucleus. Our results graphically illustrate why broad emission line studies have consistently failed to identify any simple, global flow geometry. The real structure of the flows is *inevitably* yet more complex.

The structure of these nISM flows is principally determined by two dimensionless quantities. The first is the magnitude of the stellar cluster velocity dispersion relative to the sound speed in the nISM. These speeds measure the gravitational and thermal energies in the nISM respectively, and, therefore, whether the gas is initially bound, or escapes in a thermal wind. The second parameter is the Mach number of the ill-collimated nISM flow which is driven away from the central black hole. We discuss a two-parameter classification based on this observation which, in future papers, we will relate to empirical classifications.

The interplay between the nucleus and the wider galaxy depends critically on the exchange of radiative *and* mechanical energy. The outbound mechanical energy transfer is governed by the nuclear stellar cluster. Active galactic nuclei will only be understood once the symbiotic relationships between the black hole, the stellar cluster, and the galaxy are considered. It is impossible to treat correctly any isolated component. Our conceptually simple and self-consistent *Symbiotic Model* explains the observed complexity of active galaxies without *ad hoc* measures.

Key words: galaxies: nuclei – galaxies: starburst – galaxies: active – shocks: radiative

1 INTRODUCTION

★ E-mail: rjrw@ast.leeds.ac.uk (RJRW), a.baker@astro.cf.ac.uk (ACB), jjp@ast.cam.ac.uk (JJP)

There is strong evidence for black holes with a wide range in mass in the centres of galaxies, and unambiguous evidence

for dense stellar clusters in galactic cores. Activity in the nuclei of galaxies appears to be intimately linked not only to these supermassive black holes (BH) and nuclear starbursts, but also to interactions between galaxies. The evidence for this link – both direct and circumstantial – has been reviewed in detail by Perry (1993a, 1999; see also Filippenko 1992). The exact nature of the link remains uncertain: interactions, starbursts and activity certainly can not be equated, and not all systems with these components are active. In particular, galactic interactions do not always result in activity (Sanders & Mirabel 1996). However, the evidence does unequivocally demonstrate that the active nucleus is *not* a ‘parasite’ upon a ‘host’ galaxy, but rather that activity is a galaxy-wide phenomenon which is most clearly identified by the dramatic events in the galaxy nucleus. In this paper, we consider the hydrodynamics of this basic nuclear system.

The most dramatic of the nuclear phenomena is the highly luminous (10^{10} to $10^{14} L_\odot$), time-variable, broad-band (radio to γ -ray) radiation emitted from regions as small as a few light-seconds. This radiation is accompanied in many AGN by broad emission lines from heavy elements in cold ($\approx 10^4$ K) dense ($\approx 10^9$ to 10^{12} cm^{-3}) gas. In the unified model of active nuclei, the broad line region is a constituent of all active nuclei, although it is not observed in some as a result of continuum beaming or intervening obscuration (Krolik & Begelman 1986; Barthel 1989). Line widths, which reflect local gas velocities, are typically several 10^3 km s^{-1} . Average equivalent widths are remarkably consistent across orders of magnitude differences in total bolometric luminosity (although with a marked scatter between individual objects at a given luminosity), indicating a tight relationship between the production of cold, condensed radiating gas structures and the production of the central luminosity itself.

Although accretion onto black holes seems clearly to dominate the physics of the innermost regions of AGN (within ~ 100 Schwarzschild radii), and to provide a satisfying explanation of the radiation processes which create the luminous broad-band continuum, pure black hole accretion models have always suffered from an inability to explain the structure of the line emitting regions and had great difficulty in explaining the fuelling, before the importance of stars in the wider parsec sized core was recognised.

The stars which play the dominant role in the energetics and mass budget of galactic nuclei are young, mass-losing stars: these are most abundant and important in just those nuclear stellar clusters – starbursts – which are thought to be involved in activity. Current theoretical models linking activity and starbursts come in two variants. In this paper, we explore the structure of the model (Perry 1992) based on the early work of Perry & Dyson (1985, hereafter PD) which unites starbursts and black holes as compact symbiotic systems in the nuclei of active galaxies (Collin-Souffrin et al. 1988, hereafter CDMP; Norman & Scoville 1988; Perry 1992; Williams & Perry 1994). In contrast, the pure starburst model equates the two phenomena, considering AGN to be but extreme examples of nuclear starbursts (Terlevich 1990; Cid Fernandes 1997). Interestingly, radiative shocks around supernovae play a central rôle in both theories. We shall refer to the starburst-black hole paradigm for AGN as the Symbiotic Model.

Since powerful winds and supernovae dominate the en-

ergetics of starbursts, understanding the dynamic link between black holes and starbursts requires careful analysis of the stellar- and hydro-dynamics of the combined system. In this paper we present the first comprehensive treatment of the hydrodynamics of such a symbiotic system.

In the rest of this introduction, we outline the physical context and assumptions of our model. These assumptions will be discussed in more detail in subsequent sections.

1.1 Symbiotic models

In the Symbiotic Model of AGN, the nuclear starburst stellar cluster feeds the black hole through the nuclear interstellar medium (nISM) created by stellar mass-loss. The formation of shocks within the nISM is an *inescapable* consequence of the interaction between individual (mass-loading) stars and the global nISM. It is important to emphasise that the presence of shocks in the nISM is a model independent phenomenon and is a direct consequence of basic thermodynamics, stellar dynamics and hydrodynamics in galactic nuclei. In QSOs, the shocks around individual supernovae are sufficiently large that the shocked nISM gas has time to cool radiatively into thermal equilibrium with the central radiation field at $\approx 10^4$ K, so forming broad line emitting structures (PD). The thermal pressure in such shock confined structures equals the stagnation pressure of the flow, which agrees well with the pressures deduced from observations of the emission lines. PD showed that using the observed equivalent widths of the high-ionization lines (HILs) to deduce the average properties of the nISM, the implied flow rates in the nISM are sufficient to fuel the black hole accretion.

This satisfyingly self-consistent picture did not initially explain the two-(or more)-component nature of the broad emission line region (BELR): the low-ionization lines (LILs) are observed to be both red-shifted with respect to the HILs, and to require a harder ionizing continuum. However, CDMP then showed that the nISM flow can back-scatter X-rays which provide ‘deep heating’ of the accretion disc sufficient to produce the LILs. This two-component model resolved several outstanding questions concerning the BELR. The transient nature of the BELR clouds solved the ‘cloud confinement problem’. The existence of two distinct regions of broad line emission also gave a simple explanation for the observed systematic velocity shifts and multiple component structure of the broad line profiles (Corbin & Francis 1994; Brotherton et al. 1994; Arav et al. 1998). Our results, in this paper, add another dimension to this understanding of the structure of the BELR: we find that the nISM itself forms distinct multi-component regions of differing characteristic excitation levels and velocities.

The structure of the emission line region which emerges is that of distinct local clumps of line-emitting gas confined by transient shocks. Recently, Arav et al. used the new generation of observations to update the limits which smooth line profiles put on the number of such centres of emission (e.g. Atwood, Baldwin & Carswell 1982). Their analysis was based on the fact that discrete emitting units give a smooth line profile only when the number of emitting units is very large. Their method is sensitive to structures with velocity widths between 50 and 200 km s^{-1} ; within this range they find essentially no perturbations in the wings of the Balmer lines, to very tight limits. This rules out many of

the simplest scenarios for the formation of the lines by discrete clumps. Arav et al. were able to rule out emission from less than 3×10^6 smooth shell sources with expansion velocity 100 km s^{-1} . However, such sources, with small velocity width and perfect symmetry, are not representative of shock-confined emission line clouds in galactic nuclei. Structures which are intrinsically smoother in emission than those they specifically considered, such as accretion discs (which are thought on other grounds to be important contributors to the Balmer emission, CDMP), or strong wind sources and bowshocks ($v \gtrsim 200 \text{ km s}^{-1}$) are not ruled out by these observations. The sonic velocity in the nISM is at least 400 km s^{-1} ; this is the minimum expected shock velocity in the region. In fact, characteristic velocities of the shocks which arise in symbiotic nuclei are $\times 10^3 \text{ km s}^{-1}$ [the combination of stellar ejection velocities (often $\gtrsim 3 \times 10^3 \text{ km s}^{-1}$) and the stellar orbital velocities ($\gtrsim 600 \text{ km s}^{-1}$ within the central parsec)]. Furthermore, the shocks are non-uniform: they are either open bow shocks with streaming tails, or closed shells distorted by their interaction with the wind. The density, radial velocity and surface emissivity – for any shock – all vary significantly around the shock-front, generating broad, complex lines with wings which are much less steep than those Arav et al. assumed. As Arav et al. pointed out, any flow which produces smoothly varying structures on velocity scales of $500 - 1000 \text{ km s}^{-1}$ is allowed by the observations. We therefore conclude that their elegant analysis provides support for the PD model, and underlines the importance of hydrodynamic models of the BELR.

1.2 Physical Ingredients

The physical parameters characterising the centre of a galaxy are the mass of the black hole, and the mass, stellar density profile, IMF and age of the stellar cluster. The IMF and age govern the mass-loss rate from stars due to stellar evolution; collisions and tidal disruption are negligible except in the central regions of the densest clusters. The mass lost from the stars inevitably creates a nuclear interstellar medium (nISM). If there is a black hole accretion flow, either from this nISM or from some other reservoir (e.g. flow into the nucleus from a galactic bar), then radiation processes near the black hole can generate a powerful broad-band continuum (although not if the flow into the black hole is hot or optically thick (Narayan & Yi 1994; Blandford & Begelman 1999)). For the present, we take this as an additional input to our simulations. The system which we consider in this paper is one in which such accretion processes are effective.

The stellar cluster surrounding the black hole helps to determine the structure of the nISM flow on the scale of the BELR, through gravity and distributed stellar mass loss. The strength of this mass-loading is principally determined by the age and initial mass function (IMF) of the stellar cluster. We shall assume that the cluster is young and dominated by high mass stars, and take our basic parameters from the stellar synthesis models of Williams and Perry (1994).

Mass input from the stellar cluster is discrete and local. Because we are interested in the generic properties of the global flows, we will concentrate on the luminous QSOs. In such models, the mass processing rates are high enough that we can average over the numerous small scale structures resulting from the interaction between individual stars and

supernovae with the global flow. Future papers will investigate the detailed structure of individual mass input sources, and the effects of the discrete mass input on the global flow.

We have focussed on mass injection from stars within the cluster rather than from the external ISM, primarily for two reasons. Importantly, the mass flux from the external ISM is unlikely to be able to provide a significant fraction of the fuelling requirements of the AGN as a continuous source (Shlosman et al. 1990). The wind from the nucleus is in some cases strong enough to drive the external ISM away. Also, this is the situation described in PD, where the shocks around the mass-loading centres also generate the cool gas which emits the observed emission lines. Therefore, rather than include the additional free parameters specifying the distribution of the ambient ISM at the outer boundary of our models in this first paper, we have chosen to concentrate on the case where the phase of accretion from tens or hundreds of parsecs to within a parsec of the central black hole has already ceased.

We have assumed that any relativistic jet driven from close to the central black hole is absent, or at least narrow, transferring little momentum to the surrounding global flow. If this assumption is reasonable, our models apply equally to radio-loud and radio-quiet objects. Radio structures on parsec scales are seen in radio-quiet objects as well as radio-loud ones: the explicit inclusion of jets in our models would be an interesting extension.

1.3 Formation scenarios

The starburst-black hole system is in a symbiotic relationship with the wider galaxy. We study the structure of the nuclear system in its active phase in this paper. We leave the vexed questions of the formation of the nuclear system and the details of its symbiosis with the wider galaxy to later work. This follows the tradition well established in stellar physics: first understand structure, then evolution, lastly formation. Nonetheless, there are clear indications, both from observations and from theory, of possible formation scenarios (Perry 1999). Interactions between galaxies disturb the equilibrium of the ISM of the galaxies, and gas can flow towards the nucleus where it can form a nuclear starburst. The size scale of the starburst depends on whether the gas can shed its angular momentum, and on whether it hangs up at a Lindblad resonance (Lamb 1999).

Direct optical imaging of galaxies with bright active nuclei is difficult, but HST and near-IR imaging are now revealing the morphological types (Dunlop et al. 1993; McLeod & Rieke 1994a; 1994b; Taylor et al. 1996; Bahcall, Kirhakos & Schneider 1997; Boyce 1997; McLeod 1997). Radio and quasar galaxies appear to be large and luminous, and to show signs of past merger events. Galaxies with radio-loud active nuclei are essentially all spheroidal, whereas those with radio-quiet cores are approximately equally divided between spheroidal and disc-dominated structures (Kukula et al. 1997a). This may indicate e.g. different interaction histories for radio-loud and radio-quiet systems.

There is much circumstantial evidence that similar environmental factors influence the frequency of both active nuclei and starburst galaxies (Neff & Hutchings 1992). Cooling flows around massive elliptical galaxies may provide a source of fuel for both phenomena (Binney & Tabor 1995;

Ciotti & Ostriker 1997; Bremer, Fabian & Crawford 1997; Friaça & Terlevich 1998). Ultraluminous IR galaxies may represent a transition phase as dense shrouds of dust lift to reveal bright optical quasar nuclei, since the environments, molecular gas content, near-IR colours and optical emission line diagnostics of the two classes are similar (Sanders et al. 1988). Processed material with near-solar metallicities in the nISM is seen in AGN even at the highest redshifts. At redshifts $2 < z < 3$, absorption line studies reveal that most of the gas in galaxies typically has $Z/Z_{\odot} \approx 0.01\text{--}0.1$ (Pettini et al. 1994; 1997). To reach the high metal abundances observed in QSOs after short cosmic times, massive star formation, probably *in situ*, must be intimately linked to the evolution of active galaxies (Perry 1992; Ferland et al. 1996; Korista et al. 1996). Populations of star-forming galaxies at $z \sim 3$ have now been discovered (Steidel et al. 1996). This redshift range is hence a critical period in the evolution of both normal and quasar galaxy populations (McLeod 1997).

Whatever the likely formation scenario, the nISM in our models reaches a structure characteristic of its long term behaviour – equilibrium, oscillations or explosions – on dynamical timescales typically a few thousand years. These timescales are much shorter than any plausible formation or evolution times (Williams & Perry 1994), and so we treat the structure of the system independently from its formation and evolution.

1.4 Hydrodynamics of the nISM

Our aim in this paper is to explore the hydrodynamics of those nuclear black-hole/stellar cluster systems which *are* active. Williams (1999) summarises previous hydrodynamic models of the flow structure of active nuclei. Our study is unique in that it treats the distributed mass input through the nucleus and the gravitational field of the stellar cluster.

We treat the global hydrodynamics of the nISM, as it interacts with the central black hole, the stellar cluster and the accretion disc. These physical components are essential to the starburst-black hole model of AGN – and to most other dynamical models of active nuclei. We have chosen to simplify the properties of this system as far as possible. This approach allows us focus on the most important properties of the global hydrodynamic interactions between stellar cluster, black hole and accretion disc.

Independent of the detailed model, it is possible to estimate characteristic values of the flow density and velocity required for the accreting nISM flow to be able to fuel the AGN. PD used such simple scaling arguments to discuss the structure of the nISM flow, and to investigate the consequences for the fuelling of AGN and for the creation of the BELR. If the local nISM is too dense, it obscures the system; if it is too diffuse, it fails to provide the necessary fuel for the AGN. Those flows consistent with these constraints can be shown to have ram pressures similar to the pressures deduced from observations of the broad line clouds. The ram pressure of the nISM will therefore have an important dynamical effect on the BELR clouds, whatever their confinement mechanism. Although these simple arguments provide interesting overall constraints, many important properties of the AGN depend on the structure of the flow, which PD did not address. Detailed hydrodynamic modelling is necessary to determine these flow structures. More broadly, it

is clearly necessary to consider the hydrodynamics of the nISM in order to develop fully *any* model of AGN.

In the absence of a black hole, in a dense stellar cluster with negligible external pressure, gas accretes onto a hydrostatic core, and a weak wind forms (cf. Section 5). The core grows until it reaches the sonic radius, and the wind from the cluster increases to an equilibrium in which it transports the mass injection from the stellar cluster out into the wider galaxy. Once a black hole is added to the system, with an accretion-generated radiation field, many more complex behaviours can occur, some of which we investigate in this paper. Broadly, however, the black hole can accrete matter at the centre of the flow, weakening the eventual wind, and the radiation field may drive it away. In the absence of radiative driving, the sonic (or Parker) radius is $GM/2c_s^2 = 1.4\text{ pc}$ for a $10^8 M_{\odot}$ BH mass and gas at a temperature of 10^7 K , which is at least as large as the broad emission line region even in QSOs. The velocities in pure thermally driven winds only reach $\sim 360\text{ km s}^{-1}$ (the sound speed in the nISM) at such radii. Such low velocities are in conflict with the strong evidence for outflowing gas in and around AGN at far higher velocities, most clearly in broad absorption line QSOs (Turnshek 1988; Osterbrock 1991). If radiative driving occurs at all angles, then the hole may well be starved of fuel. This will reduce the luminosity, giving rise to a limiting feedback process. However, there is strong evidence of beaming in all AGN. This asymmetry in the radiation field means that the radiation force can be greater than the gravitational attraction of the black hole on the axis of the accretion disc, but not in its plane. In such cases, mass can fall inwards towards the plane and be driven away on axis. Such flows are typical of our simulations.

The structures and the global kinematics of these nISM flows are likely to be generic features. However, we will see that small-scale features such as gas cooling may play an important role in determining the *observable* properties of the flow. Where cooling is significant, the average opacity of the gas will be increased, which will re-scale the importance of the central radiation field. The central broad-band (radio to X- and γ -rays) radiation field is powered by mass accretion through a disc and down into the black hole. We model this radiation field as the sum of an unresolved point source and an accretion disc component which follows a simple cosine law. We concentrate on models appropriate to QSOs, since there is wide agreement that they accrete at or near the Eddington limit. In contrast, the lower luminosity Seyferts appear to span a much wider range in mass-to-light ratio. We discuss the consequences of scaling our models to Seyfert properties in Section 6.5.

Because we do not model the accretion disc explicitly, the effective Eddington ratio, f_{Edd} , is an arbitrary input parameter. A goal of future research is to determine the relationship between f_{Edd} and the properties of the nISM, since this must be self-consistent (i.e., the accretion rate onto the central black hole must be sufficient to power the luminosity of the AGN). The characteristics of the disc should be determined by the rest of the nuclear system. Although f_{Edd} changes on timescales much shorter than the evolution of the overall system, these are much longer than the dynamic timescales of the nISM. It is not currently feasible to determine f_{Edd} by modelling the disc and nISM simultaneously. We have chosen a simplified parameterisation so we can, to

first order, rescale f_{Edd} , (see Section 2.2). The rescaled solutions will have the same global properties as the real flows. Subsequent papers will fill in the important details in this picture.

The flows in individual simulations are complex and varied, whilst exhibiting a generic bipolar circulation pattern. These results suggest why over 30 years of careful and detailed BELR observations and simulations have failed to identify a simple, global flow geometry. If anything, real flows will be more complex, not simpler, than the flows we find here.

These generic bipolar flow patterns are characterised by both an accretion inflow and a wind outflow in the nISM. The gas which accretes can generate the luminosity assumed by the flow models. Bipolar outflows – and even hydrodynamical jets – are generated, so long as there is sufficient outward force along the accretion disc axis. These structures will be found independent of whether the nuclei are radio-loud or radio-quiet: they are in general less collimated and lower velocity than the most dramatic radio structures observed, although when a plume of gas escapes the nucleus it may be observable as a radio structure.

The strength and structure of these flows depends primarily on the ratio of the gravitational and thermal energies in the nISM. Some of the inflowing gas is driven away into the wider galaxy, while some may accrete onto the black hole. The wind expelled from the nucleus can carry both significant mechanical energy and heavy elements into the wider galaxy. Thus, the nISM flows will affect significantly the structure of the ISM of the galaxy. At early times, the flows will enrich the galaxy ISM and may drive shocks and shells of gas out to distances of kiloparsecs (Beltrametti & Perry 1980; Dyson, Falle & Perry 1981; Falle, Perry & Dyson 1981; Silk & Perry 1999).

These nISM flows can only be observed indirectly. The nISM itself is hot – typically $\sim 10^7$ K, the Compton temperature characteristic of the central radiation field – and does not give rise to observable line radiation, although limits on its column density are set by Thomson optical depths. The BELR is formed within the nISM, and so the broad line profiles will reflect the nISM velocities as well as the stellar orbital velocities. If the BELR is formed behind shocks driven by the stars as they move through the nISM (as in the models of PD) then the characteristic velocities of the line emitting material will be determined by stellar orbital, stellar mass-ejection and nISM velocities. The stellar velocities will broaden the nISM contribution to the line widths, but the fundamental shape and asymmetries of the lines will reflect the nISM flows. Empirical models of such profiles (Albertsson & Perry 1999) show most of the characteristics of observed line profiles and their diversity. In this paper, we study the flow structures which underly the structures determined by such empirical studies.

We find that we can characterise the structure of the nuclear interstellar flows on a two-dimensional plot. This is our first step in developing a theoretical diagnostic diagram for AGN flows, analogous to the Hertzsprung-Russell diagram which provides a systematic understanding of stellar structure. Stellar spectral type, luminosity, colour and temperature – characteristics which are determined by the basic physical parameters of age, metallicity and mass – are used as the axes of the HR diagram. Similarly, the axes of

our plot can be expressed in a number of ways. Although it would be desirable to use the fundamental physical parameters listed above as the axes, we find that the most natural variables are derived parameters which are closely related to the underlying physics (see Section 3.4).

1.5 Scope and layout

We present numerical models of cylindrically symmetric, isothermal flows in black hole-starburst AGN. We have used global assumptions which are physically justifiable for QSOs. Various local deviations from those global approximations will be examined in detail in a future paper.

In Section 2, we specify the parameters of the physical model of a supermassive black hole and a starburst stellar cluster. In Section 3, we give the hydrodynamical equations and discuss their scaling behaviour and their relationships to AGN observation. We also introduce the reduced set of dimensionless parameters with which we describe the gross features of the flows, to serve as a guide to the numerical models which follow. The numerical methods used to implement the hydrodynamic representation of our physical model are outlined in Section 4. We then describe the results of our detailed modelling. First, in Section 5, we describe results for purely spherical flows. We verify that our methods reproduce the analytic results, and summarise the general properties of such flows, and those described in the literature. Next, in Section 6, we present the results from our aspherical models, calculated for parameters appropriate for luminous QSOs. In Section 6.5, we discuss models where the Eddington ratio is very small, as is suggested to occur in some Seyfert galaxies. In Section 7, we discuss these results and their physical implications in the context of the current observational and theoretical understanding of activity in galactic nuclei. We compare our results with the models of the flow structure in active nuclei of PD and Perry (1993a). We sketch the global constraints on the models. Readers who are most interested in the observational consequences of our work, and ways in which our model can be tested, could now turn straight to the figures in Section 6 and then read Section 7, where we show that the symbiosis between a nuclear starburst stellar cluster and a supermassive accreting black hole, via the nISM, provides a self-consistent model for nuclear activity in galaxies. In Section 8, we draw together our conclusions.

Illustrative animations are available at
<http://ast.leeds.ac.uk/~rjrw/agn.html>.

2 PHYSICAL STRUCTURE OF THE ACTIVE REGION

We model the nuclear system of an active galaxy as an accreting supermassive black hole, a dense starburst stellar cluster, and the resulting hot, flowing interstellar medium. In principle, mass, momentum and angular momentum will be exchanged across the interface between the active nuclear region (radius ~ 1 pc) which we explicitly model, and the wider galaxy. In Section 2.1, we discuss the theoretical and observational timescales which characterise our model. These determine the physical effects which dominate the structure of the hot phase flows. We define the parameters

Table 1. Glossary of non-standard symbols and abbreviations widely used in the text.

Symbol	Description
BELR	Broad emission line region
c_s	Sound speed in the nISM
f_{disc}	Fraction of luminosity in accretion disc (anisotropic) component
$f_{\text{Edd}}(\theta)$	Ratio of outward radiative force (from Thomson scattering) to inward gravity of the black hole
$\langle f_{\text{Edd}} \rangle$	Angle average of f_{Edd} , cf. eq. (A8)
$\bar{f}(\theta)$	Form function for f_{Edd} , so $f_{\text{Edd}}(\theta) = \langle f_{\text{Edd}} \rangle \bar{f}(\theta)$
g, \mathbf{g}	Body-force acceleration (gravity and radiation)
h	Index of stellar distribution in stellar cluster halo, cf. eq. (2)
H	Thickness of accretion disc
L_{Bol}, L_{46}	Accretion-generated bolometric luminosity of the BH, $L_{\text{Bol}}/10^{46} \text{ erg s}^{-1}$
L_{disc}	Accretion disc (anisotropic) component of L_{Bol}
L_{Edd}	Eddington luminosity of the black hole
\mathcal{M}	Flow Mach number
\dot{M}_a	Rate of accretion of mass onto black hole
M_c	Mass of stellar cluster within r_c (core mass)
$M_{\text{cl}}, M_{\text{cl},8}$	Total mass of the stellar cluster, $M_{\text{cl}}/10^8 \text{ M}_\odot$
$M_h, M_{h,8}$	Mass of the black hole, $M_h/10^8 \text{ M}_\odot$
m_l	Low mass cut-off for stellar cluster IMF
M_\star	Mass of an individual star
nISM	Nuclear interstellar medium
$n_*(r)$	Radial star number density of stellar cluster
n_c	Star number density at edge of stellar cluster core
n	Total particle density
Q, Q_{-8}	Rate of mass-loading from stellar cluster as a fraction of stellar density, $Q/10^{-8} \text{ yr}^{-1}$
$\dot{q}(r)$	Mass loading rate
$\dot{q}_c, \tilde{\dot{q}}(r/r_c)$	Mass loading rate in the core, variation of mass loading scaled to this value
r_c	Radius of stellar cluster core
r_s	Sonic radius (for spherical models)
R_\star	Radius of an individual star
R	Radius of accretion disc
s	Index of stellar distribution in stellar cluster core
t_C	Compton timescale at constant volume
T_4	Temperature $T/10^4 \text{ K}$
$T_{\text{C}}, T_{\text{C},7}$	Compton temperature, $T_{\text{C}}/10^7 \text{ K}$
v_K	Keplerian velocity (of circular stellar orbit) at cluster edge
v_\star	Escape speed from individual star
η_{acc}	Accretion efficiency factor
λ	Dimensionless length scaling parameter
μ_{acc}	Fraction of stellar mass loss accreted by BH
$\mu_*(r/r_c)$	Stellar mass enclosed with r as a fraction of total cluster mass
$\rho_*(r), \bar{\rho}_*(r/r_c)$	Radial mass density of stellar cluster
$\rho_{\star,c}$	Mass density of stellar cluster core
σ	Velocity dispersion of the stars in the stellar cluster
τ	Dimensionless time scaling parameter
τ_f	nISM characteristic flow timescale, $\sim 10^{10}-10^{12} \text{ s}$
τ_{coll}	Stellar collision time
τ_{dyn}	Cluster dynamical timescale, i.e. r_c/v_K
τ_\star	Characteristic stellar lifetime
Ξ	Ionization parameter
ϕ	Dimensionless mass-input scaling parameter

of our model in Section 2.2, and describe our treatment of the interfaces between the flow and the accretion disc, a possible nuclear jet and the surrounding galaxy in Section 2.3. We provide a more detailed physical and observational background to our assumptions in Appendix A.

Table 1 is a glossary of non-standard symbols and abbreviations widely used in the text.

2.1 Timescales

We shall concentrate on global nuclear interstellar medium (nISM) flows, which have characteristic timescales $\tau_f \sim 10^{10}-10^{12} \text{ s}$, and on their response to global gravitational and radiative forces. In this regime, cooling timescales are short enough that the gas can be taken as in equilibrium. By comparison, relative timescales $\gtrsim 10^4$ times larger are inferred for large-scale radio structures. In Table 2, we compare various physical timescales relevant to flows in AGN.

Dynamical evolution timescales are long enough that

Table 2. Approximate physical timescales.

Property	Timescale (10^{10} s)	Scaling ^a	
		Physical	(λ, τ, ϕ)
Stellar collisions ^b	3×10^7	$r_{\text{pc}}^{7/2} M_{\text{cl},8}^{-3/2}$	$\lambda^{-1} \tau^3$
Stellar relaxation in nucleus	1.6×10^7	$r_{\text{pc}}^{3/2} M_{\text{cl},8}^{1/2} M_{\star,\odot}^{-1}$	$\lambda^3 \tau^{-1}$
Galaxy interactions	3×10^5
Stellar evolution	3×10^5	Q_{-8}^{-1}	ϕ^{-1}
Disc viscosity ^c	2×10^4	$\alpha^{-1} M_{\text{h},8}^{1/2} r_{\text{pc}}^{1/2} T_{\text{d},4}^{-1}$	$\lambda^2 \tau^{-1}$
Orbital timescale	30	$r_{\text{pc}}^{3/2} M_{\text{cl},8}^{-1/2}$	τ
Global sound crossing time	10	$r_{\text{pc}} T_7^{-1/2}$	τ
Flow time	1	$r_{\text{pc}} (v/0.01c)^{-1}$	τ
Supernova evolution	0.2	$n_4^{-1/3} (v_{\text{SN}}/0.01c)^{-1}$	$\tau^{1/3} \phi^{-1/3}$
Post-shock cooling ^d	0.2	$p_{s,14}^{-1}$	$\lambda^{-2} \tau^3 \phi^{-1}$
Compton cooling	0.1	$r_{\text{pc}}^2 L_{46}^{-1}$	$\lambda^{-1} \tau^2$
Supernova frequency	0.03	$Q_{-8}^{-1} M_{\text{cl},8}^{-1}$	$\lambda^{-3} \tau^2 \phi^{-1}$
Cloud sound crossing	10^{-3}	$(d/10^{13} \text{ cm}) T_4^{-1/2}$...
Hot-phase ion collisions	10^{-4}	$T_7^{3/2} n_4^{-1}$	$\lambda^3 \tau^{-2} \phi^{-1}$
Cool-phase recombination	3×10^{-7}	n_9^{-1}	$\lambda^{-2} \tau^3 \phi^{-1}$

^a Variation of timescale with (λ, τ, ϕ) , assuming all dimensionless parameters (e.g. nuclear spectrum, Eddington ratios) and ‘microphysical’ values (e.g. cool phase temperature) are constant.

^b e.g. Perry & Williams (1993), assuming the stellar cluster dominates the gravitating mass.

^c $\alpha \lesssim 1$ is the Shakura-Sunyaev (1973) viscosity parameter, $T_{\text{d},4}$ is the temperature of the disc gas in 10^4 K (see also Shlosman, Begelman & Frank 1990).

^d Applies if post-shock cooling is dominated by bremsstrahlung cooling from 10^8 K – for shock temperatures smaller than this, there is an extra factor $T^{1/2} \equiv \lambda/\tau$.

the hydrodynamics is insensitive to secular changes in the gravitating mass distribution, although the details of the mass loading do depend on the secular evolution of the cluster (MCD; Murphy & Perry 1999). Stellar collisions, dynamical relaxation, galaxy interactions, stellar evolution and disc viscosity all have characteristic timescales far longer than the flow time through the nucleus. These processes are all important in determining the secular evolution of the nucleus. Integrated over the nucleus, mass loss due to passive stellar evolution dominates that due to collisions for all but the densest ($\gtrsim 10^9 M_{\odot} \text{ pc}^{-3}$) and most massive clusters. Mass loss due to relaxation of stars into the loss cone of plunging orbits are always insignificant. If the cluster IMF extends well below $1 M_{\odot}$, collisions can dominate mass input very close to the black hole (Murphy & Perry 1999). Hence, if low luminosity AGN are characterised by small, centrally condensed starburst stellar clusters mixed in a massive old cluster, stellar collisions may dominate stellar evolution as the mechanism for mass loss in such objects (cf. MCD; Williams & Perry 1994; Murphy & Perry 1999).

The similarity of the timescales for galaxy interactions and stellar evolution suggest that star formation will be important through much of the life of the active nucleus. However, threshold processes operating at intermediate scales within the galaxy may serve to reduce substantially the timescales which characterise the periods of mass input to the nucleus. The accretion disc viscous timescale is far longer than the dynamical timescale of the hot phase flow, even in the very central regions, $\sim 10^{-3}$ pc, where temperatures reach 3×10^4 K (eqs A9, A10). We expect that the hot phase

gas will add to the disc at radii significantly outside 10^{-3} pc, so the feedback between flow and central luminosity will have a very long delay (roughly 10^3 times the flow time, Table 2). This justifies our approach of calculating the flow structure for an applied central luminosity rather than attempting to find fully self-consistent solutions.

Small timescale variability is most often measured in relatively low-luminosity Seyfert galaxies. Typical values are $10^{-6} \tau_f$ for continuum variability in X-rays, $\gtrsim 10^{-6} \tau_f$ for the UV continuum and $\gtrsim 10^{-4} \tau_f$ for the optical continuum in Seyferts, which are both believed to be driven by the high energy source (e.g. Edelson et al. 1996). Variations of 10 per cent in QSOs are found over timescales of $10^{-2} \tau_f$ (Hook et al. 1994). In Seyfert galaxies, optical-UV emission lines also vary on a $\gtrsim 10^{-4} \tau_f$ timescale, with evidence for evolution of the distribution of line-emitting gas over a $10^{-2} \tau_f$ timescale (Perry, van Groningen & Wanders 1994; Wanders & Peterson 1996). The flow will be perturbed by sound waves driven by short timescale variations in radiation forces. The steady luminosity we assume here may be taken as a time-average, which we assume drives a ‘averaged’ flow.

The thermal evolution of the nISM may affect the flow at the 10 per cent level. This may be qualitatively important if instabilities result. The timescale for evolution of supernovae is comparable to the flow timescales, and so may be significant – individual supernova events can significantly perturb the flow, particularly in lower-luminosity nuclei (Perry, Williams & Dyson 1999). The short timescale for hot phase collisions is a necessary (if not sufficient) condition for our use of single-temperature hydrodynamics; the

timescales for sound to cross clouds and for recombination suggest that the hot phase may be taken as a steady background in cloud structure problems.

As we shall see (Section 6), some flows seem to reach no equilibrium, undergoing a chaotic sequence of explosions or large magnitude oscillations; others seem to be steady on a dynamical timescale, but can take far longer than this to reach equilibrium. Flows with the latter behaviour can be modelled analytically in spherical symmetry (see Appendix B). However, even those flows which do not reach equilibrium will adjust to changes in the structure of the nucleus, such as an increase in the central luminosity, within a flow crossing timescale.

2.2 Components of Active Nuclei

This paper concentrates on the structure of the hot global ISM which fills much of the volume of an active nucleus. In this section, we describe the other basic physical components of the nucleus which dominate its mass content and energetics, and which give rise to and act on the global flow to determine its structure.

2.2.1 The Black Hole and Stellar Cluster

We assume that an AGN contains a supermassive black hole, of mass $M_h = 10^8 M_{h,8} M_\odot$, surrounded by a starburst stellar cluster, of total mass $M_{cl} = 10^8 M_{cl,8} M_\odot$. For the fiducial model of a luminous QSO, the cluster has a mass of $M_{cl,8} \simeq 10$. Dynamical models (MCD) show that the stellar cluster dominates the gravitational potential of the nucleus, and that the black hole typically represents only 20–50 per cent of the mass of the system. Observational support for this is discussed in appendices A1 and A2. Mass is liberated from the stars within the cluster and distributed through the volume of the nucleus.

The stellar cluster is chosen to be steady and spherically symmetric with a stellar density given by

$$\rho_* = \rho_{*,c} \bar{\rho}_*(r/r_c), \quad (1)$$

where $\bar{\rho}_*$ is the dimensionless spatial profile function normalised at the core radius, r_c . In this paper, we take a broken power-law form for $\bar{\rho}_*$ (cf Appendix A2):

$$\bar{\rho}_* = \begin{cases} (r/r_c)^{-s} & r < r_c \\ (r/r_c)^{-h} & r > r_c, \end{cases} \quad (2)$$

The power-law indices, s and h , are required to be $s < 3$ and $h > 3$ for the cluster mass to be finite. In fact, we choose $s = 0$ and $h = 5$ in most of the models presented, similar to the Plummer model initial conditions of MCD. Experiments with different stellar distributions did not greatly alter the results that we discuss. Where we take $h = 5$, the core radius is often chosen to be 2/3 pc, in order that the average radius of mass injection is 1 pc. With these parameters, the central stellar density within r_c for our canonical model is $\rho_{*,c} = 3.2 \times 10^8 M_\odot \text{ pc}^{-3}$. This value is considerably larger than that inferred from observations of nearby galactic nuclei (Watson 1999), but the lifetimes of the clusters we consider are short and their presence may be masked by the luminosity of the QSO they feed (for a more detailed discussion, see Appendix A2). If the gravity and radiation

forces are negligible in such a model, the outflow becomes transonic at 0.89 pc.

2.2.2 Stellar Mass Loss

There are various sources of mass for the flow in the nISM. Stars in the stellar cluster lose mass through the normal processes of stellar evolution, and also as a result of collisions within the stellar cluster and tidal disruption as they pass close to the black hole. The mass-loading rate, \dot{q} , is chosen to be spherically symmetric, and time steady over the period of our calculations. Clearly the mass-loss rate evolves over the lifetime of the cluster and is a function of the age and IMF of the cluster. However, the timescales of this evolution are much longer than the typical dynamical timescales over which our calculations run. We write

$$\dot{q}(r) = \dot{q}_c \tilde{q}(r/r_c). \quad (3)$$

In the present paper, we restrict ourselves to the case that the mass-loading rate to be proportional to the stellar density, at a rate

$$\dot{q}(r) = Q \rho_*(r), \quad (4)$$

so that $\dot{q}_c = Q \rho_{*,c}$, $Q \simeq 10^{-8} \text{ yr}^{-1} Q_{-8}$, and $Q_{-8} \sim 1$ for a young cluster of massive stars (cf. Appendix A2; Williams & Perry 1994; Murphy & Perry 1999).

2.2.3 Accretion Disc

Accretion from the global flow, directly and through the accretion disc, powers emission from the vicinity of the central black hole (Zycki, Collin-Souffrin & Czerny 1995). The galaxy ISM may also feed an accretion disc if it does not hang up at an intermediate radius, and if the extended (~ 1 pc scale) regions of the disc are stable (Hure et al. 1995).

The accretion disc which forms around the black hole can also act as both a source and a sink of gas. In the hot central regions, a wind may be driven from the disc surface. Further out, gas may condense onto its surface, while self-gravitating instabilities could generate clumps of cool gas which would then be ablated by the nISM flow as it streams past. Eventually, the mass lost from the stellar cluster must either reach the black hole, to power the luminosity of the AGN, or be blown out of the nucleus in a wind.

2.2.4 Luminosity

The total integrated luminosity is

$$L_{\text{Bol}} \equiv 10^{46} L_{46} \text{ erg s}^{-1}. \quad (5)$$

We model the angular distribution of the radiation field, $L_{\text{Bol}}(\theta)$, by two components, one isotropic – representing the radiation directly associated with the black hole – and the other anisotropic, representing the radiation of a thin accretion disc. This accretion disc luminosity is the only component of our model which is not spherically symmetric (Appendix A5). As we discuss in Appendix A6, we assume for the moment that any variation in the continuum spectrum with angle is unimportant. As we assume that the dominant opacity is electron scattering, we can describe the

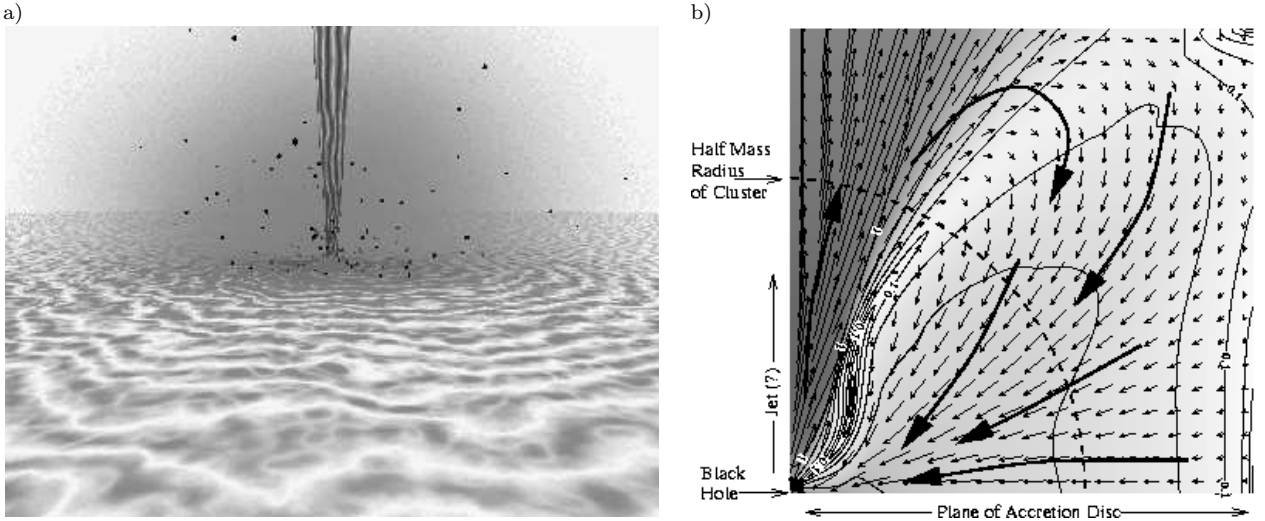


Figure 1. Illustrations of the assumed structure of the nucleus. In a), a schematic view of the nucleus shows the extensive disc which surrounds the black hole. Along the axis of the disc, a radio jet is driven outwards in about 10 per cent of active nuclei. Around the black hole, the stellar density is high enough to be treated as a distinct stellar cluster – a small fraction of these stars are indicated by dots in this figure. The nebulosity which fills the region within the cluster illustrates the location of the nISM which we simulate. In b), we illustrate how these components relate to the structure of the simulations shown in the rest of this paper. The black hole is at the origin of the grid, the accretion disc in the horizontal plane, and any jet would travel along the vertical axis. The half-mass radius of the cluster reaches out a substantial way through the grid: mass loss from the cluster falls inwards in the plane of the accretion disc, and is driven outwards along its axis.

luminosities by Eddington ratios (i.e., ratios of outward radiative force to the inward gravity of the black hole) for a given black hole mass, where the radiation flux at (r, θ) is

$$F(r, \theta) = f_{\text{Edd}}(\theta) \frac{L_{\text{Edd}}}{4\pi r^2}, \quad (6)$$

and where the Eddington limit luminosity (at which the radiation driving balances the gravitational acceleration) is given by

$$L_{\text{Edd}} \simeq 1.3 \times 10^{46} M_{\text{h,8}} \text{ erg s}^{-1}. \quad (7)$$

The angularly dependent Eddington ratio, $f_{\text{Edd}}(\theta)$, is specified by its average over solid angle

$$\langle f_{\text{Edd}} \rangle = \frac{1}{4\pi} \int f_{\text{Edd}}(\theta) d\Omega, \quad (8)$$

and an angular form function $\bar{f}(\theta)$ which depends on the fraction of the luminosity in the anisotropic component, f_{disc} and its angular dependence (Appendix A5), so $f_{\text{Edd}}(\theta) = \langle f_{\text{Edd}} \rangle \bar{f}(\theta)$. Studies of AGN have indicated that typical values of f_{Edd} vary from 10^{-3} to values close to unity (Laor 1990; Collin-Souffrin 1993), with the higher ratios found for the brighter nuclei. However, even amongst Seyfert galaxies with very similar source luminosities the Eddington ratio appears to vary between $10^{-4.5}$ (NGC 4258, Lasota et al. 1996) and 0.5 (NGC 1068, Greenhill et al. 1996).

2.2.5 Thermal Equilibrium

Consistent with our choice of electron scattering as the dominant opacity source, we assume that the gas is maintained everywhere in isothermal equilibrium, at the mean Compton temperature of the central luminosity source, $T_C = T_7 \times 10^7 \text{ K}$. This temperature is determined by the spectrum

of the radiation, with values $0.6 \lesssim T_7 \lesssim 15$ predicted for in the majority of AGN (Krolik, McKee & Tarter 1981; Fabian et al. 1986; Mathews & Ferland 1987). We discuss the physical limits on the validity of this assumption in Appendix A6. The sound speed in fully ionized gas with solar abundance is $c_s = 360 T_7^{1/2} \text{ km s}^{-1}$: we have used $c_s = 10^{-3} T_7^{1/2} c$ for simplicity.

The assumption of isothermality allows us to scale our models to a wide range of situations; however, there are some limits on the applicability of this assumption. The presence of strong shocks in our simulations means that including the energy equation explicitly would allow gas to cool: the production of such cool gas is important in deriving observational diagnostics for the flow, in calculating the rate at which gas can be added to the accretion disc (though limits can be put on the amount of gas which can possibly be added to the disc in this manner), and in increasing the radiative force per unit mass, which may have important dynamical effects. However, in the context of global models, the short time- and length-scales which will characterise this cool gas mean that it is difficult to accurately model both small and large-scale flows. Modelling the details of mass-injection from individual stellar sources presents similar difficulties. In consequence, we have decided to focus first on the global properties of flows which remain closely isothermal, and treat the finer-scale structures in future papers.

2.2.6 Forces

As well as hydrodynamic effects, body forces act on the nISM as a result of gravity, radiation pressure, and friction with the mass injected into the flow. The gravity is dominated by the black hole and the stellar cluster (Appen-

dix A4). We assume that the mass loss from the cluster is, on average, at rest with respect to the black hole and stellar cluster and must therefore be accelerated by the flow.

The radiative driving acceleration due to Thomson opacity is given by

$$g_{\text{rad}} = \frac{\sigma_T F(r, \theta)}{m_H c} = f_{\text{Edd}}(\theta) \frac{GM_h}{r^2}, \quad (9)$$

where σ_T is the electron scattering cross section. The gravitational force on the nISM at r is due to both the mass of the black hole and the mass of the stellar cluster which lies within r ; the latter can be written as

$$M_{\text{cl}}(< r) = M_{\text{cl}}\mu_*(r/r_c), \quad (10)$$

where $\mu_*(r/r_c)$ is the fraction of the total cluster mass within r . The form of μ_* for our broken power-law is given in Section A4.

The inverse-square laws for the central radiative and gravitational forces hold at all radii outside, respectively, $\sim 10^{-3}$ pc (where the finite spatial extent of the radiating accretion disc becomes important) and $\sim 10^{-4}$ pc (where relativistic corrections need to be made), in QSOs. In addition to these limits to the inverse-square law, the effects of the angular momentum of the hot phase, pressure from a thick central disc, and extra heating processes (such as stimulated Compton scattering) may effectively work counter to the gravitational force. We have chosen to mimic these effects by smoothing the forces in a region close to the central black hole. Instead of a pure inverse-square law, we take the forces to vary as

$$g \propto \frac{r}{(r^2 + \epsilon^2)^{3/2}}, \quad (11)$$

where in general we take the smoothing radius, ϵ , to be far smaller than the cluster radius, but significantly larger than the grid resolution where possible. In this way, the grid resolves the flow structures throughout the nucleus.

We shall see that the link between the gravitational velocities at the radius at which the outflow is driven and the broad line kinematics leads to one of the fundamental distinctions between the results of the current paper and previous models of global flows in active nuclei. The low-ionization lines may be formed in exactly the regions of the accretion disc which dominate the anisotropic continuum emission (CDMP), which is one physical origin for such a smoothing term. This provides a link between LILs and the driving of the global wind in which the high-ionization lines are formed since these HIL are formed behind shocks within the global flow. The shock velocities, reflected in the line widths, represent the superposition of the nISM velocities upon the stellar kinematics (Perry 1999). Both the low- and high-ionization emitting regions have velocities determined by the gravitational potential. The high-ionization emitting gas has an additional component of velocity due to the nISM flow. Hence the similarity of high- and low-ionization line-widths (Corbin 1991) arises naturally in these models, allowing for the centroid shift between the lines (Espey et al. 1989; Tytler & Fan 1992; Sulentic et al. 1995).

2.3 Interfaces: Accretion discs, jets, the galaxy

We now discuss the interfaces of the nuclear flow at the edges of our computational grid. In the plane $z = 0$, the flow interacts with the accretion disc. Along the grid axis, $r = 0$, there may be a relativistic jet. At large radii, the flow in the nucleus will interact with the galaxy ISM.

2.3.1 Disc interface

The nuclear starburst stellar cluster inevitably creates an nISM. No available treatment of accretion disc physics has considered the myriad physical processes which may arise in such an environment. The nISM flow near the disc plane can clearly have a wide range of detailed structures. At one extreme, the nISM and accretion flows are completely separated by a contact discontinuity, and may be modelled by a mirror boundary condition. At the other extreme, if the pressure is sufficient that cooling can occur, all the material raining onto the disc will be lost to the global flow and incorporated into the disc. We model the latter case by specifying a region of the accretion disc over which we treat the disc plane as a mass sink.

The scale height, H , of a thin accretion disc is given by

$$\frac{H}{r} \simeq 0.015 \left(\frac{T_4 r_{\text{pc}}}{M_{h,8}} \right)^{1/2}, \quad (12)$$

where $T_4 \simeq 1$ is suggested by many models of the inner disc. This will be reduced still further by the gravity of the stellar cluster at radii beyond the cluster core. We can, at best, marginally resolve the cool disc in a (uniformly gridded) global model of the flow in AGN. The thermal equilibrium time of the disc gas is of order the recombination timescale, roughly 3×10^4 s, even at a density as low as 10^8 cm^{-3} . To accurately model the structure of the disc would require a cell size $\sim 10^{-8}$ times the size of the global grid.

2.3.2 Jet interface

The other inner boundary condition on the models is along the axis of the disc. This will form the interface with a nuclear jet, if one is present. While radio-loud AGN, with their strong jets, form only 10 per cent of the population, there is evidence for radio emission on BELR scales in many more nuclei (Dunlop et al. 1993; Kukula et al. 1997b).

In the present paper, we treat the axis as a mirror boundary, in effect assuming there is no jet or that its width is $\ll 1$ pc. In reality, a boundary layer will form at the interface between global flow and jet. We leave the detailed treatment of such boundary layers for the present. In some cases we do find that well-collimated non-relativistic jets form spontaneously in our model, driven by the wide opening angle outflow from the central black hole.

2.3.3 Galaxy interface

In real active nuclei, mass, momentum and angular momentum will be exchanged between the active nuclear region and the wider galaxy. The rate of this exchange will depend upon both the properties of the nuclear region and of the galaxy. The timescales for stellar evolution and mass inflow

from galaxy interactions are comparable, but far longer than those over which the structure of the nuclear ISM is determined.

The rate of mass input by the galaxy to the nucleus has been the subject of much discussion. Shlosman et al. (1990, see also, e.g., the proceedings edited by Shlosman 1994) suggest that the rate may well be controlled by galactic interactions and subsequent instabilities. While some inflow of the hot phase from the ISM of a normal galaxy may occur, it is difficult for this gas to lose its angular momentum and so the accretion rates will be a very small component of the mass budget of the nucleus (and may be further suppressed by any nuclear wind). Where a galaxy interaction has occurred, however, the angular momentum constraint is removed for gas distributed on kiloparsec scales. The similarity between interaction timescales and the stellar formation and evolution timescales within the nucleus might then suggest that most active nuclei would be observed during the actively star forming phase. However, when the details of the fuelling process are considered, it is found that the infalling gas tends to remain well outside the nucleus until a sufficient mass has collected that it gas go through a self-gravitating instability and can then fall inwards once more (the so-called ‘bars within bars’ picture). The fuelling thus depends on this threshold process operating on scales of ~ 100 pc, where dynamical timescales are far shorter than those of galactic interactions. It is thus reasonable to concentrate upon the case in which mass input from the wider galaxy is negligible in this first paper.

Making only the reasonable assumption that the galaxy succeeds in creating a nuclear stellar cluster (cf. Watson 1997, and references therein) we conclude that *in situ* feeding of the black hole by the stellar cluster is highly probable.

3 THE THEORETICAL MODEL: TOWARDS AN HR DIAGRAM FOR AGN

We next discuss the basic equations, moving on to the scaling of the solutions to different sets of parameters (Section 3.2), the scalings which may characterise observed AGN (Section 3.3), and the parameters which dominate the flow structures (Section 3.4, which also introduces our diagnostic plot).

The interstellar medium is evolved using the equations of hydrodynamics, with a distributed mass-loading source function and gravitational and radiative forces. These are conservation of mass:

$$\frac{\partial \rho}{\partial t} + \nabla \cdot (\rho \mathbf{v}) = \dot{q}, \quad (13)$$

the equations of motion,

$$\rho \frac{D\mathbf{v}}{Dt} = -\nabla p - \dot{q}\mathbf{v} - \rho \mathbf{g}, \quad (14)$$

and the energy equation,

$$\begin{aligned} \frac{\partial}{\partial t} \left(\frac{1}{2} \rho v^2 + \frac{p}{\gamma - 1} \right) &= -\nabla \cdot \left[\mathbf{v} \left(\frac{1}{2} \rho v^2 + \frac{\gamma p}{\gamma - 1} \right) \right] \quad (15) \\ &\quad - \rho \mathbf{g} \cdot \mathbf{v} + \rho(\Gamma - n\Lambda) + \frac{\dot{q} c_s^2}{\gamma - 1}, \end{aligned}$$

together with the equation of state $p = \rho k_B T / \mu$, where μ is

the mean mass per particle, $\gamma = 5/3$ is the adiabatic constant, Γ and Λ are the usual heating and cooling coefficients, and c_s is the isothermal sound speed which characterises the internal energy of the mass injected.

These equations include both the effects of applied gravitational and radiative forces through the combined effective acceleration term,

$$\mathbf{g} = \frac{G[(1 - f_{\text{Edd}}(\theta))M_h + M_{\text{cl}}(< r)]}{(r^2 + \epsilon^2)^{3/2}} \mathbf{r}, \quad (16)$$

where $M_{\text{cl}}(< r)$ is given by equation (A6). Mass loading from the stellar cluster, at a rate \dot{q} per unit volume per unit time, is included both in the mass conservation equation and as a frictional term in the equations of motion. The only radiative driving which we have included is that due to Thomson scattering.

3.1 Isothermal Flows

In the present paper we assume that the nISM is maintained in radiative equilibrium at the Compton temperature and hence do not solve the energy equation; instead we use the isothermal equation of state $p = \rho c_s^2$ where the isothermal sound speed c_s is determined by Compton equilibrium (we discuss the validity of this assumption in Appendix A6). The input parameters to the equations governing the system are therefore the mass of the black hole M_h ; the mass of the stellar cluster M_{cl} , the radial distribution of the mean stellar density $\bar{\rho}_*(r/r_c)$, the cluster core radius r_c ; the mass loading rate density in the core \dot{q}_c , and its radial variation $\tilde{\dot{q}}(r/r_c)$; the bolometric luminosity L_{Bol} , the sound speed in the nISM c_s and the distribution of the effective Eddington ratio $f_{\text{Edd}}(\theta)$.

Spherically symmetric, electron scattering driven, point source isothermal flows ($f_{\text{Edd}}(\theta) = \text{const}$ [less than unity], $\rho_* = \dot{q} = 0$) have the well-known Parker solutions, with a characteristic length given by the sonic point radius, r_s , ($r_s = (1 - f_{\text{Edd}})M_h/c_s^2$, Kippenhahn et al. 1975, hereafter KMP) and a characteristic velocity by the sound speed, c_s . In such flows, the radiation driving reduces the effective mass of the central gravitating object, M_h , to $(1 - f_{\text{Edd}})M_h$. As is well known, the solution (wind or accretion flow) which is realised in any particular physical situation is determined by the boundary conditions.

This universal solution topology is removed by the radial variation of the gravitational force or the distributed mass loading (both of which may introduce internal shocks and additional sonic point to the flow; mass loading also may introduce stagnation points), or, most dramatically, by the symmetry breaking introduced by the angular dependence of the radiation. Each set of $f_{\text{Edd}}(\theta)$, $\rho_*(r/r_c)$ and $\dot{q}(r/r_c)$ gives rise to a different family of solutions, further differentiated by the values of four dimensionless ratios between the other physical input parameters, as discussed below. Although this may, at first sight, appear to render any general conclusions impossible, the physical expectation that most AGN share similar spatial forms for f_{Edd} , ρ_* and \dot{q} even when they differ in their total M_h , M_{cl} and L_{Bol} means that we can classify families of solution which apply over a broad range of objects, as we now discuss. In order to do so we write the equations in scaled, dimensionless form.

3.2 Dimensionless Equations

We can cast equations (13), (14) and (16) into dimensionless form by scaling all distances to the cluster core radius, r_c (i.e. $\mathbf{r} = r_c \tilde{\mathbf{r}}$, $\nabla \rightarrow (1/r_c) \tilde{\nabla}$ and $\epsilon = r_c \tilde{\epsilon}$) and all velocities to the isothermal sound speed, c_s , (i.e. $\mathbf{v}(\mathbf{r}, \theta, t) = c_s \tilde{\mathbf{v}}(\tilde{\mathbf{r}}, \theta, \tilde{t})$), from which it follows that all times scale as $t = r_c/c_s \tilde{t}$. Furthermore $\rho(\mathbf{r}, \theta, t) = (\dot{q}_c r_c/c_s) \tilde{\rho}(\tilde{\mathbf{r}}, \theta, \tilde{t})$. We then have

$$\frac{\partial \tilde{\rho}}{\partial \tilde{t}} + \tilde{\nabla} \cdot (\tilde{\rho} \tilde{\mathbf{v}}) = \tilde{q}, \quad (17)$$

and

$$\tilde{\rho} \frac{D \tilde{\mathbf{v}}}{D \tilde{t}} = -\tilde{\nabla} \tilde{\rho} - \tilde{q} \tilde{\mathbf{v}} - \tilde{\rho} \tilde{\mathbf{g}}, \quad (18)$$

where

$$\tilde{\mathbf{g}} = \frac{GM_{\text{cl}}}{r_c c_s^2} \frac{[(1 - \langle f_{\text{Edd}} \rangle \tilde{f}(\theta)) (M_h/M_{\text{cl}}) + \mu_{\star}(\tilde{r})]}{(\tilde{r}^2 + \tilde{\epsilon}^2)^{3/2}} \tilde{\mathbf{r}}, \quad (19)$$

Hence, from equations (17), (18) and (19) we see that the dimensionless solution $(\tilde{\mathbf{v}}, \tilde{\rho})$ depends on

(1) $\tilde{f}(\theta)$, $\bar{\rho}_{\star}(\tilde{r})$ and $\tilde{q}(\tilde{r})$ – three dimensionless spatial form functions: these specify the angular variation of the radiation, the spatial variation of the stellar density and the mass loading, respectively,

and the six physical parameters, M_h , M_{cl} , r_c , L_{Bol} , c_s (or equivalently T_{nISM}), and ϵ , through the four dimensionless ratios:

- (II) $GM_{\text{cl}}/r_c c_s^2$ – essentially the ratio of the stellar cluster velocity dispersion to the sound speed,
- (III) the ratio of the black hole to total cluster mass, M_h/M_{cl} ,
- (IV) the Eddington ratio, $\langle f_{\text{Edd}} \rangle$, and
- (V) the dimensionless smoothing length, $\tilde{\epsilon} = \epsilon/r_c$.

Note that no value dependent on \dot{q}_c appears in the list, since the isothermal equations are homogeneous in ρ and \dot{q} . Whereas \dot{q}_c sets the physical scale of ρ , it can be ignored for isothermal flows as far as the dynamics is concerned. This is a result of our assumption that $f_{\text{Edd}}(\theta)$ [or, equivalently, $L_{\text{Bol}}(\theta)$] is a free parameter. If we had included the structure and dynamics of the accretion disc in the hydrodynamics then the rate of mass-loss, $\propto \dot{q}$, would determine $L_{\text{Bol}}(\theta)$ and $f_{\text{Edd}}(\theta)$ directly.

By varying (I) through (V), each of the numerical solutions we present can be rescaled to a wide variety of AGN. In fact, as we shall discuss, two particular dimensionless ratios dominate the differences between solutions. The similarity of form of the solutions for a wide variety of AGN allows us to predict how, for example, the dynamics will scale with e.g. changing luminosity or Eddington ratio and spectral shape (or temperature) or luminosity and cluster core radius.

For the solutions to scale, there are also constraints on the boundary conditions: for most of our simulations, these are observed as, for instance, free-flow boundary conditions which have no dimensional dependence; where accretion is allowed over some fraction of the disc, however, the size of this region must be specified as a fraction of the cluster core radius for the models to scale. In reality, several of these dimensionless parameters will be less important than terms that break the scaling, such as heating and cooling of the nISM gas.

As we shall see, within broadly similar bipolar nISM structures common to all symbiotic AGN, there are systematic differences in topology (see Fig. 2). AGN of widely different bolometric luminosities can have topologically identical flows if they all share a common stellar density profile (i.e. core halo structure $\bar{\rho}(\tilde{r})$), have stellar mass loss rates which are directly proportional to ρ_{\star} , have the same radiation pattern $\tilde{f}(\theta)$, ratios (II) through (V), and scaled boundary conditions. I.e. if their underlying physical structure is similar, their nISM will be described by a single dimensionless solution $(\tilde{\mathbf{v}}, \tilde{\rho})$ to equations (17), (18) and (19). However, rather than present dimensionless solutions for particular combinations of (I) through (V), we have chosen to present all our results in physical units for fiducial models in order to make them more immediately accessible. Below, we describe the manner in which the models which we have calculated can be scaled to a wide range of parameter values, and discuss how these scalings may relate to the relationships which have been inferred observationally for AGN.

We have grouped $\bar{\rho}_{\star}(\tilde{r})$ and $\tilde{q}(\tilde{r})$ in (I) above, since in this paper we make the further restriction that these spatial distribution functions are equal, which is equivalent to the assumption that $\dot{q}_c = Q \rho_{\star,c}$. [For this limit to be strictly valid, we must consider young stellar clusters with core densities $\rho_{\star,c} \lesssim 10^9 M_{\odot} \text{ pc}^{-3}$, above which collisions and tidal disruption at small radii make a significant contribution to the mass loss (MCD). Models A, B, C are all below this limit, but may breach it when scaled to Seyfert parameters.] In this case equation (17) becomes

$$\frac{\partial \tilde{\rho}}{\partial \tilde{t}} + \tilde{\nabla} \cdot (\tilde{\rho} \tilde{\mathbf{v}}) = \bar{\rho}_{\star}. \quad (20)$$

The densities and pressures in the nISM flow are then $\rho = (Q \rho_{\star,c} r_c/c_s) \tilde{\rho}$ and $p = (Q \rho_{\star,c} r_c c_s) \tilde{\rho}$.

Clearly in such isothermal flows, a consequence of the scaling is that changes in the source spectrum, which result in a change in the Compton temperature and thus in c_s , imply a consequent change in the time scales. Other things being equal, the same \tilde{t} corresponds to a shorter real time in hotter flows (with harder spectra). Note, again, that no value dependent on Q appears in the list.

Taken together, if ratios (II), (III), and (IV) are constant, then each of L_{Bol} , M_h and M_{cl} is proportional to $r_c c_s^2$ with a known factor, so $L_{\text{Bol}} \propto M_h \propto M_{\text{cl}}$.

3.3 From High Luminosities to Low: How AGN Scale in Nature

One of the most striking features observed in the spectra of AGN is the remarkable consistency of their dynamics over orders of magnitude in total bolometric luminosity. Line widths – direct measures of gas velocities – vary almost imperceptibly as L_{Bol} changes from $\leq 10^{43}$ to $\geq 10^{47} \text{ erg s}^{-1}$. The size of the emitting region, however, appears to track the luminosity, $r_{\text{BLR}} \propto L_{\text{Bol}}^{1/2}$ (from reverberation and photoionization studies). Controversy still surrounds the question of whether or not black hole masses and/or the efficiency of the radiation process ($\langle f_{\text{Edd}} \rangle$) vary as L_{Bol} varies – or, more accurately put, whether L_{Bol} varies because of variations in M_h , f_{Edd} , or because of the availability of fuel. The fuel supply is controlled by stellar and galactic processes. Unfortunately, to date observations can measure nei-

ther the properties (M_{cl} , $\rho(r)$, age or IMF) of the stellar cluster (because it is outshone by the central radiation by orders of magnitude Williams & Perry 1994), nor the rate of any possible inflow of matter from the galaxy. The relationship between the properties of the cluster and the fuelling process is, at least in part, a theoretical prediction of this paper.

We now consider the implications for AGN of the scale invariance of the equations and discuss how the physical properties of AGN are expected to vary as a function of luminosity, L_{Bol} . Our models make clear predictions about how unobserved properties (e.g. M_{cl} and r_c) are expected to behave as a consequence of those which are observed. They also provide simple rules for scaling the solutions we present here to objects with other luminosities or cluster/BH properties so that the reader can choose amongst the solutions we present those which are appropriate to her or his favourite AGN.

Consider a family of *structurally similar* AGN (i.e. the same (i)) all of which share the same characteristic values of (ii), (iii) and (v), but which differ in L_{Bol} , and possibly in $\langle f_{\text{Edd}} \rangle$ (iv). The members of the family will have different characteristic sizes, velocities, time scales and masses. If their spectral hardness differs, so will their Compton temperatures, and thus their sound speeds. We denote the ratio of their sound speeds by ν , the ratio of their typical length scales by λ , and the ratio of their timescales by τ . For consistency, $\tau \propto \lambda/\nu$. Further, we denote the ratio of their mass loss rates by ϕ (which, for given λ and τ or ν , sets the gas density scale). The constancy of (ii) means that cluster masses scale as $M_{\text{cl}} \propto \lambda\nu^2$, the stellar mass densities as $\rho_{*,c} \propto (\nu/\lambda)^2$ and the nISM gas densities as $\rho \propto \phi\nu/\lambda \propto \phi/\tau$. The ionization parameter in the flow, $\Xi = L_i/(4\pi r^2 n_{\text{H}} k T c)$ (see Section 7.3), scales as $\Xi \propto L/\phi\lambda\nu^3$.

3.3.1 AGN with constant Eddington ratios

We first consider a class of AGN of different total luminosities which are all able to accrete with equal efficiencies and, in consequence, to radiate with the same constant Eddington ratio. In such a population, with (i) through (v) constant, the masses of the black hole and stellar cluster scale as the luminosity ($M_{\text{cl}} \propto M_{\text{h}} \propto L/\langle f_{\text{Edd}} \rangle \propto L$) and $\lambda\nu^2 \propto \lambda^3/\tau^2 \propto L$; the ionization parameter then scales as $\Xi \propto 1/\phi\nu$.

(a) If, in such an AGN population, the velocities were constant (roughly as observed), the characteristic sizes of the regions would scale as $\lambda \propto L$ (rather than $\lambda^2 \propto L$ as is often discussed), and typical timescales would scale as $\tau \propto \lambda \propto L$. The stellar clusters would be very much denser and smaller as the luminosity decreased: $\lambda \propto L$, $\rho_{*,c} \propto 1/L^2$. Furthermore, the ionization parameter would be a function only of the mass loss rate of the cluster stellar populations through ϕ : $\Xi \propto 1/\phi$.

(b) Alternatively, if L/r^2 were constant within a population, as is often inferred from broad line studies, (e.g. Netzer & Peterson 1997), then $\lambda^2 \propto L \propto M_{\text{h}}$. In that case, our models predict that the velocities would scale as $\nu \propto (L/\lambda)^{1/2} \propto L^{1/4}$, implying also that the spectra of AGN must harden slightly ($\langle h\nu \rangle \propto T \propto L^{1/8}$) as they become brighter. The stellar clusters would be more compact and denser as the

luminosity decreased, but the changes would be significantly weaker than in (a), $\lambda \propto L^{1/2}$, $\rho_{*,c} \propto 1/L^{1/2}$, which seems more probable. Furthermore, the typical timescales and the ionization parameter would be weakly dependent on L , $\tau \propto L^{1/4}$ and $\Xi \propto 1/\phi L^{1/4}$.

There is some observational evidence for this kind of relation between line width and luminosity. Baldwin, Wampler & Gaskell (1989) find a correlation between the width of C III] 1909 and source luminosity, but not for the other lines they studied. The variation in Compton temperature also compares well with observed change in continuum shape with source luminosity (e.g. Zheng & Malkan 1993). Mushotzky & Ferland (1984) find an anticorrelation between ionization parameter and luminosity of this form can also explain the Baldwin effect, an anticorrelation between the equivalent width of lines and the source luminosity. All such observations are, however, plagued by selection effects and the wide dispersion between the emission line properties of individual galaxies with a certain luminosity.

3.3.2 Eddington ratio varying with L_{Bol}

It is possible that the Eddington ratio varies systematically with source luminosity (a point to which we return below). This would seem to exclude scaling the solution to equations (18) and (20) found for one AGN to other AGNs with different $\langle f_{\text{Edd}} \rangle$ since, as we have just seen, $\langle f_{\text{Edd}} \rangle$ is one of the dimensionless ratios defining the topology of the solution which we wish to apply to AGN of varying L_{Bol} . However, as we shall see from our simulations, the most important value of the Eddington ratio for the flow is that on the axis of the accretion disc, $f_{\text{Edd},0}$. Thus, for the moment, assume that we can ignore the angular variation of the luminosity. In that case, we can relax the condition that $\bar{f}(\theta)$ must be invariant (this assumption is supported by our numerical simulations, see Section 6), which is equivalent to allowing the degree of beaming to vary with L or f_{Edd} . Since theoretical studies of the structure of accretion discs find structural changes with f_{Edd} , this seems a reasonable assumption. When $\bar{f}(\theta)$ is constant $\langle f_{\text{Edd}} \rangle \propto f_{\text{Edd},0}$, whereas when $\bar{f}(\theta)$ varies with L , $\langle f_{\text{Edd}} \rangle$ and $f_{\text{Edd},0}$ are independent.

Given the primacy of $f_{\text{Edd},0}$, we find that the forces which act upon the flow are controlled by an effective black hole mass, $(1 - f_{\text{Edd},0})M_{\text{h}}$, rather than directly by $\bar{f}(\theta)$ and the BH mass separately. Parameters (iii) and (iv) then combine into a single parameter, $(1 - f_{\text{Edd},0})(M_{\text{h}}/M_{\text{cl}})$ which defines the solution and must be scaled for different AGN. Note that in the trivial case that the radiation is isotropic and $f_{\text{Edd}}(\theta) = 1$, the BH has no net effect on the flow and its mass is arbitrary.

Consider now such a class of AGN whose Eddington ratios, $\langle f_{\text{Edd}} \rangle$, vary systematically with luminosity. Requiring $(f_{\text{Edd},0} - 1)M_{\text{h}}/M_{\text{cl}}$ to be constant rather than (iii) and (iv) introduces an additional degree of freedom, and relaxes the strict scaling between the masses and the luminosity. The constancy of (ii) means that, as before, $M_{\text{cl}} \propto \lambda\nu^2$. Since $M_{\text{h}} \propto L/\langle f_{\text{Edd}} \rangle$, the new condition, $(f_{\text{Edd},0} - 1)M_{\text{h}}/M_{\text{cl}} = \text{const.}$, becomes $(f_{\text{Edd},0} - 1)/\langle f_{\text{Edd}} \rangle \propto \lambda\nu^2/L$.

(c) Consider first a population for which the velocities vary as weakly as $\nu \propto L^{1/4}$, for which $(f_{\text{Edd},0} - 1)/\langle f_{\text{Edd}} \rangle \propto \lambda/L^{1/2}$. If, in addition, $L \propto \lambda^2$, $(f_{\text{Edd},0} - 1)/\langle f_{\text{Edd}} \rangle = \text{const.}$ as we found in (b) above, $v \propto L^{1/4}$ combined with $L \propto r^2$

implies that f_{Edd} is constant; all other properties then vary as they did in (b).

(d) If the velocities have constant characteristic values (ν = constant), then the masses of the clusters must scale as $M_{\text{cl}} \propto \lambda$ whereas the masses of the black holes scale as $M_{\text{h}} \propto L/\langle f_{\text{Edd}} \rangle \propto \lambda/(f_{\text{Edd},0} - 1)$. If, in addition, $L \propto \lambda^2$, we find that the Eddington ratios must scale as $(f_{\text{Edd},0} - 1)/\langle f_{\text{Edd}} \rangle \propto L^{-1/2}$. Typical timescales, $\tau \propto \lambda \propto L^{1/2}$, in accord with the observation that typical timescales are shorter in low luminosity objects. We find also that $\Xi \propto L^{1/2}/\phi$, i.e. for clusters with the same IMF and age, ($\phi \approx \text{const}$), $\Xi \propto L^{1/2}$.

If the relation $(f_{\text{Edd},0} - 1)/\langle f_{\text{Edd}} \rangle \propto L^{-1/2}$ found in (d) is imposed, and we attempt to impose $\bar{f}(\theta)$ constant, we find that both $f_{\text{Edd},0}$ and $\langle f_{\text{Edd}} \rangle$ increase as L decreases. This correlation is in the opposite direction from that inferred from observation, but will occur only for a narrow range of luminosity before the luminosity becomes super Eddington at all angles. The flow structures change dramatically when this occurs, suggesting that they will not scale between Seyfert galaxies and QSOs. Alternatively, the flows *can* scale when the Eddington ratio varies with L and the characteristic velocities are constant, but only if the continuum becomes closely beamed as the luminosity decreases. If the on-axis Eddington ratio is roughly constant, we find that $\langle f_{\text{Edd}} \rangle \propto L^{1/2}$ which accords well with some estimates of the variation of the variation of f_{Edd} with L . Furthermore, this then means that $M_{\text{h}} \propto M_{\text{cl}} \propto L^{1/2}$; the stellar cluster will be more compact and denser as L decreases, $\lambda \propto L^{1/2}$, $\rho_{\star,c} \propto 1/L$. This situation seems in broad accord with observations. We conclude that in the case of constant $f_{\text{Edd},0}$ but varying $\langle f_{\text{Edd}} \rangle$ we can scale our solutions for QSOs to low- L AGN.

The variation of some physical timescales with these scaling parameters is included in Table 2. If dynamical velocities are constant, most of the timescales will vary in proportion to the length scale; QSO models can then be scaled to other situations. Notable exceptions are the stellar collision time, and the frequency and lifetime of supernovae. In smaller nuclei, stellar collisions will become an important mass source while supernovae will become infrequent events: when they do occur, both processes will have a catastrophic effect on the nuclear ISM.

3.4 An HR Diagram for AGN?

As we have discussed, our models are determined by four dimensionless ratios and a number of ‘form factors’. However, extensive numerical modelling has suggested that the number of parameters which dominate the overall form of the flow is far smaller than is yielded by such a formal reduction. We find that the solutions we calculate can be well described by just two dimensionless ratios, describing how strongly the gas is bound to the nucleus as a whole and how strongly it is driven away by the black hole at its centre. In the rest of this paper, we present models to illustrate the reasonableness of this simplified parameterisation, and its usefulness as a classification scheme for the numerical models. The details of this classification scheme are presented in Sections 3.4.2 and 7.1. While the derivation of detailed observational diagnostics is beyond the scope of the present paper, we intend to work to bridge the gap between em-

Table 3. Derived velocities, for the models defined in Table 5. The values of v_K , v_z and c_s are set by the parameters of the model. The ejection velocity, v_{ej} , is the peak outflow speed in a region close to $z = 0.2$ pc on axis (except \dagger E close to $z = 0.04$ pc, F close to $z = 2$ pc), where the mass ejected from the region close to the black hole has reached close to its final value.

Label	v_K/c_s	v_z/c_s	v_{ej}/c_s
A	5.4	10	12.4
B	5.4	7	10
C	5.4	3.8	4.6
A _{0.005}	5.4	10	12.4
A _{0.25}	5.4	10	11.7
A' _{0.25}	5.4	10	12.4
D	1.7	7	9.3
E	5.4	7	4.2 \dagger
F	1.8	20	14.6 \dagger
G	0.8	8	8.7
H	5.4	7	9.1

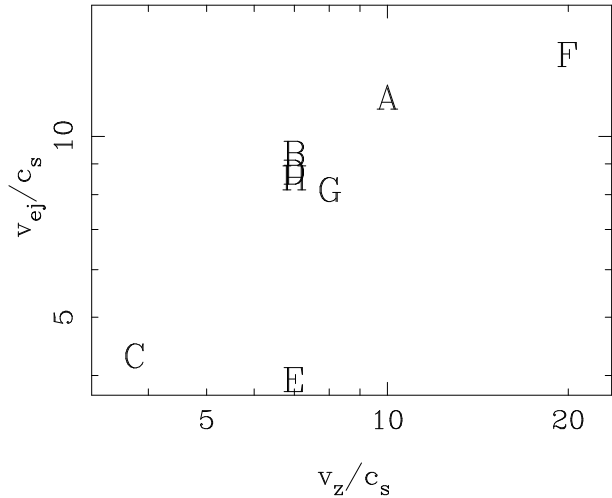


Figure 3. In this plot, we compare the outflow velocity, v_z , estimated from eq. (21) with that measured in the simulations, v_{ej} . Values are given in Table 3. A good relationship is seen, apart from in Models E and F where the assumptions underlying eq. (21) break down. In Model E the smoothing region fills much of the volume of the cluster so the cluster mass acts to suppress the outflow. In Model F, the smoothing region is unresolved by the grid, so the effective ϵ will be larger than that imposed. Models B, D and H are coincident.

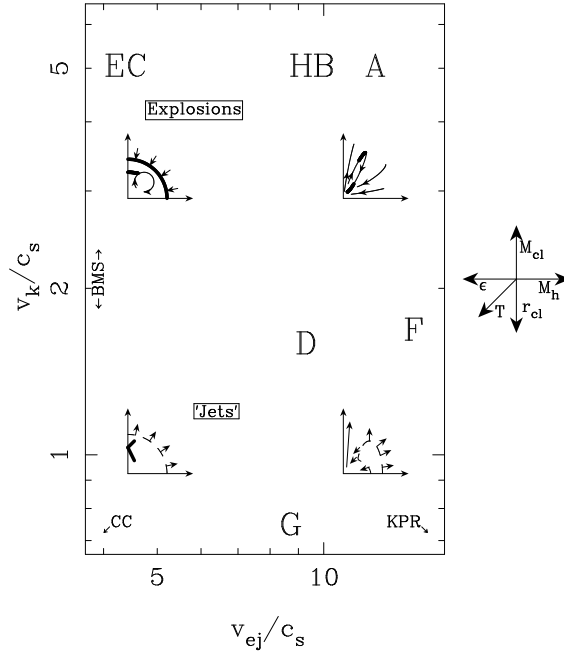


Figure 2. This graph compares the values of v_k/c_s and v_{ej}/c_s , also presented in Table 3. Smaller labels show the regimes corresponding to various models: CC – the uniformly mass-loaded, zero-gravity models of Chevalier & Clegg (1985; cf. also Williams & Dyson 1994); BMS – the disc wind models of Begelman et al. (1983); KMP – the nuclear wind models of Kippenhahn et al. and Beltrametti & Perry approximate the on-axis flows here. The small panels show the outline structures expected for each set of parameters: arrows show the directions of *supersonic* flows, solid lines show the most important shocks and dashed lines the most significant sub- to super-sonic transitions. The regions of parameter space in which we find explosions and collimated jets are labelled. The set of arrows to the right shows the directions in which models change if the variable labelled is changed.

pirical classifications and this theoretical framework. Before describing the classification scheme we preview the physical properties of the flows we find.

3.4.1 A preview of the nISM flows

Here, we preview our results, and move on, in Section 3.4.2 to the classification scheme which we have found. The details of the models are presented in Section 6. By anticipating the conclusions here, we hope the reader will be better placed to understand not only the details of the individual models, but also their relative place in the wider scheme.

In spherical models with no accreting central black hole the form of the flow is principally determined by the ratio v_K/c_s of the Kepler velocity and the sound speed in the ISM (see also Durisen & Burns 1981), where $v_K^2 \equiv GM_c/r_c$ and M_c is the core mass of the cluster. For small $v_K \lesssim c_s$, the cluster core fills with gas on a dynamical timescale and the sonic surface coincides with the edge of the cluster. By contrast, for large v_K/c_s (as in Fig. 4), most of the gas injected falls supersonically through the cluster onto a hydrostatic core at early times. Eventually this hydrostatic core fills up to the edge of the cluster, causing the inflow to cease. After this the core grows further, quasi-statically, until it reaches the sonic surface at $r_s \sim (v_K/c_s)^2 r_c$, when a steady isothermal wind is established. This scheme is illustrated by the analysis of Appendix B and the numerical models in Section 5.

The addition of an accreting black hole to the cluster fundamentally alters the structure of the nISM created by

the stellar mass-loss. The non-spherical radiation, by exerting a non-spherical force on the gas, gives rise to the in- and out-flow structures which we discuss. We have considered a wide range of models spanning the expected range of the independent parameters listed above. In this paper we present a selected set of characteristic models which illustrate the full variety of expected flow topologies. Our basic model, designated A, is the most likely physical scenario. We consider the systematic effects of changing the physical structure of the region: in models Band C we decrease the relative mass of the cluster; models A_x explore accretion (where x indicates the region of accretion); D and E have a dynamically less significant cluster; F has a diffuse cluster and a heavy black hole; G has a small and diffuse cluster. The properties of our models are given in Table 5.

In these two-dimensional models, gas which falls close to the black hole is driven outwards along the axis in a dynamical timescale. Rather than a hydrostatic core forming in the gravitational well of the central black hole, a circulatory flow forms close to the centre. In addition, the amount of mass within the nuclei can continue to vary, either because no gas escapes, as in Model C, or because it escapes in an episodic fashion, as in Model B.

The properties of the flow may also depend on the age of the nucleus. Where the central outflow drives directly out into the ambient ISM, the nuclear flow rapidly reaches an equilibrium situation: it is unlikely that the transient evolution, over a dynamical timescale, will be observed (or even occur, depending as it does on the artificial initial conditions). Age will certainly be important where most of the mass input is retained by the nucleus, since the mass con-

tent of the ISM will then increase linearly with time. Eventually, this will lead the flow to break our assumptions of low optical depth and isothermality. In the mean time, as the mass content increases, the dynamical importance of the mass loading decreases, so the density scaling works for us once more. The structure of the flows becomes a turbulent-looking plume, with an extent determined by the balance between driving and gravitational velocities, in which the gas density increases linearly with time, surrounded by a constant accretion flow which is no longer dynamically important (or observationally, as a result of its low gas pressure).

3.4.2 The classification scheme: An HR diagram for AGN?

Many authors have attempted to find out how many effective parameters determine the structure of active nuclei, using both observational data and theoretical analysis (e.g. Boroson & Green 1992; Francis et al. 1992; Blackman & Yi 1996; Donea & Biermann 1996). This may be seen as a search for diagnostics analogous to the Hertzsprung-Russell diagram, which has led to so many insights into the most stars very close to spherical symmetry: it is no surprise that the situation in AGN is substantially more difficult.

To recap, we take as the starting point for our model a galactic nucleus with an accreting black hole, surrounded by a starburst stellar cluster. We assume that the cluster can form by prior processes such as galaxy interactions. These two simple, relatively well-understood input components turn out to provide a remarkable and fascinating variety in the behaviour of the nISM. Broadly speaking, the results of our simulations can be understood in a two-dimensional theoretical classification scheme, analogous to the HR diagram.

We find that we can classify the models computed in terms of two dimensionless quantities: v_K/c_s , the ratio between stellar dynamical velocity and ISM sound speed; and v_{ej}/c_s , the Mach number of the gas driven away from the black hole along the axis of the disc. These parameters are the axes of in Fig. 2. Also shown on this figure are the codes of the various models which will be presented in Section 6 and the form of the flows which characterise each region of the plot. The flows take a variety of forms: inflow with a small core, jets, explosions and bipolar winds, as will be seen from the models themselves. The application of this plot to classifying AGN models is discussed in detail in Section 7.1.

The interaction of the axial outflow with the gravity field and the mass input of the stellar cluster determines the form of the global flow: the axial wind can be confined within the core, can escape episodically or can drive outwards as a steady flow. The overall effect is determined by a combination of whether the central outflow has more than escape velocity from the nucleus as a whole (with due account taken for mass loading), and, if so, whether it has sufficient momentum to overcome the ram pressure of the accretion flow.

The most important effect not included in the models presented here is the thermal balance of the flow. As we assume that the flow is isothermal, the two-dimensional classification of disc winds introduced by Begelman et al. (1983; and related to global flows by Williams 1999) collapses to

the axis labelled BMS on Fig. 2 – the one-dimensional classification of Section 5. While isothermality seems to be a reasonable first approximation for flows in AGN (Appendix A6), we intend to investigate the structure of radiative flows in more detail in future papers. This classification must, of course, be supplemented by the inclination angle to the observer when applied to observations.

4 NUMERICAL METHODS

These simulations were computed with a Godunov-type hydrodynamic code (Falle 1991). The method is second order in space and time in smooth regions, representing the flow with piecewise-linear variations across the computational cells. It calculates the inter-cell fluxes by solving a Riemann shock-tube problem across the cell interfaces. In the models presented here, the flow is treated as isothermal. The computational grid is two dimensional, with interfaces along the ordinates of a cylindrical polar grid.

As discussed in Section 2.3, we assume that no mass passes inwards from the galaxy to the nucleus at the outer boundaries of the grid, at large r and large z . If the nuclear flow at the grid boundary is outwards we use zero transverse gradient boundary conditions, and keep a record of the total mass and energy flows through these boundaries. This allows us both to verify mass conservation and to investigate the strength of the winds interacting with the external medium.

In some models, the mass escaping the region has too little kinetic energy to escape to infinity. It is likely that some fraction of this mass ought eventually fall back into the nucleus, probably in the accretion disc plane, after some interval. We comment elsewhere (Appendix A2) on the insensitivity of our results to the detailed form of the mass-loading (whether internal or extra-nuclear) if this input mass has low angular momentum. In the models presented here, we have chosen to keep an independent total of the ‘bound ejecta’ to compare with other mass fluxes rather than impose an arbitrary reinjection model. Experiments with larger grids and a variety of reinjection models have shown that while this artificial lowering of the barrier to escape from the nucleus changes the boundaries between the flow modes by a small amount, it does not fundamentally alter the nature of the flows.

We do not include the effects of angular velocities about the grid axis. We consider only the input of gas with low net angular momentum from stellar mass loss. Models including disc winds, although not the gravitational effect of a stellar cluster, have been calculated by Woods et al. (1996). They require treatment of both angular momentum and of wind acceleration very close to the accretion disc. The z component of angular momentum is included in those models. While essential in that case as the mass source had high angular momentum, this results in nearly empty vortices forming along the poles of the simulation, which may not be physically realistic when account is taken of non-axisymmetric perturbations to the flow.

We concentrate here on two limits, one in which there is negligible net mass transfer to the accretion disc (so that the surface $z = 0$ is just treated as a mirror plane), and another in which mass is accreted over some fraction of its surface. We determine the flux onto the accretion disc in the

latter case by making the disc surface a free flow boundary. This mimics the effect of the strong cooling which may well be driven by the high pressures found in the disc plane (e.g. Figs. 6, 7).

5 SPHERICAL MODELS

One limiting case of the flow models presented in this paper is the flow in a purely spherical system, such as an active nucleus with no anisotropic radiation, or a starburst with no black hole, or a globular cluster. Prior to presenting our main results, we present one example of a spherical flow as a test case. This can be compared with many treatments in the literature, with a variety of distributions of gravitating matter and radiative forces (e.g. KMP; Beltrametti & Perry 1980; David, Durisen & Cohn 1987). We focus on a case with no black hole and no radiation forces to illustrate the accuracy of the numerical method. Our numerical results agree well with an analytic treatment of the flow structure.

In Fig. 4, we show the structure of the flow after 4.4×10^4 yr. An accretion shock (0.5 pc from the centre of the grid) then surrounds a central hydrostatic core, and is still moving outwards. No physical instabilities operate to drive the flow far from spherical symmetry. The structure is that of a central, near-hydrostatic core surrounded by a supersonic accretion flow. The velocities in the core (Fig. 4b) reach levels as high as Mach 0.7 in one isolated region, and some striated structures appear close to the bounding shock. Some turbulence in the core would be expected in a real cluster, as a result of stirring by orbiting stars and of inhomogeneities in the infalling flow. Here, however, turbulence is driven by the jagged form of the well-resolved shock at the cluster edge and by the well-known numerical instability of slow-moving shocks (Quirk 1994), and is maintained in part by the reflective boundaries at $r = 0$ and $z = 0$ (notice the vortex at 0.15, 0.6; cf. the similar effects seen by Mellema & Frank 1995, for outgoing flows).

Beyond the sharp edge of the cluster, a near-hydrostatic atmosphere reaches outwards. The flow would only become transonic at a radius of about 25 pc (i.e. $2.5M_8T_7^{-1}$ pc), far beyond our grid. The steep density gradient in the atmosphere allows us to ignore these outer regions as they will have little dynamic effect, and only a negligible influence on the overall mass budget. This density gradient amplifies small waves at the edge of the core to generate sound waves with gas velocities up to Mach 0.2 further out in the halo. Nowhere, however, are the density contours significantly perturbed from spherical symmetry.

In Appendix B, we give an analytic derivation of the time evolution of the mass-loaded isothermal flow in an initially evacuated spherical cluster with no central black hole. In Fig. B1 we compare these results to the numerical model shown here, and find excellent agreement. The smooth curve on Fig. B1a shows the good fit of the density to the isothermal, hydrostatic solution obtained below (equation B9). The low level features of Fig. B1b within the hydrostatic core are caused by the turbulence in the core.

As the flow evolves, the hydrostatic core will become larger until eventually its outer edge, having merged with the inner accretion sonic point, reaches the outer sonic point of the flow and forms a classic Parker-type wind. Even after

Table 4. Computational Grids

Models	Cells	Size/pc	Smoothing radius/pc
ØABCAD	300×300	1.5×1.5	0.05
ESaSn	300×300	0.15×0.15	0.05
F	300×300	15×15	0.05
G	1000×1000	4×4	0.004
H	600×600	1.5×1.5	0.05

more than 4×10^4 yr the flow is far from equilibrium (cf. Figs. 4 and B1). It is likely that by the time the equilibrium solution is reached the stellar cluster will have evolved significantly. As we discuss below, the high densities which are reached in the hydrostatic core are also likely to allow bremsstrahlung cooling to become important before the core has filled, breaking our assumption of isothermality.

Adding a black hole with no aspherical radiation component or accretion simply changes the properties of the central hydrostatic core. Small accretion rates can be modelled as Bondi accretion within this core (Durisen & Burns 1981; David, Durisen & Cohn 1987): as the accretion sonic point moves further out into the core, the mass removed will weaken the wind which eventually drives outwards from the cluster (cf. Model Sa below). In the next Section, we illustrate the dramatic effects which can occur when the radiation field of the central black hole and accretion structure is aspherical.

6 ASPHERICAL MODELS

We present in this section the results for a variety of models chosen to illustrate the relative importance of the black hole mass and luminosity, the nuclear cluster and the structure of the accretion disc. If the outward driving by the accretion disc luminosity can counteract the gravitational acceleration of the black hole, its anisotropy inevitably results in a bipolar outflow. This outflow coexists with inflow from the outer regions of the cluster. The outflow funnels the inflow close to the accretion disc plane at small radii.

We explore a range of models between those in which the central flow is strong enough to drive a steady outflow, with a classic ‘bipolar’ shape, and those where it is confined (smothered) within a very small central region. At intermediate values, the flow either drives jets or sequences of explosions, depending on the ratio of the Keplerian velocity to hot phase sound speed. The balance between inflow and outflow is determined primarily by the ratio between the dynamical velocity in the cluster core and that at the smoothing radius around the central black hole.

The generalizations we draw throughout this paper about the pattern of structures which occur are based on numerous simulations – of these, those which we have chosen to present here are those with parameters close to those expected from the observations (as discussed in Appendix A), and those where the resulting nISM structures are non-trivial. If, for instance, the stellar cluster has a mass far lower than the central black hole, then its influence on the flow will be small, a situation already treated thoroughly in the literature.

In Tables 4 and 5, we list the parameters of the mod-

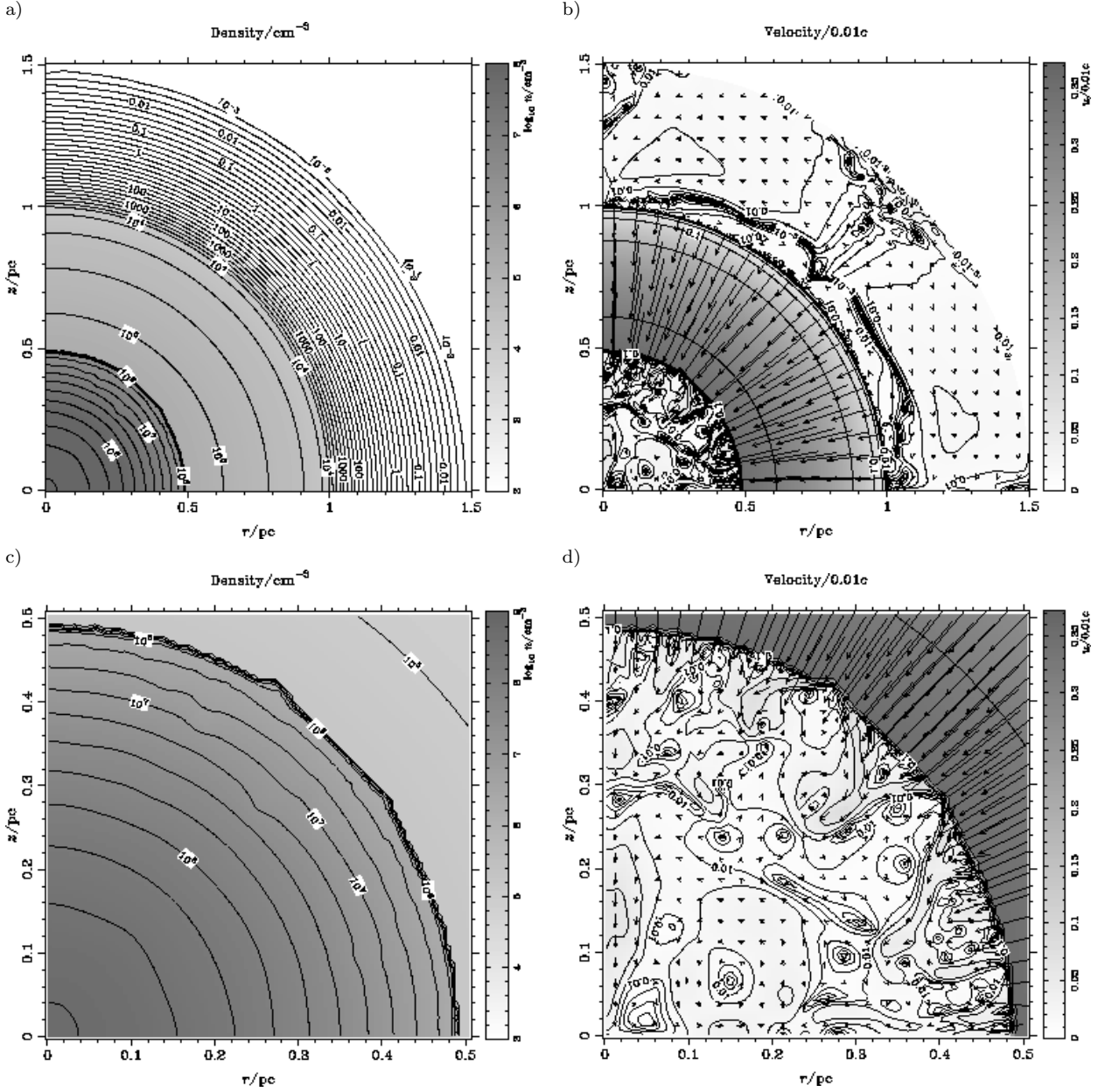


Figure 4. A spherical flow model (Model \mathcal{O} discussed in Section 5, with parameters given in Table 5) at $t = 4.4 \times 10^4$ yr. The panels show a) number density n (up to $5.6 \times 10^9 \text{ cm}^{-3}$) b) total velocity u (grey-scale and contours, up to $3.7 \times 10^{-3} c$). The vectors are in the flow direction, and have lengths proportional to the velocity, sampled at one vector in every 15×15 cells. The flow is sonic at the $u = 0.1$ contour. c) and d) are a magnification of the central 0.5×0.5 pc region (here, the vectors are every 5×5 cells). The flow structure is of spherical accretion onto a near-hydrostatic core (Appendix B).

els presented, and in Table 6 various numerical results. As can be seen, we first explore (in Models A, B, C) the balance between the dynamical velocities in the cluster and at the smoothing radius by varying the black hole parameters, leaving the cluster parameters unchanged. Next, we present models in which the accretion disc is assumed to remove gas from the flow over some fraction of its surface ($A_{0.005}$, $A_{0.25}$, $A'_{0.25}$). We then investigate the effect of varying the parameters of the stellar cluster in Models D, E and F. We look at the effects of changing other flow parameters, such as the opening angle of the central outflow (H), and of increasing the temperature of the ISM (G).

We also discuss two cases (Sa, Sn) with parameters which may be more appropriate for Seyfert galaxies. In Section 3.2 we consider in general how our results scale with the input parameters of the system.

The range of models presented are chosen to illustrate the classification which we have derived for the flow morphologies, and which we discuss in Section 3.4.

In the figures of this section, we present plots of the flow structures of our simulations. The plots are shown at the end of the computational run, or sooner if the flow reaches a steady equilibrium within this time. In all cases, the structures shown are broadly characteristic of those

Table 5. Parameters of models computed. The labels in column 1 are used to refer to these models elsewhere in the text. See Table 1 for definitions of symbols. In all the models computed, half the luminosity is in the anisotropic accretion disc component, $f_{\text{disc}} = 0.5$, and the stellar cluster core has uniform density, $s = 0$. The computational grids for each model are listed in Table 4.

Label	BH mass $M_{\text{h},8}$	mass, $M_{\text{cl},8}$	Cluster radius, $r_{\text{c,pc}}$	halo, h	Mass ratio $M_{\text{h}}/M_{\text{cl}}$	ISM temp. $T_{\text{C},7}$	$\langle f_{\text{Edd}} \rangle$	Accretion disc pc	Fig.	Comments
\emptyset	0	10	1	∞	-	1	n/a	0	4	Pure spherical cluster
A	2	10	2/3	5	0.2	1	1	0	5	Fiducial model
B	1	10	2/3	5	0.1	1	1	0	6	—
C	0.3	10	2/3	5	0.03	1	1	0	7	— Fiducial cluster; —
A _{0.005}	2	10	2/3	5	—	1	1	0 \rightarrow 0.005	13	— Changes in hole
A _{0.25}	2	10	2/3	5	0.2	1	1	0 \rightarrow 0.25	14	— and accretion
A' _{0.25}	2	10	2/3	5	—	1	1	0.25 \rightarrow 1.5	15	—
D	1	1	2/3	5	1	1	1	0	8	
E	1	1	2/30	5	1	1	1	0	9	
F	4	10	20/3	5	0.4	1	1	0	10	Relative importance of
G	1	4	3	∞	0.25	10	1	0	11	the cluster
H	10	10	2/3	5	1	1	0.7	0	12	
Sa	1	0.01	2/30	5	100	1	0.01	0 \rightarrow 5×10^{-4}	17	
Sn	1	0.01	2/30	5	100	1	0.01	0	18	

Table 6. Computational results, for the models defined in Table 5. Values are long-term averages; mass transfer rates are in $M_{\odot} \text{ yr}^{-1}$, mass content in M_{\odot} . Where values they are marked ‘?’ the simulations which had not fully relaxed (the values given are either rough averages for intrinsically variable simulations, or final ones when the flow could not be integrated to convergence).

Label	\dot{M}_{inj}	\dot{M}_{acc}	μ_{acc}	\dot{M}_{wind}	$\log(L_{\text{wind}} / \text{erg s}^{-1})$	M_{grid}	Comments
\emptyset	9.5	0	0	0	0	$\dot{M}t$	No hole
A	8.6	0	0	8.6	43.3	1.1×10^4	Steady outflow forms quickly
B	8.6	0	0	8.6	39.0:	10^5 :	Many explosions
C	8.6	0	0	0	0	$\dot{M}t$	Trapped circulation
A _{0.005}	8.6	3.2	0.37	5.4	43.1	9.4×10^3	Inner disc accretion
A _{0.25}	8.6	8.6	1	0	0	8.6×10^3	Large accretion
A' _{0.25}	8.6	3.7	0.43	4.8	43.1	8.9×10^3	Outer disc accretion
D	0.86	0	0	0.86	42.1	3.0×10^3	Small cluster
E	0.86	0	0	2×10^{-3}	38.7	$\dot{M}t$	Small cluster, const v_K
F	8.6	0	0	8.6	43.2	5.2×10^5	
G	3.8	0	0	3.7:	43.4:	1.2×10^4 :	Hot flow – jet
H	8.6	0	0	8.6	0	2.2×10^4	Narrow cone – axis force as B
Sa	8.6×10^{-3}	8.6×10^{-3}	1	0	0	0.30	‘Seyfert’ parameters
Sn	8.6×10^{-3}	0	0	0	0	$\dot{M}t$	‘Seyfert’ parameters, no accn

found throughout the evolution of the flow. The physical time which this represents varies, as the length of the run was specified in most cases by the total number of computational steps taken.

6.1 Varying the black hole mass

In the first three models (A, B, C; Figs. 5, 6 and 7, respectively), we vary the mass of the central black hole from 20 per cent down to 3 per cent of the mass of the cluster, keeping the cluster properties and Eddington ratios constant (see Table 5). Later, we present the structure of flows in systems where the black hole is relatively more massive; however, we focus first on this range of parameters since this is where mass budget requirements are best met. Also, the flows are distinct from the spherical accretion in a massive cluster illustrated in the previous section and from flows around a

black hole in the absence of a cluster. As the mass of the hole decreases, its region of influence on the global flow contracts, and the region in which the forces due to the stellar cluster dominate consequently expands.

Model A (Fig. 5) has the highest mass black hole of the first three models, $2 \times 10^8 M_{\odot}$. The flow relaxes, on a sound crossing timescale, to a steady bipolar outflow (cf. Fig. 22a, which illustrates the relaxation process revealed by the mass loss rate from the grid). The inflow in equatorial regions interacts with the outflow, and is funnelled by a shock into a dense region close to the plane. This shock is roughly coincident with the outermost section of the $n = 10^6 \text{ cm}^{-3}$ contour (which hits the r axis at 0.2 pc) in Fig. 5c, and, in Fig. 5d, is most easily seen by the sudden change in the direction of velocity vectors. A narrow, tulip shaped region of

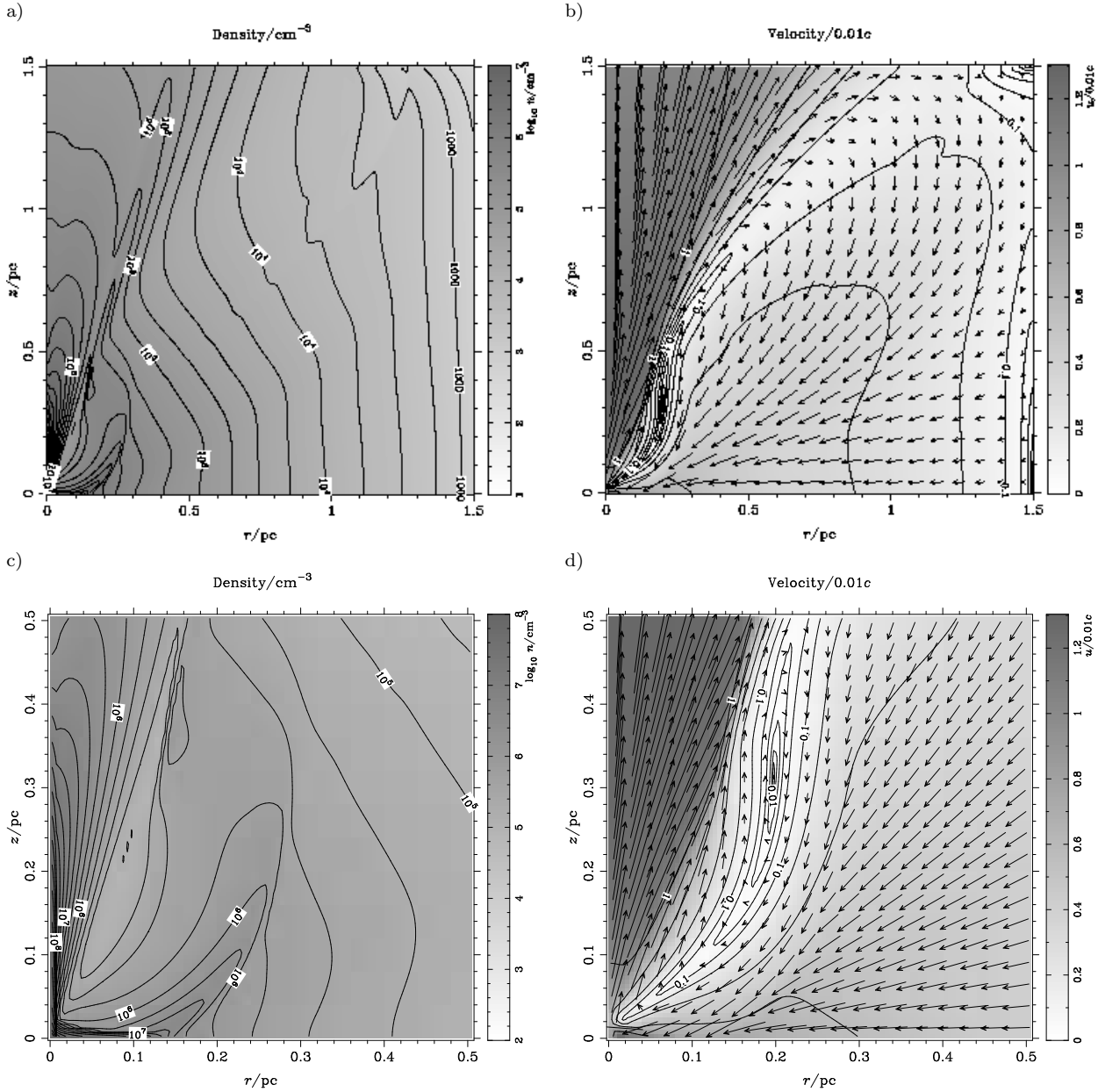


Figure 5. Model A at $t = 2.6 \times 10^4$ yr. The panels show a) density (from 323 to $1.5 \times 10^{10} \text{ cm}^{-3}$) b) total velocity (greyscale and contours, up to 1.3), c), d) Magnifications of the central region. The vectors are in the flow direction, and have lengths proportional to the velocity, sampled at one vector in every 15×15 cells in b), every 5×5 cells in d). The flow is sonic at the $u = 0.1$ contour.

circulating, subsonic flow separates the inflow and outflow regions.

The sonic surface separates flow above and below the sound speed. In general the streamlines are almost in the plane of the sonic surface, although both inflow and outflow from the region are seen close to its ends. Even at the ends, the flow is reasonably well-resolved, giving us confidence that the transition from shock to sub-sonic to super-sonic transition through the parallel sonic flow observed here is a real feature. Note, however, that this sonic transition coincides with the outer radius of the region in which the forces are smoothed, and will move inwards if the physical ‘smoothing region’ is smaller than that assumed here.

At the centre of the grid, much of the outflow is con-

centrated in the grid cells adjacent to the axis (the individual cells are 5×10^{-3} pc square). The flow is confined by the inward radial velocities found in these cells (not visible in the selected cells shown in Fig. 5b or d), a well-known difficulty for axisymmetric hydrodynamical codes. However, since the flow here is more-or-less ballistic, and the gravitational and radiation forces acting on the gas are chosen to vary smoothly with angle, this should not have a strong influence on the results. This is confirmed by the smoothness of the velocity field shown by the contours in Fig. 5d.

Model B (Fig. 6) has a central black hole of $10^8 M_\odot$, half the mass assumed in Model A. The gravity of the cluster and the friction of the mass loading are now sufficient to

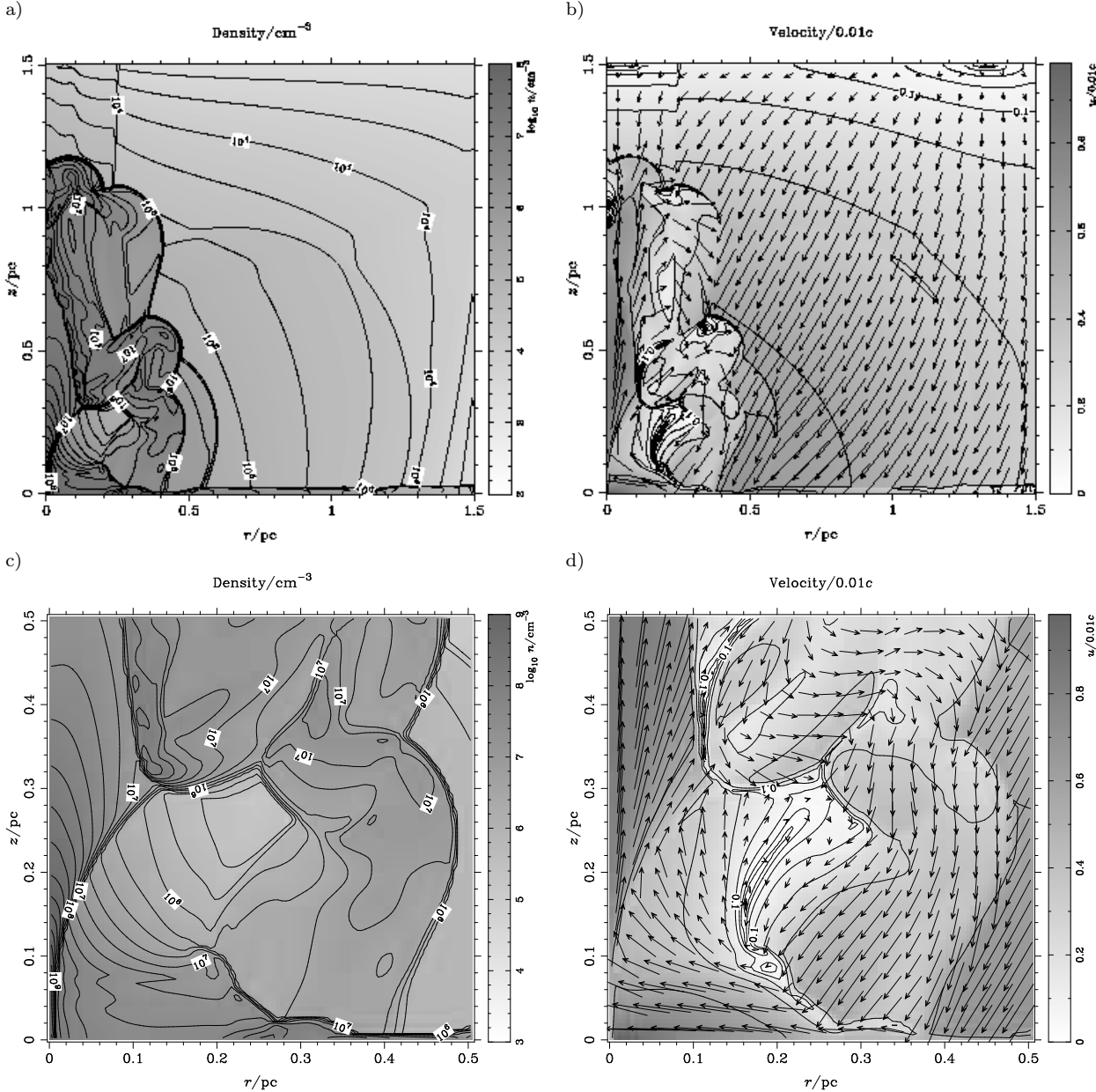


Figure 6. Model B at $t = 6 \times 10^4$ yr. The panels are as in Figure 5, except that the density range is from 1800 to $2 \times 10^{10} \text{ cm}^{-3}$ and velocities reach $0.01c$.

stagnate the flow within the cluster. Unsteady structures develop, and a sequence of explosions drive out from the region. Strong shocks are distributed throughout the region where the inflow from the outer cluster interacts with the central core; in the plane of the disc (over the surface of which a thin plate of very dense, infalling gas forms at radii between 0.5 and 1.5 pc), and (as bowshocks) around clumps which form in the flow [on axis at $z = 1$ pc, and at $(r, z) = (0.12, 0.32)$]. Where shocks cross each other, regions of particularly enhanced density (and pressure) are formed, although this pressurization will be transient and may not be important for generating cool gas.

In some cases, these clumps develop an independent identity, and fall from the strong outflows close to the axis, where they are confined by ram-pressure, towards the plane

of the accretion disc. However, as they leave the central outflow region the ram pressure of the flow decreases rapidly, so the clumps explode and drive shocks into the accreting flow.

We discuss the mass budget of this model further in Section 7.5.

Model C (Fig. 7) has a yet lower mass hole, $3 \times 10^7 M_\odot$. The accreted gas collects in a mildly unsteady, convective structure at the centre of the grid. Essentially no mass is lost from the central parsec-scale region over the 10^5 yr for which the simulation was run, although the density and size of the central structure gradually increases with time. At the end of the simulation, the mass contained in the grid was $9 \times 10^7 M_\odot$, and the mean mass loss rate was roughly

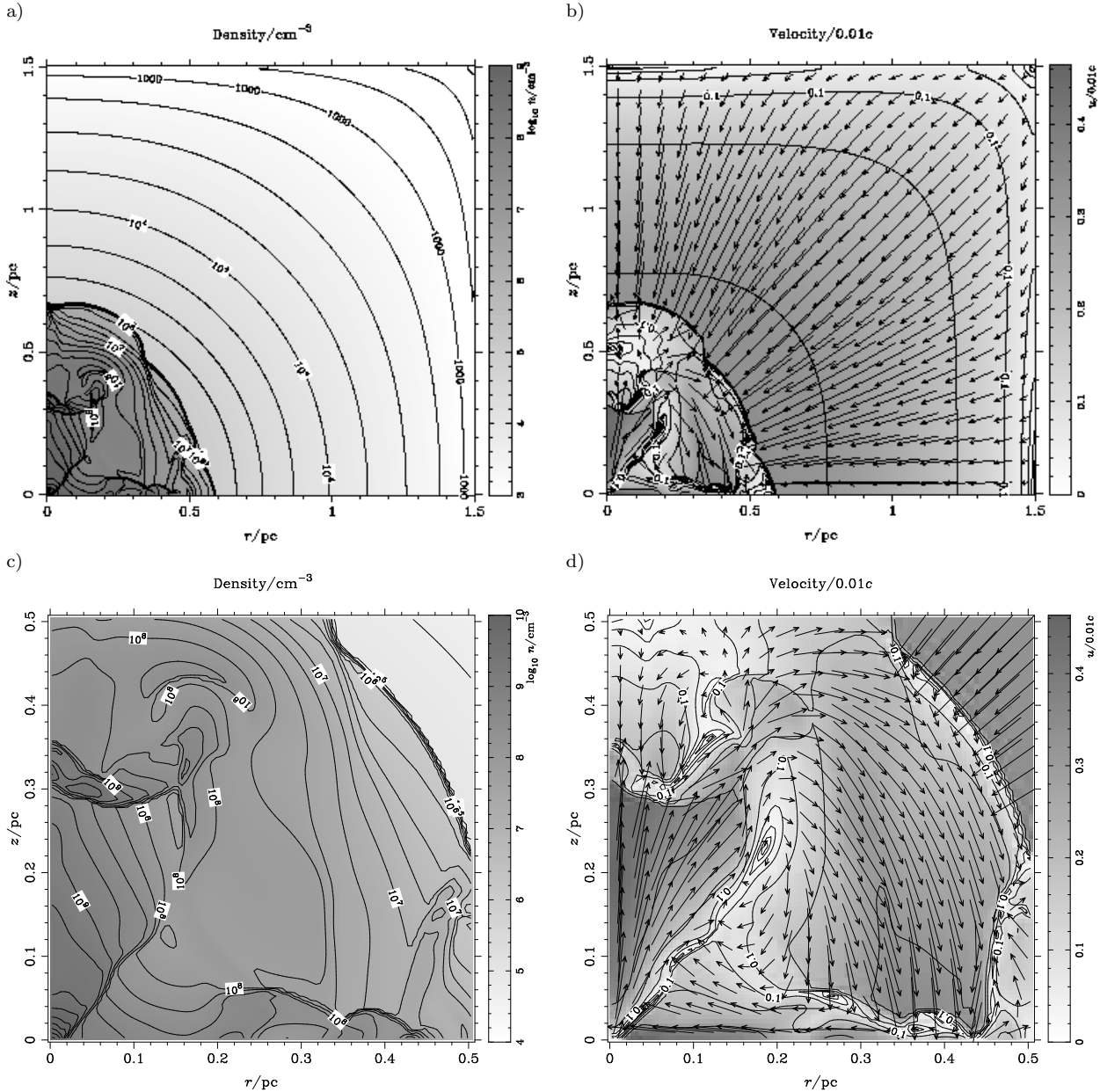


Figure 7. Model C at $t = 10^5$ yr. The panels are as in Fig. 5, except that the density range is from 2330 to $1 \times 10^{11} \text{ cm}^{-3}$ and velocities reach $4.6 \times 10^{-3}c$.

$10^{-3} M_\odot \text{ yr}^{-1}$. This total is entirely dominated by gas with less than escape velocity flowing out from the edges of the accreting flow. Later, once outflows begin to be driven by the central convective structure this mass loss rate will begin to increase. Even if this were to occur as early as the time illustrated in Fig. 7, and if thereafter the mass loss rate were to increase in proportion to the flow density (hence roughly linearly in time), it would still require 5000 times the length of the current simulation before a balanced mass budget could be reached. However, it seems likely that the flow will remain unsteady in this eventual state, as in Model B, with episodic loss of a tiny fraction of the ISM mass.

The structure of the flow is broadly similar to that of Model B. Features to note are the dense plate of gas on axis at $z = 0.3 \text{ pc}$, which forms where the inflowing halo gas and

outflowing wind meet. Oscillations of this plate drive weak shocks into the halo, and modulate the rate at which gas falls back towards the plane of the accretion disc. The three-limbed structure of shocks and sonic surfaces seen here is worth noting. It also appears in many other cases (but compare the single ‘tulip’ in Model A). Gas injected close to the stagnation point does not accelerate monotonically: rather, it spirals around in increasing spirals, passing through a sequence of shocks until finally it can escape.

6.2 Varying the stellar cluster properties

We now discuss a selection of models which investigate variations in the parameters of the stellar cluster. In Models D and E, the cluster mass is reduced. In Model D, we choose

the radius of the cluster to be the same as Model B. In Model E, we choose the dynamical velocity of the stars to be roughly constant. In Models D and F, we investigate the behaviour of the flow as the Keplerian velocity decreases relative to the sound speed, where F has a rather higher velocity of ejection from the central region than D.

Models D and F can be paired with models A and B, respectively, except that they have relatively small stellar velocity dispersions (scaled to the sound speed of the flow, cf. Fig. 2).

Model G has an cluster with a Keplerian velocity rather smaller than the sound speed in the nISM. As a result, the flow inside the cluster core is quasi-hydrostatic, rather than the supersonic accretion flow found in most of the other simulations presented here. Much of the mass loss from the cluster occurs in a spherical wind. A strong outflow is, however, still driven from the centre of the grid, and a recollimating jet is formed as this interacts with the core.

Model D (Fig. 8) has a lower cluster mass than Model B, but the same cluster core radius. Deceleration by gravity and mass loading have both decreased, and the flow can now drive freely from the centre along the axis of the grid.

Compared to Model A, the nISM has been made dynamically ‘hotter’ – i.e. the ratio v_K/c_s has been decreased. The opening angle of the flow which escapes the cluster core has been substantially increased. As expected, the sonic region substantially expanded; it provides significant support against gravity for the gas falling in the accretion disc plane, allowing the central outflow to widen. However, it should also be noted that with $M_h = M_{cl}$, the radiation forces retain a significant influence out to the edge of the cluster. This encourages the free outflow of gas along the axis.

Model E (Fig. 9) also has a lower cluster mass than A, and has a far smaller cluster core. Weak shocks are sent into the circumnuclear ISM. At the end of the simulation, the mass contained in the grid was $7.6 \times 10^3 M_\odot$, and the mean mass loss rate was roughly $2 \times 10^{-3} M_\odot \text{ yr}^{-1}$. This mass loss was dominated by gas with sufficient energy to escape the nucleus. In this regime, the mass loss rate roughly scales with the mass within the grid: a balanced mass budget would be expected after $4 \times 10^6 \text{ yr}$, 500 times later than the picture presented in the figure.

Here again we see a three-limbed sonic surface spreading out through the cluster (note the $v/0.01c = 0.1$ contour in Fig. 9d, which is in this case well within the extended smoothing region). At the very centre of the grid, the disc inflow shocks into a compact, dense and largely subsonic structure. The end of one of the three limbs seems to act as a de Laval nozzle, at $(0.004, 0.008)$, where the flow becomes supersonic. The flow in and around this nozzle is very variable. This results, for the most part, from the variation of the inflow on the disc plane: flow instabilities are expected to be suppressed in squat nozzles such as this one (Smith et al. 1983). The small mass of the cluster in this simulation means that the flow continues to be accelerated beyond the nozzle, until it reaches the termination shock which oscillates about 0.06 pc.

Note that for the parameters assumed in this case, the stellar cluster will be highly collisional. As we have discussed, the solution can simply be scaled to different pa-

rameters to avoid this constraint. However, we have chosen here to keep the parameters of the BH and accretion disc the same as in Model B, and as a result sacrificed this freedom.

Model F (Fig. 10) has a cluster with a far larger core radius than Model A, but with the same cluster mass. It extends our coverage of parameter space to higher ejection velocities than Model D, but with a lower cluster dispersion than A. Hence, the cluster takes up a far larger fraction of the Parker radius of 25 pc. Comparing Figs. 10 and Fig. 5, the subsonic region has inflated from a narrow tulip to take up a broad region of the flow. The decreased flow velocities in this region have removed the weak shocks close to the accretion disc. Funnelling of the flow by the broadened subsonic region has acted to offset the decrease in mass flux in the inflow region, keeping the density here roughly constant. The velocity and opening angle of the outflow are fairly similar between the models, so the densities (at a given fraction of the cluster core radius) are about 100 times smaller in Model F than in Model A – in Model F, the axial outflow is less dense than the surrounding cluster ISM, in contrast to most of the other models presented here.

Model G (Fig. 11) has an extremely low cluster core density and a very hot ISM. Looking at Fig. 2, we see that Model G is an extreme case in our modelling. The Parker radius is 1 pc, within the cluster core. If there were no black hole, the flow would relax on a dynamical timescale to a subsonic core with a sonic transition on its surface, hardly altered by the effects of gravity (cf. Chevalier & Clegg 1985; Williams & Dyson 1994). Even when a black hole is present, the sonic transition coincides with the edge of the cluster over much of its surface, and a substantial fraction of the mass loss flows out in this global wind. In Model G, the central outflow is highly supersonic. Interestingly, this weakly collimated central flow is soon recollimated by the hydrostatic pressure of the core: it recollimates three times within the core, to generate a supersonic outflow region with a high aspect ratio – a genuine jet.

Structures similar to these have previously been studied in work following on from that of Blandford & Rees (1974; see also Wiita 1978a). These authors modelled the outflow driven by a central injection of energy, accelerated to supersonic velocities by de Laval nozzles confined by the pressure of the surrounding nISM. The original models treated the funnel as very long and thin, but these long funnels were found to be unstable to Kelvin-Helmholtz instabilities, resulting in the loss of gas in a series of bubbles rather than a continuous jet (Gull & Northover 1973; Wiita 1978b; Norman et al. 1981). For rather higher injection luminosities, continuous outflows do occur (Smith et al. 1981; Smith et al. 1983). However, in the latter cases the neck of the funnel was close to the termination shock of the central wind. In consequence, the ‘jets’ so formed were only slightly supersonic, and poorly collimated. Here we find that a dense hydrostatic envelope can indeed lead to the formation of a well-collimated jet with a substantial Mach number, if a highly supersonic but ill-collimated flow is driven from the centre.

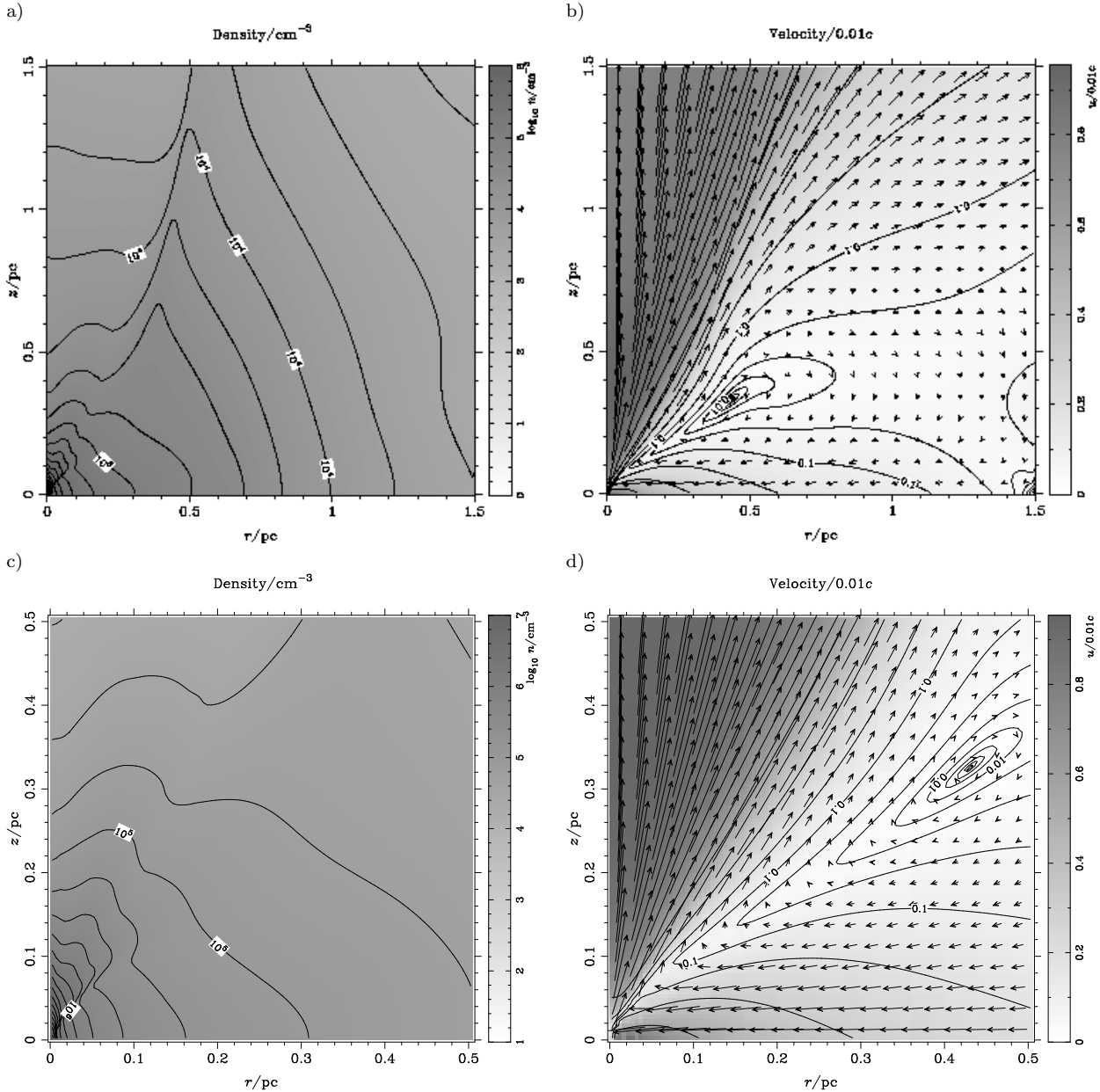


Figure 8. Model D at 6×10^4 yr (steady equilibrium solution). The panels show a) density (from 1513 to $4 \times 10^8 \text{ cm}^{-3}$) b) total velocity (greyscale and contours, up to 0.95), c, d) Magnifications of the central region. The vectors are in the flow direction, and have lengths proportional to the velocity, sampled at one vector in every 15×15 cells. The flow is sonic at the $u = 0.1$ contour.

6.3 Varying the distribution of radiation

Model H (Fig. 12) has parameters identical to those of Model B, except for the Eddington ratio. The net force is the same along the axis of the disc as in Model B, but is outwards in a cone with far smaller opening angle, and the inward force in the plane of the accretion disc is far greater. Model H quickly relaxes to a steady outflow, albeit with no mass leaving the cluster with escape velocity, whereas Model B underwent a series of explosions. However, the flow structure of Model B close to its long-lived mass minimum of $3 \times 10^4 \text{ M}_\odot$ at 2×10^5 yr (see Fig. 22a) is almost indistinguishable from that of the equilibrium state of Model H. Altogether, comparison of models B and H indicates that

the opening angle of the central outflow has little influence on the overall flow structure, if the cluster gravity and mass input are significant factors.

6.4 Accretion over part of the disc

We next investigate the effect of accretion on the global flows. We assume that the accretion from the flow onto the thin disc occurs either in its innermost region (Model A_{0.005}), over a large fraction of its inner surface (Model A_{0.25}) or over a large fraction of its outer disc (Model A_{0.25}'). These models cover a range of ways in which mass might be lost from the global flow to the accretion disc. As accretion tends to weaken the net outflow from the central regions,

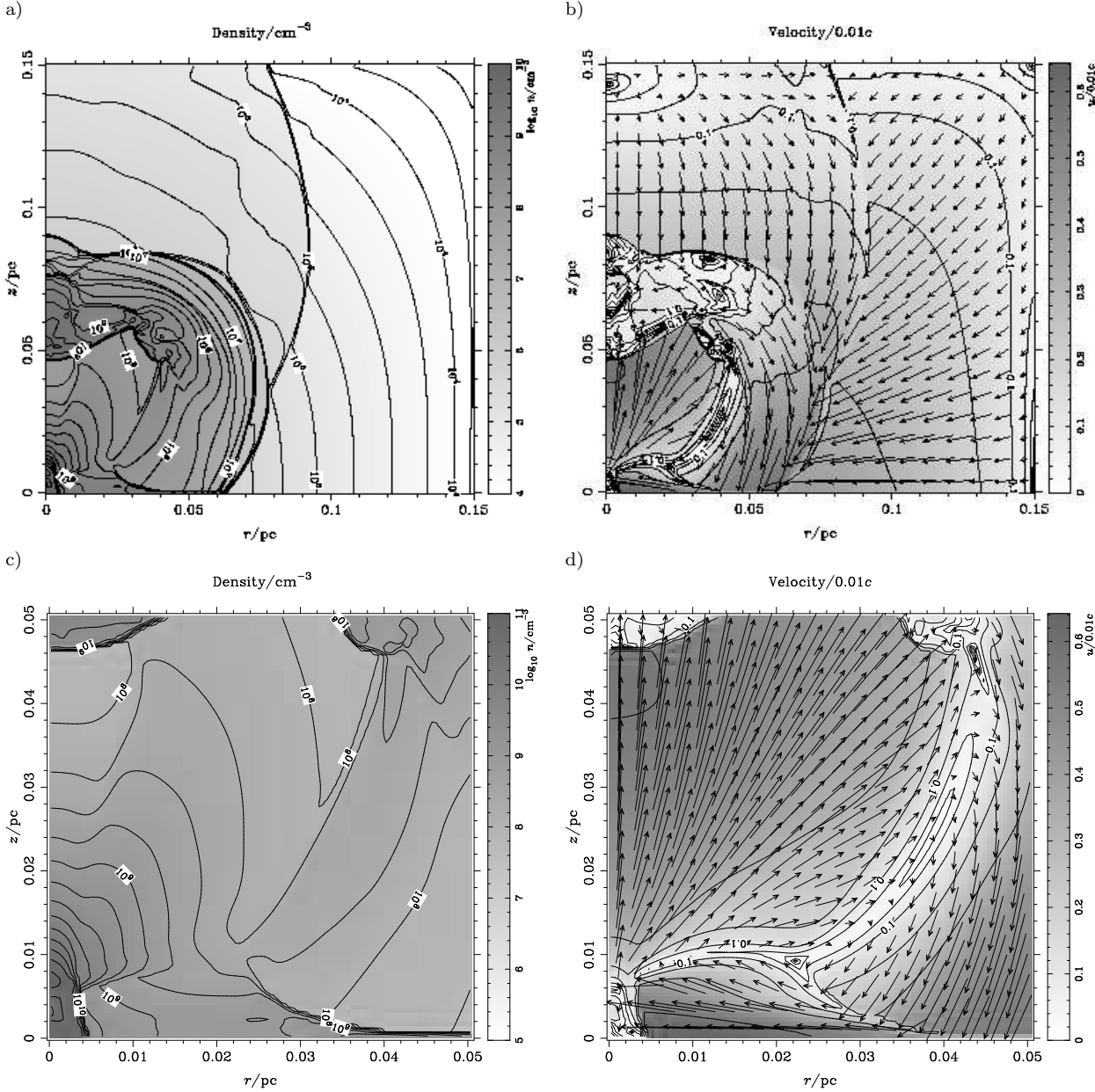


Figure 9. Model E at 9×10^3 yr (note that this simulation is on a small scale, so the dynamical timescale is short). The smoothing scale here is 0.05 pc, the same as in models C, A and B, and takes up a large fraction of the grid. The panels show a) density (from 2100 to 10^{11} cm^{-3}) b) total velocity (greyscale and contours, up to 0.64), c), d) Magnifications of the central region. The vectors are in the flow direction, and have lengths proportional to the velocity, sampled at one vector in every 15×15 cells. The flow is sonic at the $u = 0.1$ contour.

we use parameters which are perturbations of those used in Model A above, which has the strongest initial outflow.

Models A_{0.005} and A'_{0.25}, Figs. 13 and 15, evolve in a manner nearly identical to model A, even though around 40 per cent of the input mass flux is diverted into the accretion disc rather than the wind.

There is a striking similarity between the flows illustrated in Figs. 13 and 15. This extends even to the evolution of detailed time-dependent features, such as mass clumps on axis (Fig. 16). In one, mass is removed from the simulation at the very centre of the grid, in the other across a wide area of the outer disc. Some signature of this can be seen in the re-

gions closest to the r -axis in the figures, beyond $r = 0.25$ pc. Overall, the comparison illustrates convincingly the independence of the form of the solutions from the detailed distribution of mass input, or in this case mass removal, so long as the total mass budget is similar.

With its substantially larger area of accretion, the outflow in model A_{0.25} has been weakened so much that the flow structure is more reminiscent of Model C, except with dramatically smaller densities in the flow (10^6 cm^{-3} is characteristic, compared to 10^9 cm^{-3} in Model C), and with a far narrower collar of shocked gas at the base of the central outflow.

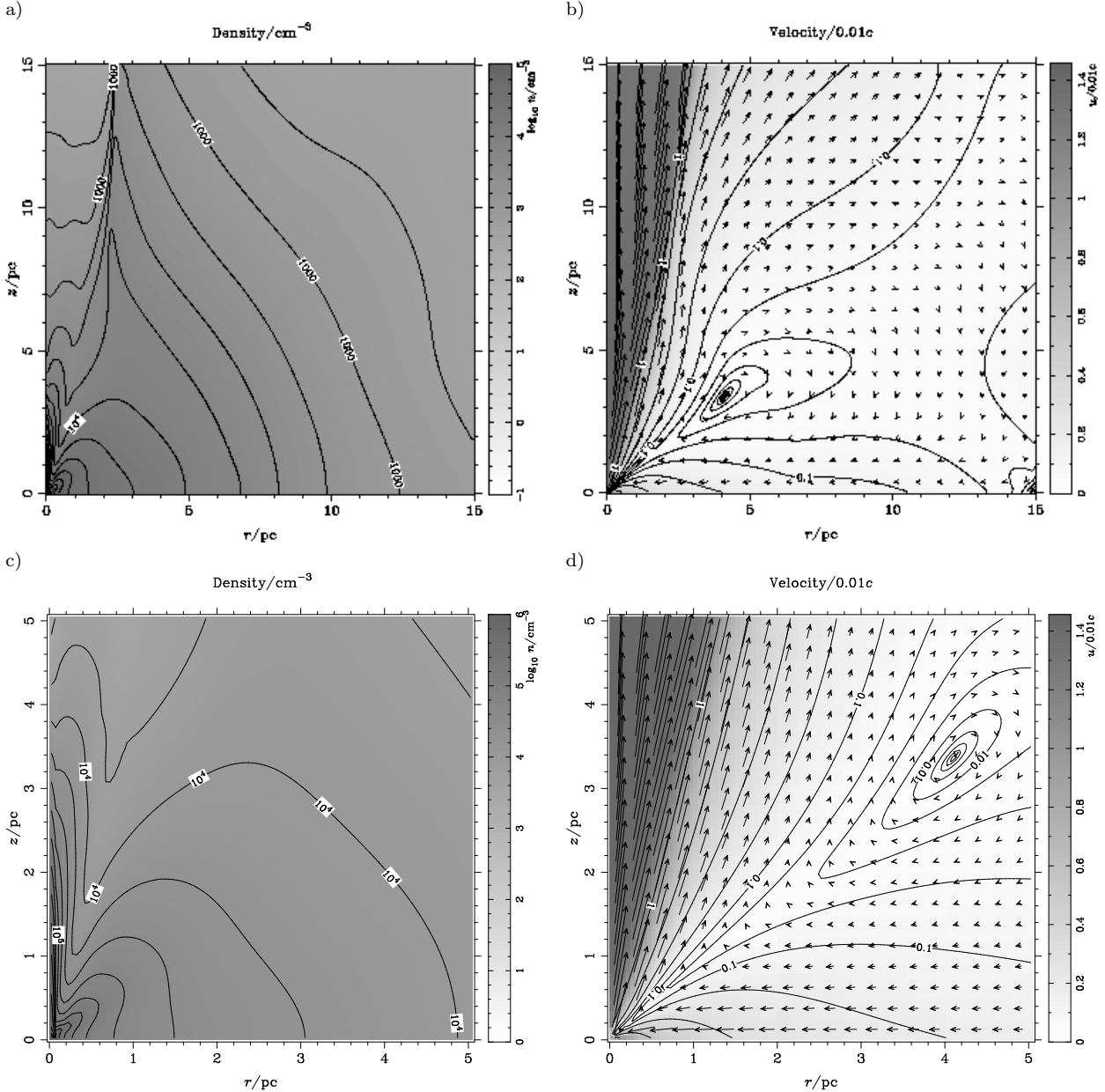


Figure 10. Model F at 4.2×10^5 yr. The panels show a) density (from 350 to $7.5 \times 10^7 \text{ cm}^{-3}$) b) total velocity (greyscale and contours, up to 1.46), c), d) Magnifications of the central region. The vectors are in the flow direction, and have lengths proportional to the velocity, sampled at one vector in every 15×15 cells. The flow is sonic at the $u = 0.1$ contour.

6.5 Low Eddington ratio

The models described so far in this section were for bright QSOs. We now consider the effects of changes in parameters to values characteristics of Seyfert nuclei.

The similarity in line widths and profiles between AGN of widely differing luminosities can be interpreted as implying that the kinematics are similar. If this is so, in Seyfert nuclei the characteristic length and timescales must be $\lambda \simeq \tau \simeq 0.01$, relative to the QSO case. If the Eddington ratio, etc., remain constant then such a self-consistent Seyfert model would have masses smaller than those of QSOs by λ , and densities increased by $1/\lambda$. The ionization parameter remains constant so long as Q is determined to within

a small factor by stellar physics. In this case, the ratio between cooling and flow times is constant, and the models scale directly from those presented above (see also the next subsection).

However, many authors find black hole masses in Seyferts $\sim 10^8 M_\odot$ (as might be expected in an old QSO brought back to life), requiring that accretion is sub-Eddington (Padovani, Burg & Edelson 1990; Lasota et al. 1996). Structures similar to those shown in the preceding subsections would persist if the efficiency of outward radiation driving were increased (cf. Section 7.4).

However, if there is no such enhanced driving the topology of the flows changes radically, as we have discussed from scaling arguments in Section 3.3.2. In this subsection, we

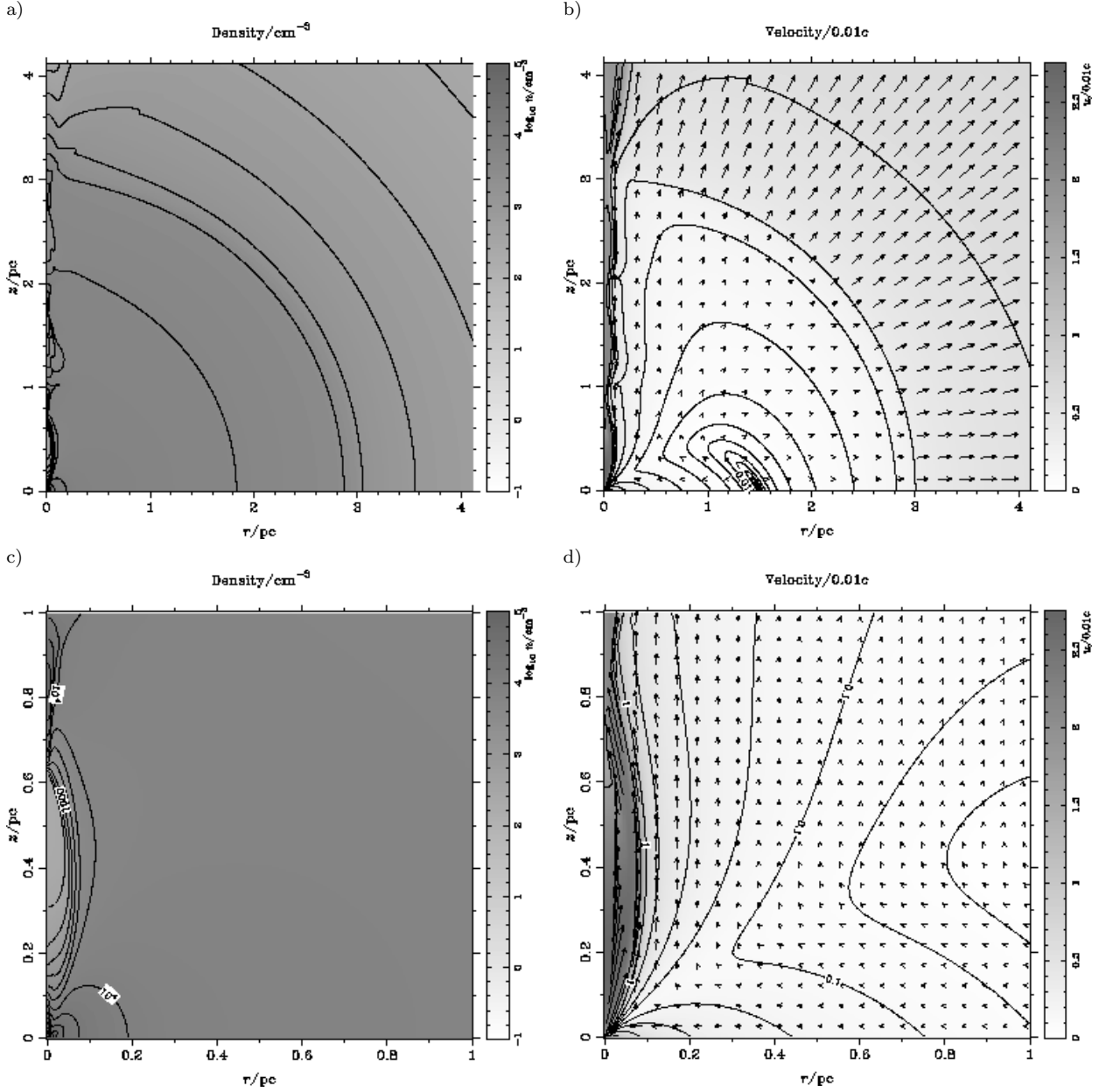


Figure 11. Model G at 9×10^3 yr. As this simulation was very time-consuming, it was halted at this stage, before the solution had reached equilibrium. However, since the wind mass loss has reached 97 per cent of the injection rate, and little movement was seen in the solution, these plots should be fairly representative of the eventual equilibrium. The panels show a) density (from 211 to 10^7 cm^{-3}) b) total velocity (greyscale and contours, up to 2.7 , note that for the gas temperature of 10^8 K used here, the sound speed is 0.32 so this corresponds to a peak Mach number of 8.7), c), d) Magnifications of the central region. The vectors are in the flow direction, and have lengths proportional to the velocity, sampled at one vector in every 32×32 cells in b), every 7×7 in d). A jet close to the axis passes through recollimation shocks which reach the axis at 1 , 2 and 3 pc before it escapes the cluster core.

present numerical results for the case in which there is no increased driving. We consider a black hole mass of $10^8 M_\odot$, but a cluster mass of only $10^6 M_\odot$, sufficient to power accretion at luminosity $10^{44} \text{ erg s}^{-1}$, i.e. about $0.01 L_{\text{Edd}}$. (We shall see that the form of the flow is similar to that for a low mass-loss cluster of $10^8 M_\odot$, as might be expected in a ‘fossil QSO’ nucleus.) In order that stellar collisions do not dominate the mass input, the core radius of the cluster must be larger than 0.07 pc (note that in this case the stellar velocities will be dominated by the mass of the black

hole). This core radius is an order of magnitude greater than variability-based estimates of the size of the BELR (e.g. Peterson 1994), which suggests that the BELR lies entirely within the cluster core.

We calculated two models, with and without central accretion (Figs. 17 and 18, respectively). In both, we found near-spherical inflows of the nISM throughout the nucleus, except for a small hydrostatic core in model Sn.

These low Eddington ratio models do not show the bipolar structures characteristic of the QSO models, and

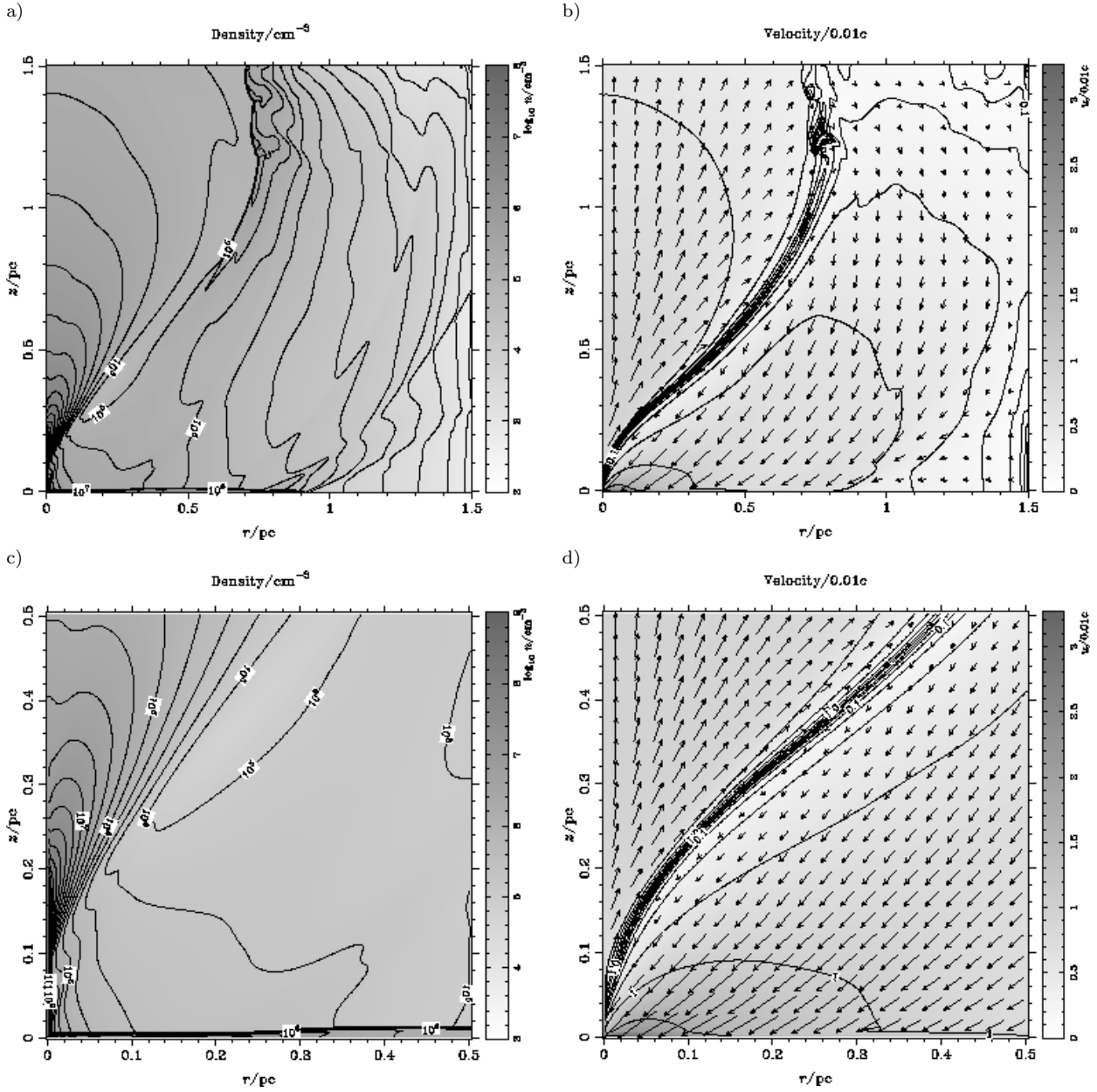


Figure 12. Model H at 2×10^4 yr. The panels show a) density (from 400 to $2 \times 10^{11} \text{ cm}^{-3}$) b) total velocity (greyscale and contours, up to 3.3), c), d) Magnifications of the central region. The vectors are in the flow direction, and have lengths proportional to the velocity, sampled at one vector in every 31×31 cells. The flow is sonic at the $u = 0.1$ contour.

as observed in radio maps of Seyfert galaxies. This is because the accretion disc luminosity is only a fraction of the (insignificant) radiation force. Spherical inflow will characterise Seyferts with $f_{\text{Edd}} \ll 1$ if the opacity is dominated by Thomson scattering. Observations imply that other sources of opacity will produce bipolar flows in Seyferts. The signature of this radial inflow should be detectable in the variability of line profiles, with the red wings of the lines leading the blue. For the smaller nuclei observed in Seyfert galaxies, individual supernovae will often evacuate the entire nuclear ISM (Perry, Williams & Dyson 1999) returning the flow to initial conditions similar to those we have assumed for our simulations.

7 DISCUSSION: THE PROPERTIES OF FLOWS IN ACTIVE NUCLEI

We have modelled the central region of an AGN, assuming only that a black hole and accretion disc with an aspherical radiation field is embedded in a young starburst stellar cluster. These two simple components give rise, symbiotically, to a nuclear interstellar medium with a remarkable and fascinating variety of structures. Despite the absence, in our models, of any effects due to radio-related phenomena, the nISM shows a range of behaviour normally associated with relativistic effects near the black hole: episodic, explosive, percolating structures, and/or well collimated, hypersonic hydrodynamic jets – given only that the radiation

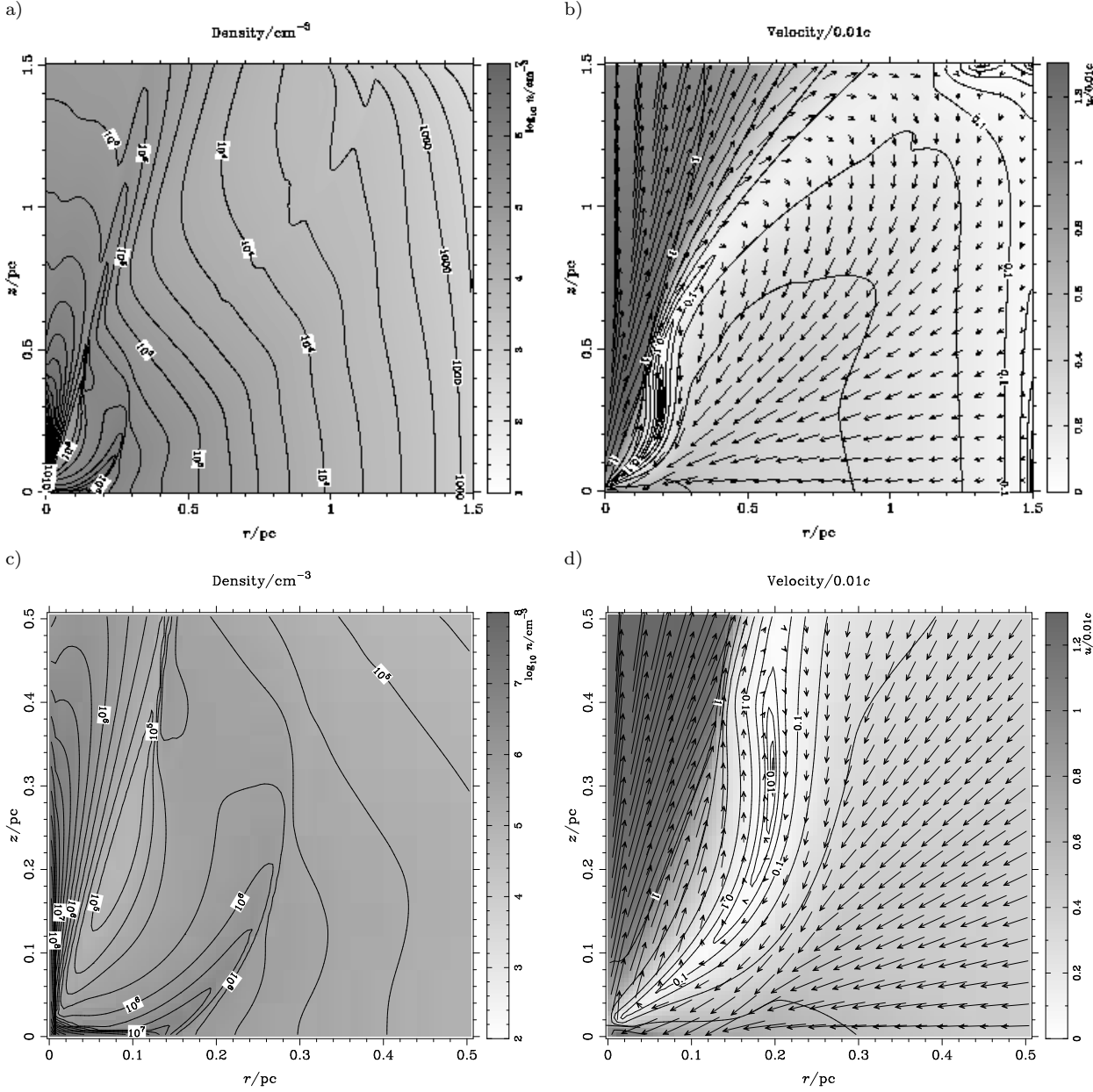


Figure 13. Model A_{0.005} at 1.8×10^4 yr (steady equilibrium solution). The panels show a) density (from 191 to $1.1 \times 10^{10} \text{ cm}^{-3}$) b) total velocity (greyscale and contours, up to 1.3), c), d) Magnifications of the central region. The vectors are in the flow direction, and have lengths proportional to the velocity, sampled at one vector in every 15×15 cells. The flow is sonic at the $u = 0.1$ contour.

field drives an outward flow along the axis of the disc. When the Keplerian velocities of the stars, v_K , are $\gg c_s$, the black hole drives a meridional flow within the previous hydrostatic core. The mass-loaded outflow from the core is either confined by an (apparently very unstable) internal termination shock or can drive gas beyond the cluster core, in episodic explosions or as a continuous wind. For smaller v_K/c_s , confined jets can form on-axis. In all cases where a wind drives out through the nucleus, it has a half-opening angle which is rather smaller than that of the (conical) region close to the centre within which the net force is outwards (typically 30 degrees compared to 60 degrees).

The models we present here are distinguished from previous studies by the effects of the stellar cluster and by the

nature of the flow at small radii. The poorly collimated central wind from the very centre of the grid drives outwards supersonically into the cluster. When this outflow has sufficiently great momentum, it blows straight through the cluster and onwards into the galaxy ISM: such flows soon settle to steady equilibria. For lower momentum flows, the outflow shocks against the inflowing nISM of the cluster, and falls back to the core in a circulation. In some cases, a series of explosions are found; rather than buoyancy-driven bubbles, these are pushed outwards by the recycling of matter through the black hole core. The timescale for these explosions is the dynamical timescale of the nuclei, which will vary between roughly 300 yr in QSOs and 3 yr in Seyfert galaxies. These times, too long to explain continuum vari-

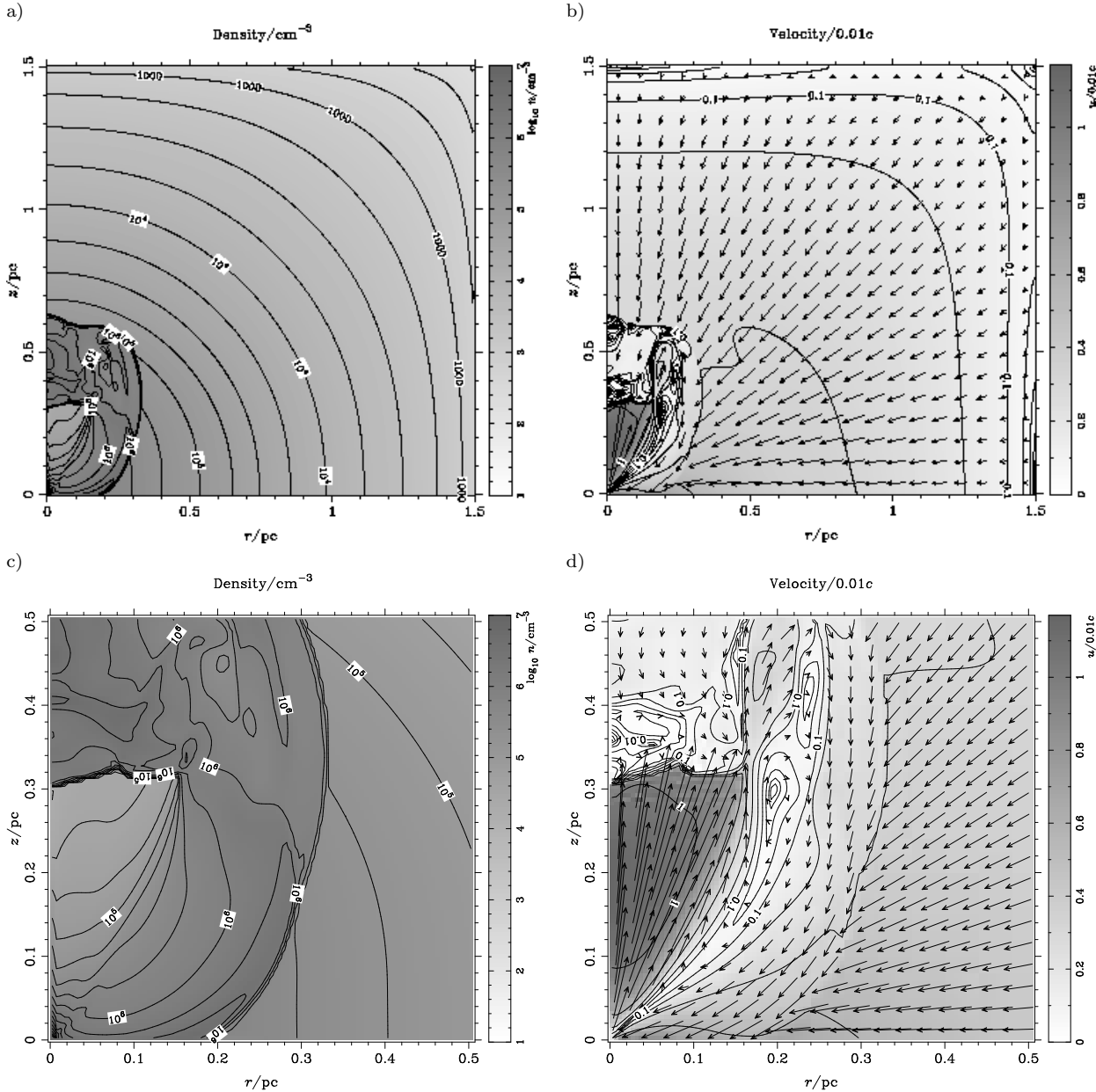


Figure 14. Model A0.25 at 5.1×10^4 yr. The flow here is oscillating, cf. Fig. 23. The panels show a) density (from 171 to $5.1 \times 10^8 \text{ cm}^{-3}$) b) total velocity (greyscale and contours, up to 1.2), c), d) Magnifications of the central region. The vectors are in the flow direction, and have lengths proportional to the velocity, sampled at one vector in every 15×15 cells. The flow is sonic at the $u = 0.1$ contour.

ability, may relate to variations in the underlying structure of line-emitting gas (Perry, van Groningen & Wanders 1994; Wanders & Peterson 1996).

Gas which rains onto the disc in many of our models may also suppress the wind from some part of its surface. If the gas in this region can cool, it will irradiate the outer disc and may have important ramifications for angular momentum transport in the disc.

The structures we predict for the flows are very sensitive to the central luminosity, if it is close to the (on-axis) Eddington limit. The boundary between stagnated inflow and free, steady outflow is fine, depending on whether transient explosions can drive significant mass from the nucleus. Indeed, there seem to be bimodal solutions in some cases,

where the flow can take either a low-mass, free-outflow or high-mass, recirculating form. Quite small changes in luminosity may lead to ejection of large masses of nISM gas within the dynamical timescale of the nuclear flow. In a fully self-consistent model, variations may be even more catastrophic than those presented here (although these variations may be damped by lags due to viscous transport within the accretion disc).

In many cases the time-steady system does not lead to structures in the nISM which are time steady, unlike the models of the wind from the surface of a molecular torus by Balsara & Krolik (1993). Our results indicate that the flows may remain chaotic for all time, with shocks forming an important part of the structure. In the models of Balsara

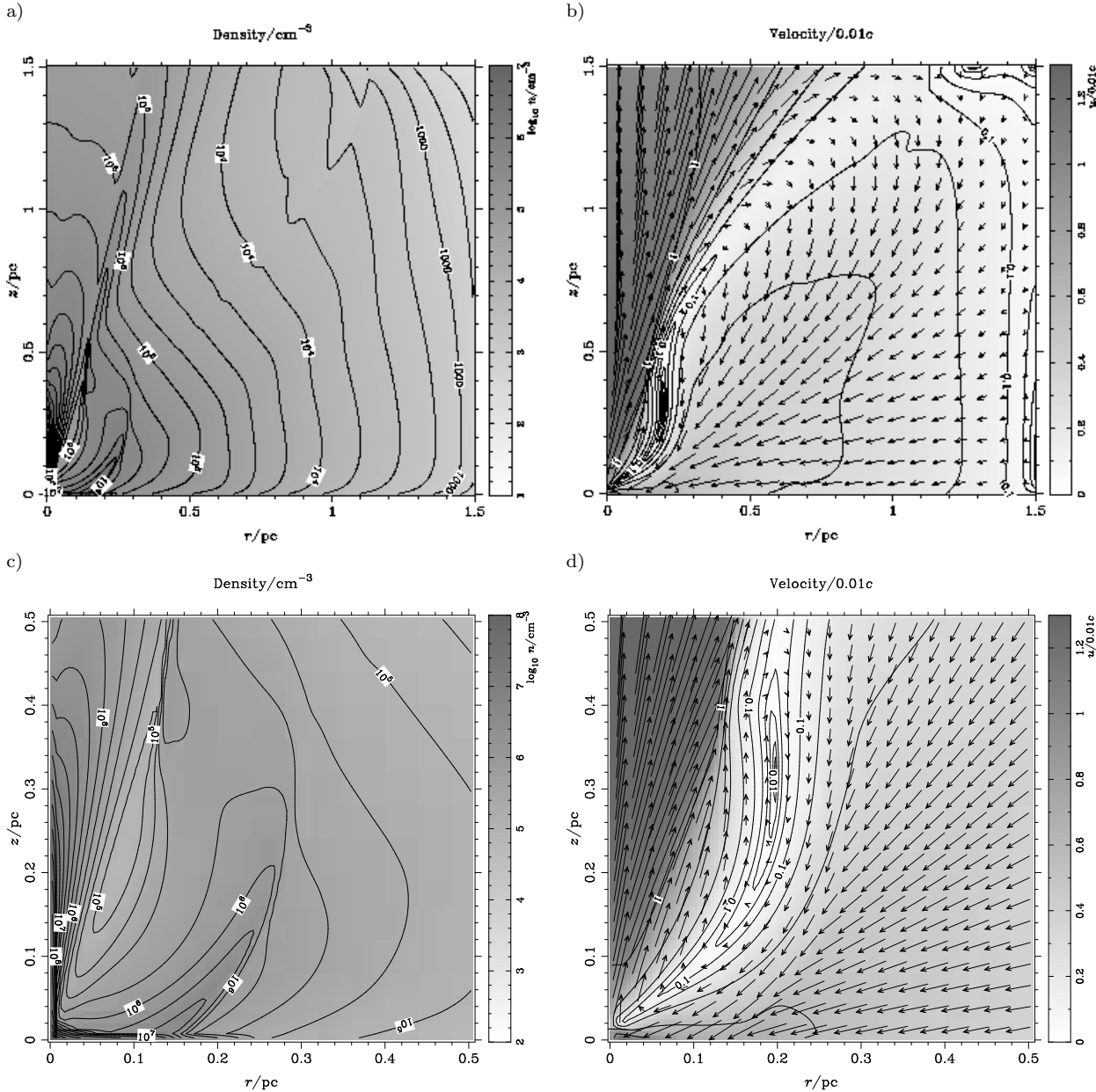


Figure 15. Model $A'_{0.25}$ at 4.6×10^4 yr. The flow here is oscillating, cf. Fig. 23. The panels show a) density (from 182 to $9.6 \times 10^9 \text{ cm}^{-3}$) b) total velocity (greyscale and contours, up to 1.3), c), d) Magnifications of the central region. The vectors are in the flow direction, and have lengths proportional to the velocity, sampled at one vector in every 15×15 cells. The flow is sonic at the $u = 0.1$ contour.

& Krolik, outflows are driven from scales $\gtrsim 1 \text{ pc}$ – the flow within the BELR is purely accretion – and have significantly lower velocities than those we find in our models.

This is also true of the Compton-heated disc winds modelled by Woods et al. (1996). In their very detailed treatment, they found low-level variability in the flows – it is our eventual aim to model the thermal structure of the flow in similar detail, but cooling of gas behind global shocks will make this problem even more computationally taxing than the cases calculated by Woods et al.

We now consider the physical properties of the nISM flows found above. We first discuss the free parameters which are most important in determining the flow structures, and the physical limits of the models. Next, we derived the dy-

namic pressures and ionization state of the flowing gas, especially in Section 7.3, where we also consider the interaction of the nISM with the shocks driven by stars and supernovae. We calculate the overall mass budget of the nucleus in Section 7.5 and the mechanical energy carried in the winds and their effects in Section 7.6. Throughout this section, we highlight the observational consequences of the model.

7.1 Classification Scheme

Comparison of the flow structures shown in the previous section with the sketched structures in Fig. 2 illustrates our suggested classification in terms of the first two parameters. In terms of the physical parameters of the nuclei, the

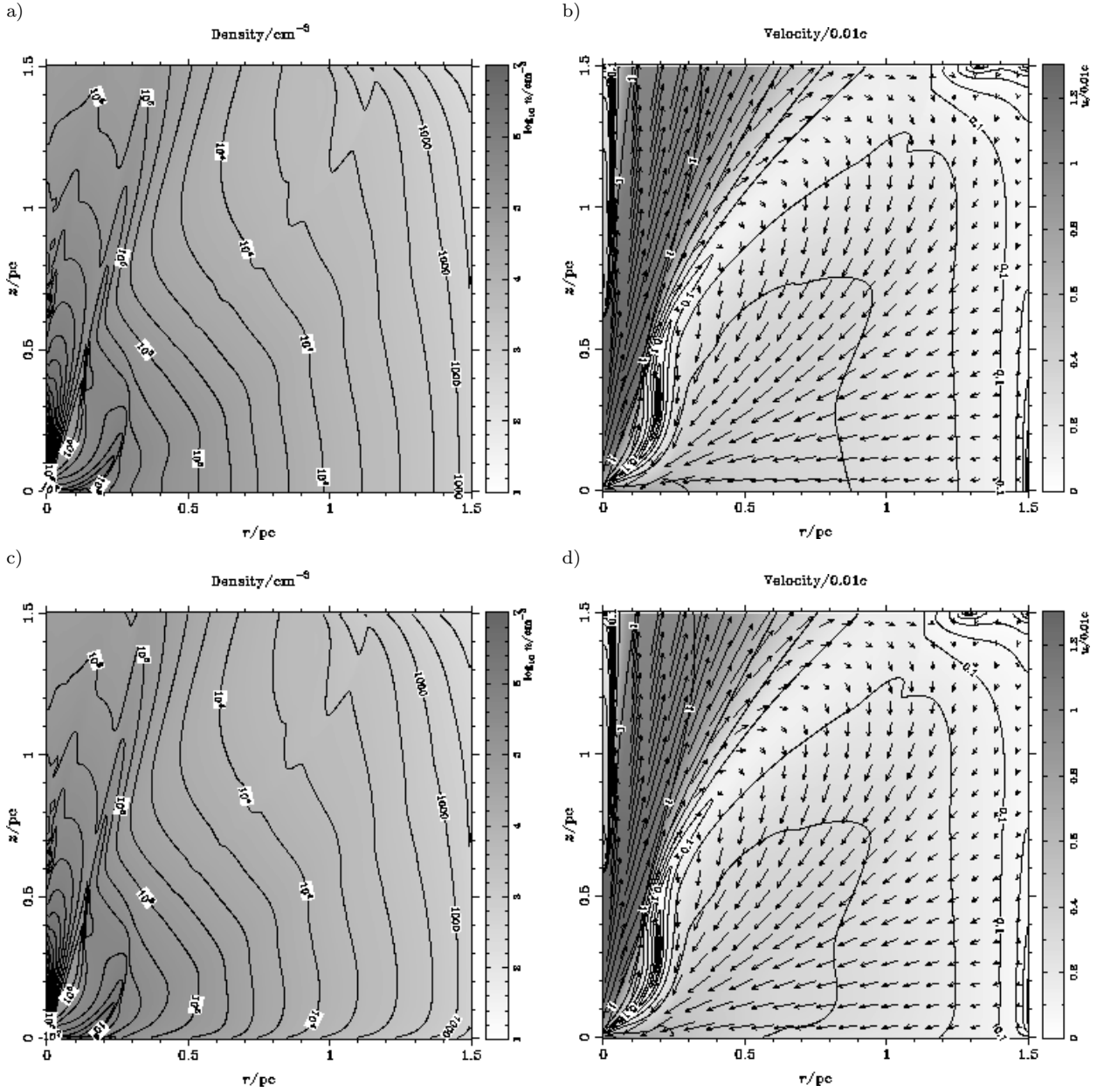


Figure 16. Comparison of (a, b) model $A_{0.005}$ and (c, d) $A'_{0.25}$, both at 6.5×10^3 yr. Notice the similarity of detail in these simulations (away from the disc plane), in particular the dense clump of gas at $z \simeq 0.65$ pc on axis.

Keplerian velocity is $v_K^2 \equiv GM_c/r_c$ and the sound speed is determined by the shape of the AGN continuum. We can estimate the ejection velocity, v_{ej} , by assuming that the central outflow is dominated by gas accelerated in the z direction within the central smoothing region, so

$$\frac{v_{\text{ej}}}{c_s} \simeq \frac{v_z}{c_s} \equiv \left\{ [1 - f_{\text{Edd},0}] \frac{GM_h}{\epsilon c_s^2} \right\}^{1/2}. \quad (21)$$

The comparison between the calculated v_z and the measured v_{ej} is shown in Fig. 3. The comparison is good except for the cases (described in the figure caption) where the approximations made in applying eq. (21) break down.

Where the outward driving from the black hole is large, the flow relaxes to a steady bipolar form: gas falls inwards in the plane of the disc and is then driven away when

reaches the super-Eddington region on-axis, close to the central black hole. When the retarding effects of cluster gravity and mass loading become great enough, the outflow shocks within the stellar cluster. If the sound speed in the hot gas is sufficiently great, a steady recollimating jet structure can be produced. More characteristic, however, is a structure where episodic explosions drive gas from the nucleus in bursts. As the retarding forces increase further, the outflow region becomes more compact and can less often drive mass out from the nucleus, eventually becoming a turbulent core in the flow onto which gas injected in the outer regions of the stellar cluster accretes.

For our approximations to hold, we require that the forces due to the black hole dominate close to it, but that the gravity of the cluster dominates at large radii (this as-

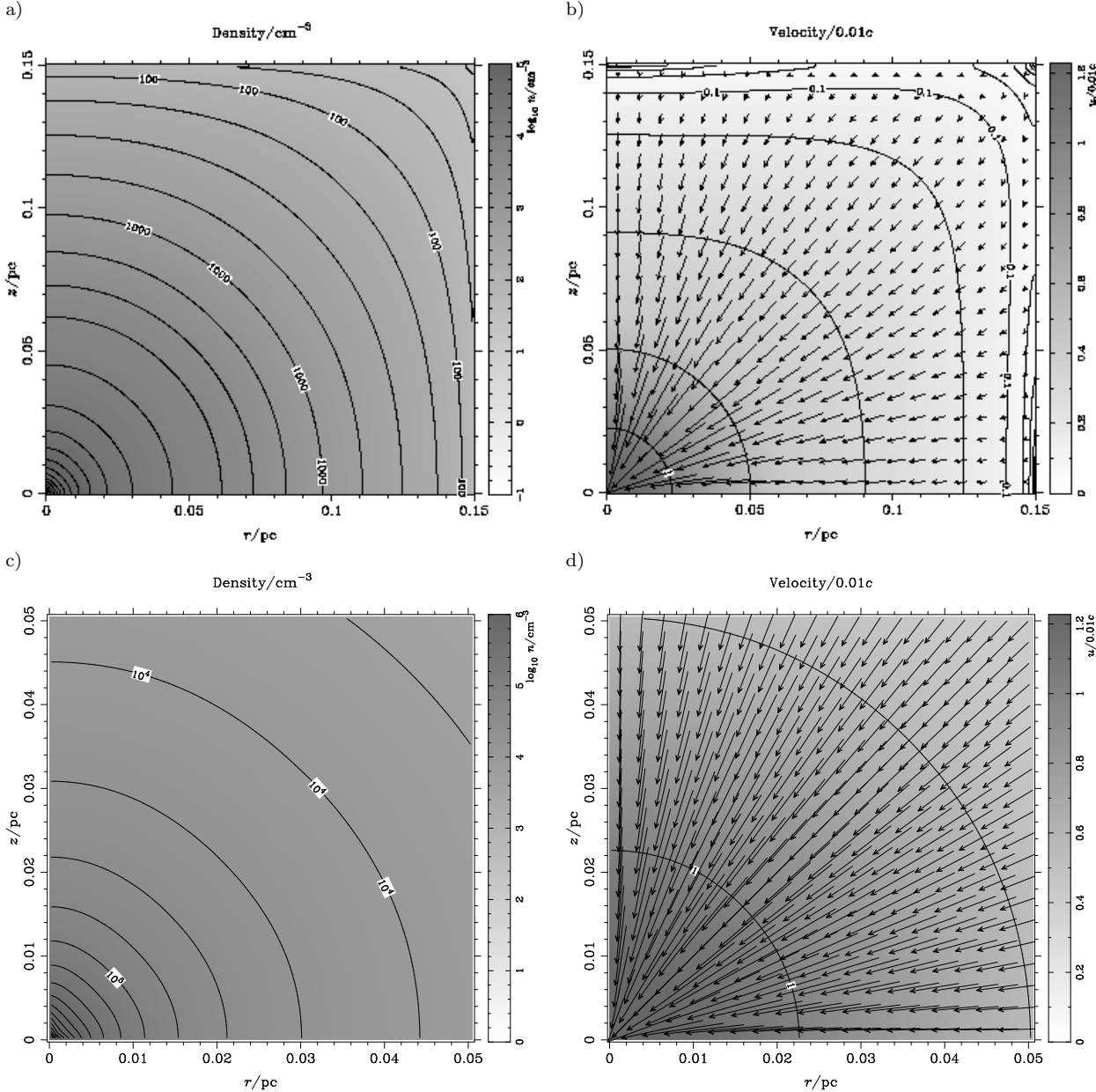


Figure 17. Model Sa at 2.5×10^3 yr. Notice the smaller scale of the grid in this simulation: the flow reaches equilibrium as early as 200 yr as a result of the very short dynamical timescale in this model. The panels show a) density (from 15 to 2×10^8 cm⁻³) b) total velocity (greyscale and contours, up to 1.2), c), d) Magnifications of the central region. The vectors are in the flow direction, and have lengths proportional to the velocity, sampled at one vector in every 15×15 cells in b), every 5×5 in d). Gas flows freely in from the cluster and is accreted at the centre of the grid. The anisotropic radiation, with a mean Eddington ratio of only 0.01, produces no noticeable perturbations on this flow.

sumption is strained in models D and E). Various other parameters come into play; although they are less important, they limit the strict application of our classification scheme. Changes in the opening angle of the outflow (Model H) and the distribution of stars within the cluster will have only a small effect. Accretion of gas from the flow on a dynamical timescale can also serve to weaken the central outflow (models A_i). In all these cases, the morphology of the flows are still broadly within our classification, and analytic estimates of flow velocities and densities are still readily calculable. The net effect of accretion on the flow structures is

to weaken the winds and dampen the variability, although this depends on where the accreted mass is removed from the global flow. Changing this region does not fundamentally alter the structure of the flows until the fraction of the mass accreted exceeds ~ 0.5 . The overall fraction is more important in determining the flow structure than the location of the sink. The structures are basically similar to those found in non-accreting cases, albeit with different black hole parameters (cases in which there is a central wind blowing through a mass-loading cluster will again be similar, so long as this wind does not have a high angular momentum).

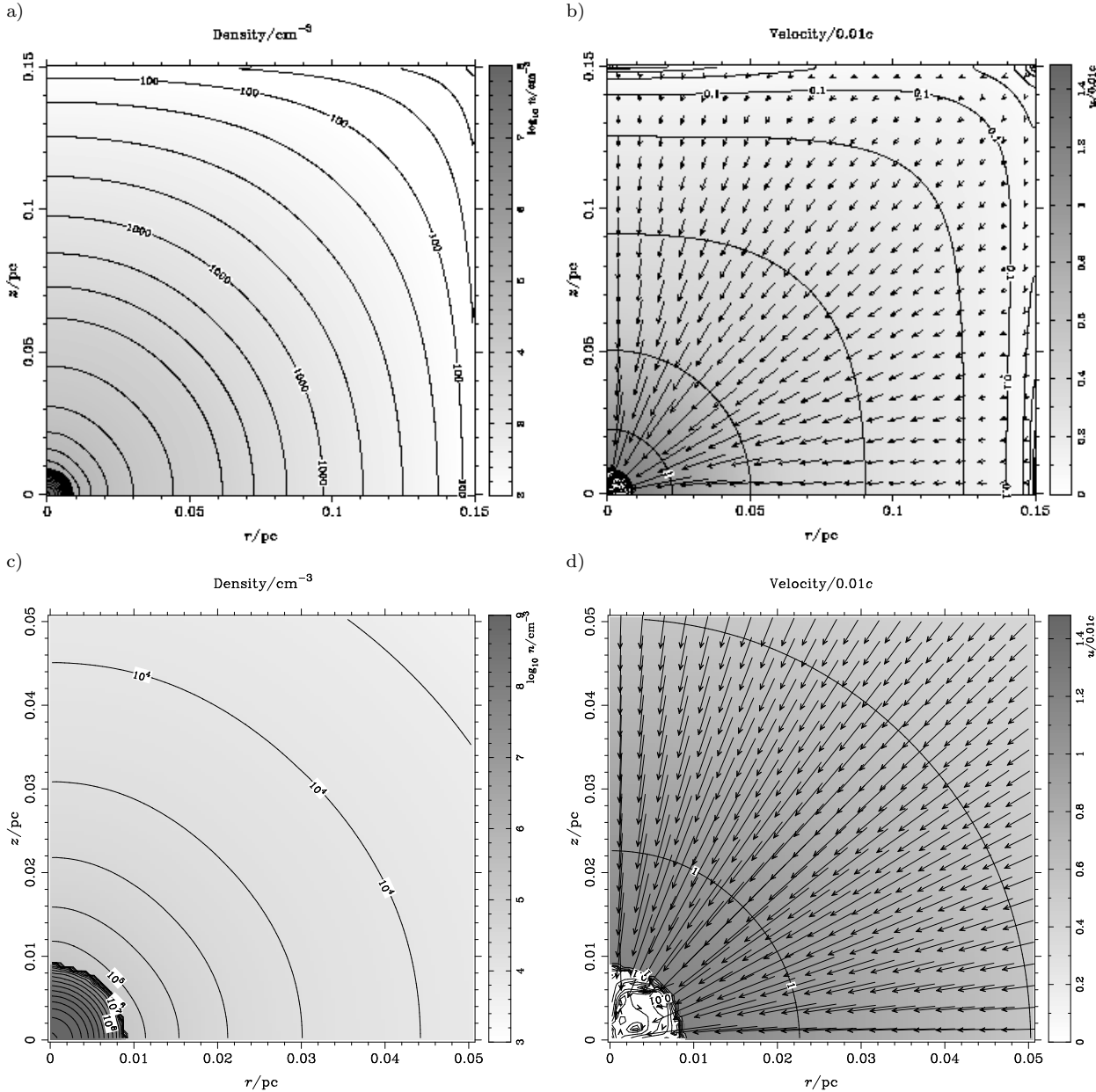


Figure 18. Model Sn at 4.2×10^3 yr. Notice the smaller scale of the grid in this simulation: the flow reaches equilibrium as early as 200 yr as a result of the very short dynamical timescale in this model. The panels show a) density (from 15 to $1 \times 10^1 \text{ cm}^{-3}$) b) total velocity (greyscale and contours, up to 1.5), c), d) Magnifications of the central region. The vectors are in the flow direction, and have lengths proportional to the velocity, sampled at one vector in every 15×15 cells in b), every 5×5 in d). Gas flows freely in from the cluster and is accreted at the centre of the grid. The anisotropic radiation, with a mean Eddington ratio of only 0.01, produces no noticeable perturbations on this flow.

This classification should be supplemented by the number of dynamical times for which mass is retained by the nucleus (which will often relax to a constant value). Most importantly, the gas may not remain in Compton equilibrium, in which case the scalings we have derived will have to be recalibrated in terms of an ‘effective’ Eddington ratio.

7.2 Densities and velocities

The models we have calculated imply a range of local properties (densities, pressures, velocities) for the flows. We now

compare these with simple estimates, based on spherically symmetric flows, similar to those often given in the literature. Conservation of mass in spherical symmetry gives a density for the global flow (on scales of $r = r_{\text{pc}} \text{ pc}$) of

$$n \simeq 4 \times 10^3 \left(\frac{f_{\text{Edd}}}{\mu_{\text{acc}} \eta_{\text{acc},-1}} \right) \frac{M_{\text{h},8}}{r_{\text{pc}}^2 (v_{\text{flow}}/0.01c)} \text{ cm}^{-3} \quad (22)$$

where v is a characteristic flow velocity within the nucleus (by comparison, for the sound speed, $v = 10^{-3} T_7^{1/2} c$ and for the Keplerian velocity, $v \simeq 7 \times 10^{-3} (M_{\text{cl},8}/10r_{\text{pc}})^{1/2} c$).

This estimate of density is in line with the values seen in the accretion flows in, e.g., model A. The flow velocity in the inflow region is about $3 \times 10^{-3}c$, similar to the Keplerian velocity, and the density in this region corresponds to equation (22) to reasonable accuracy. In the axial outflow region, the velocity is about 3 times higher (corresponding to non-Keplerian velocities that are obviously required by the widths of the observed optical emission lines). Here, the density is *higher* than in the inflow region, with a value more than ten times larger than suggested by equation (29). This is because the 60 per cent of the mass input not accreted by the black hole flows out in a cone of half opening angle of only $\sim 15^\circ$, (3.5 per cent of the solid angle) rather than the large fraction assumed in deriving the approximate result.

As the outflows are driven from very close to the central black hole, their velocities are characteristic of these radii. While the highest speeds in the models presented here are $\sim 8700 \text{ km s}^{-1}$, this value can be rescaled by choosing different flow parameters, and might be significantly increased if the effective smoothing length was lower than that assumed. The physical processes which determine the smoothing length are discussed in Section 2.2.6. It is possible that values as small as $\sim 3 \times 10^{15} \text{ cm}$ may be appropriate in some cases, rather than the values of $\sim 1.5 \times 10^{17} \text{ cm}$ we used principally because of computational necessity. Nuclei with very high outflow velocities are, however, likely to have structures similar to our model A, with little retained gas and few global shocks.

If mass is retained by the nucleus for N dynamical times, as for instance in models B and C, the density and pressure [equations (22) and (24)] will be boosted by a factor N , and the ionization parameter [equation (25)] decreased by a similar factor, within the central convective structure. Where this occurs, this will increase the emission from gas in the central plume beyond that, retention occurs.

Therefore, we find that the simple arguments of PD and Perry (1993a) are borne out throughout much of the nucleus. However, they did not anticipate several important effects which we have found boost the gas density in some regions. These are the very regions which may dominate the line emission from these nuclei (as we have seen in the discussion of Fig. 20 above).

7.3 Stagnation pressures, ionization parameters and the multi-component BELR

Both the ionization parameter and the stagnation pressures within the nISM provide checks on the consistency of our models with our assumptions, and are first steps towards assessing the observational consequences of the symbiotic starburst-black hole model for AGN. In this section, we present results for the ionization parameter in the freely flowing nISM, and the ionization parameter and gas pressure at stagnation in the nISM, for two characteristic shock velocities.

The ionization parameter we use is that as defined by (Krolik et al. 1981)

$$\Xi = \frac{F_i}{n_H k_B T_c}, \quad (23)$$

where F_i is the local radiation flux between 1 and 1000 Ryd. This choice of ionization parameter is that which is most

appropriate for discussions of the interplay between hydrodynamics and photoionization equilibrium. Collin-Souffrin (1993) discusses the relationship between the various ionization parameters in common use. We plot Ξ based on the local intensity of radiation, assuming that the ionizing flux is a constant fraction of the total flux.

PD and Perry (1993a) emphasized the importance of shocks in the flows in AGN. A simple estimate of the pressure on cool gas behind a stationary shock, i.e. the stagnation pressure of the flow at v_s , is

$$p_s \simeq 4 \times 10^{11} \left(\frac{f_{\text{Edd}}}{\mu_{\text{acc}} \eta_{\text{acc},-1}} \right) \frac{M_{\text{h},8}}{r_{\text{pc}}^2} \frac{v_s^2}{0.01 c v_{\text{flow}}} \text{ cm}^{-3} \text{ K} \quad (24)$$

and the ionization parameter of shocked gas is

$$\Xi_s \simeq 0.1 \eta_{\text{acc},-1} \mu_{\text{acc}} \frac{c v_{\text{flow}}}{v_s^2}. \quad (25)$$

Hot phase gas will begin to cool when its ionization parameter falls below that at the knee of the equilibrium curve,

$$\Xi_{\text{knee}} \simeq 100 \frac{L_i}{L_{\text{Bol}}} T_{\text{C},7}^{-3/2}, \quad (26)$$

where bremsstrahlung cooling begins to dominate over Comptonization. For a recent composite spectrum, (Ferland 1996) $L_i/L_{\text{Bol}} = 0.45$ and $T_{\text{C},7} = 1.3$.

While this limit is consistent with our choice of constant Compton temperature in the flows we analysed, the anisotropic component of the radiation field may well have a different spectrum to the isotropic one. For example, for the outer regions of the disc plane, it might be more appropriate to consider only the luminosity under the blue bump. In the case of Ferland's continuum, the luminosity in the 1–10³ Ryd wave-band then decreases by a factor more than 5 with a concomitant decrease in Ξ (and, as discussed below, the Compton temperature increases by a factor 2). These gross changes in spectral shape may have considerably more far-reaching effects than simply a change in the ionization parameter. The effects of variations in spectrum and Compton temperature with angle will be discussed in detail in future papers.

If $\Xi_f \lesssim 10$, our assumption of Compton equilibrium for the hot gas will be strained by the increasing influence of bremsstrahlung and atomic cooling. Conservatively, we take $\Xi_f = 10$ as a limit below which cooling is likely to become important.

The pressure in any gas which manages to cool will rarely be less than that in the surrounding free flow, and so the free-flow ionization parameter Ξ_f is an upper limit to that which acts on the cool gas. This free-flow Ξ_f is shown in panel (a) of the graphs in this section.

In panel (b) of the graphs in this section, we show the ionization parameter Ξ_s in gas shocked to stagnation in the rest frame of the nucleus. This ionization parameter characterises the 'average' ionization parameter in shocks which form around local obstacles to the flow, as well as in steady features within the flow.

In reality, most of the obstacles in the flow will be driven by stars and supernovae. The speed of shocks driven by these stars will depend on their orbital velocities, mass ejection velocities and the amount of gas swept up by the shell, as discussed extensively by Perry (1992, 1993a,b, 1999). As an indication of the likely importance of these random veloc-

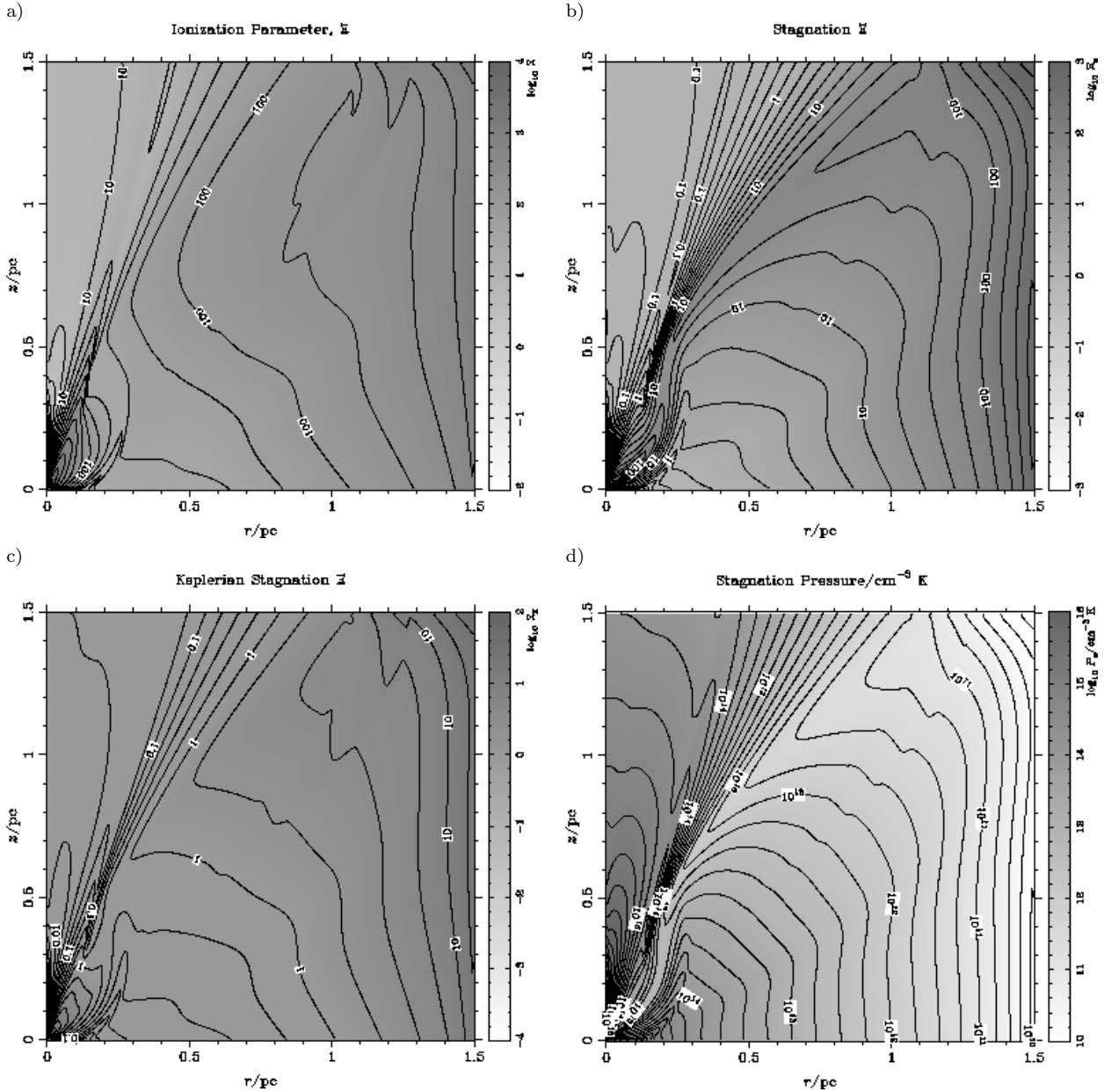


Figure 19. Model A at 2.6×10^4 yr. The panels show a) ionization parameter, Ξ , in the free flow, b) ionization parameter, Ξ_s , at stagnation in the rest frame of the nucleus, c) ‘minimum’ stagnation ionization parameter, Ξ_k , at stagnation against a counter-moving Keplerian obstacle, d) gas pressure, p_s , at stagnation in the rest frame of the nucleus (in $\text{cm}^{-3} \text{ K}$).

ties, we also plot ionization parameters behind shocks of velocity $v_{\text{flow}} + v_K$, where v_K is the local velocity of a circular orbit in the potential of black hole and cluster. This is the maximum shock velocity for a rigid obstacle. Note that in the inner regions of the flow, where the gravity is dominated by the black hole, the Keplerian velocities depend on the absolute mass of the central black hole (and thus the degeneracy between assumed values of $\langle f_{\text{Edd}} \rangle$ and M_h is lifted).

In Fig. 19a we show the ionization parameter, Ξ_f , for Model A. As $\Xi_f > 10$ through most of this region, our assumption that the flow is isothermal at the Compton temperature is self-consistent, except for a very small region close to the origin. There are no direct observational tracers

of gas with this high temperature and ionization parameter. Even iron K-shell absorption, one component of the so-called ‘warm absorbers’, which can be significant in gas with temperatures as high as 10^7 K, will only be important in gas with typical densities $\gtrsim 10^7 \text{ cm}^{-3}$ for the radiation flux assumed here (Mathews & Ferland 1987).

While a wide range of densities and pressures are predicted by these models (cf. empirical evidence for this, Baldwin et al. 1995), broad systematic trends are also expected. For instance, in Model A, there are two regions where the gas shocked to typical stagnation pressures can form line-emitting clouds. In the rest of the flow, post-shock gas has high ionization parameters, and so does not cool sufficiently to radiate emission lines (Fig. 19b). The two line-emitting

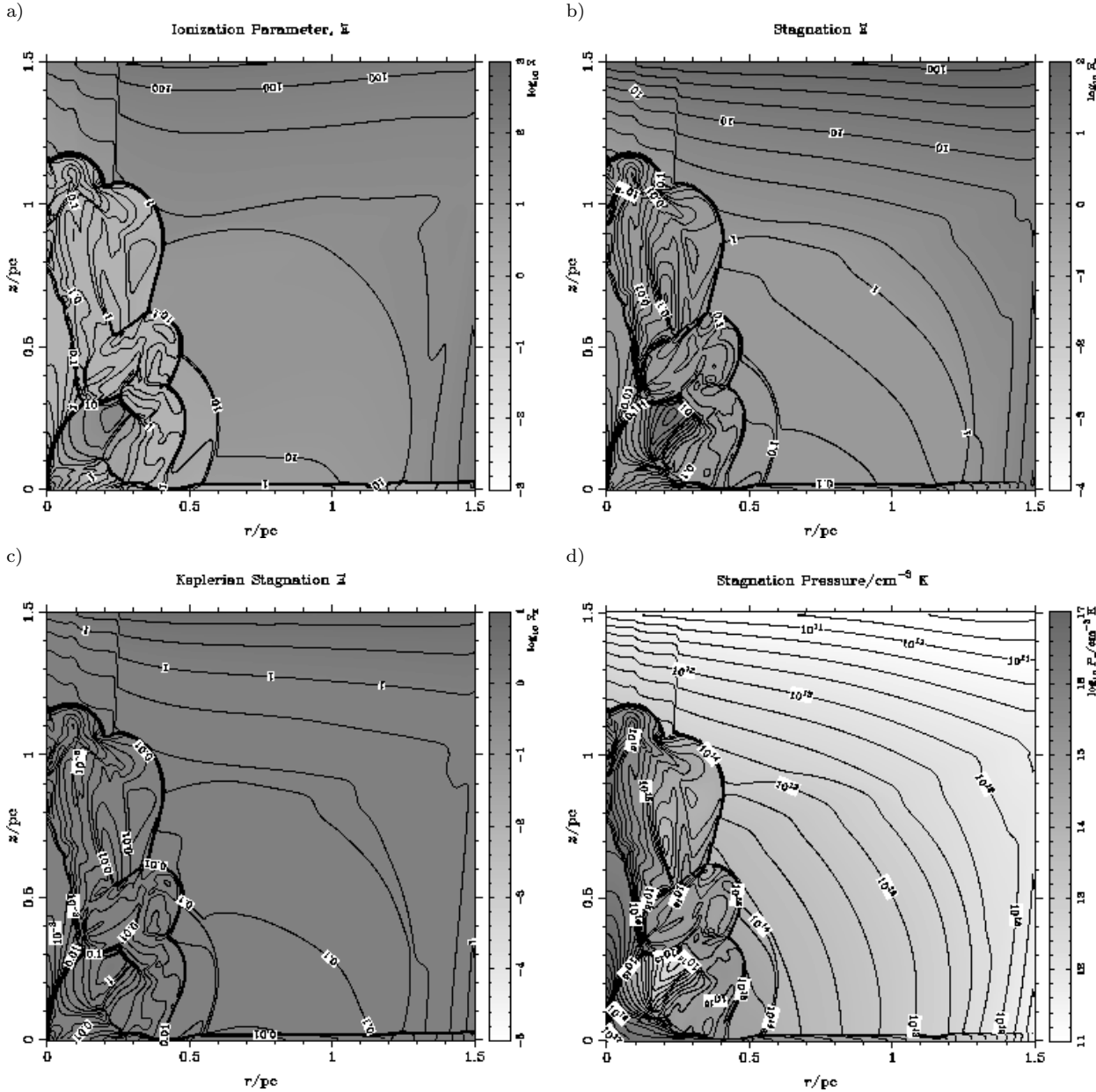


Figure 20. Model B at 6×10^4 yr. The panels show a) ionization parameter, Ξ , in the free flow, b) ionization parameter, Ξ_s , at stagnation in the rest frame of the nucleus, c) ‘minimum’ stagnation ionization parameter, Ξ_k , d) gas pressure, p_s , at stagnation in the rest frame of the nucleus (in $\text{cm}^{-3} \text{ K}$).

regions are near the outflow cone, and just above the disc. The stagnation ionization parameter is $\lesssim 0.1$ through most of the conical outflow around the axis. The pressures here are high ($\gtrsim 10^{14} \text{ cm}^{-3} \text{ K}$, Fig. 19d). Above the accretion disc, in the other low ionization parameter region, inflowing gas shocks to a rather smaller pressure, $\sim 10^{13} \text{ cm}^{-3} \text{ K}$. The relative contributions of these two regions to the observed broad emission lines will be weighted by their relative volumes of rotation about the z -axis. Many physical effects other than the overall pressure and ionization parameter must be included in determining the volume emissivity of the cool gas from hot phase properties (cf. PD, and below). However, the obvious distinction between the properties of gas in the two

regions means that, broadly-defined, two ‘components’ will describe these two, dynamically separate flows.

The fastest shocks, where Keplerian velocities add to the flow velocity, can cool gas throughout the entire cluster core as well as in a broad cone outwards along the flow axis, if the gas can be maintained at the high pressure at the head of the shock for at least a cooling time (Fig. 19c). In future papers (Albertsson & Perry 1999), we will predict the detailed line profiles and variability signatures expected as a result of the combination of all these effects.

The flow in Model B (Fig. 20a) is too dense in most of the central ‘plume’ to be maintained in isothermal equilibrium by Compton heating and cooling. Except for a small conical area about the central black hole, all the gas with

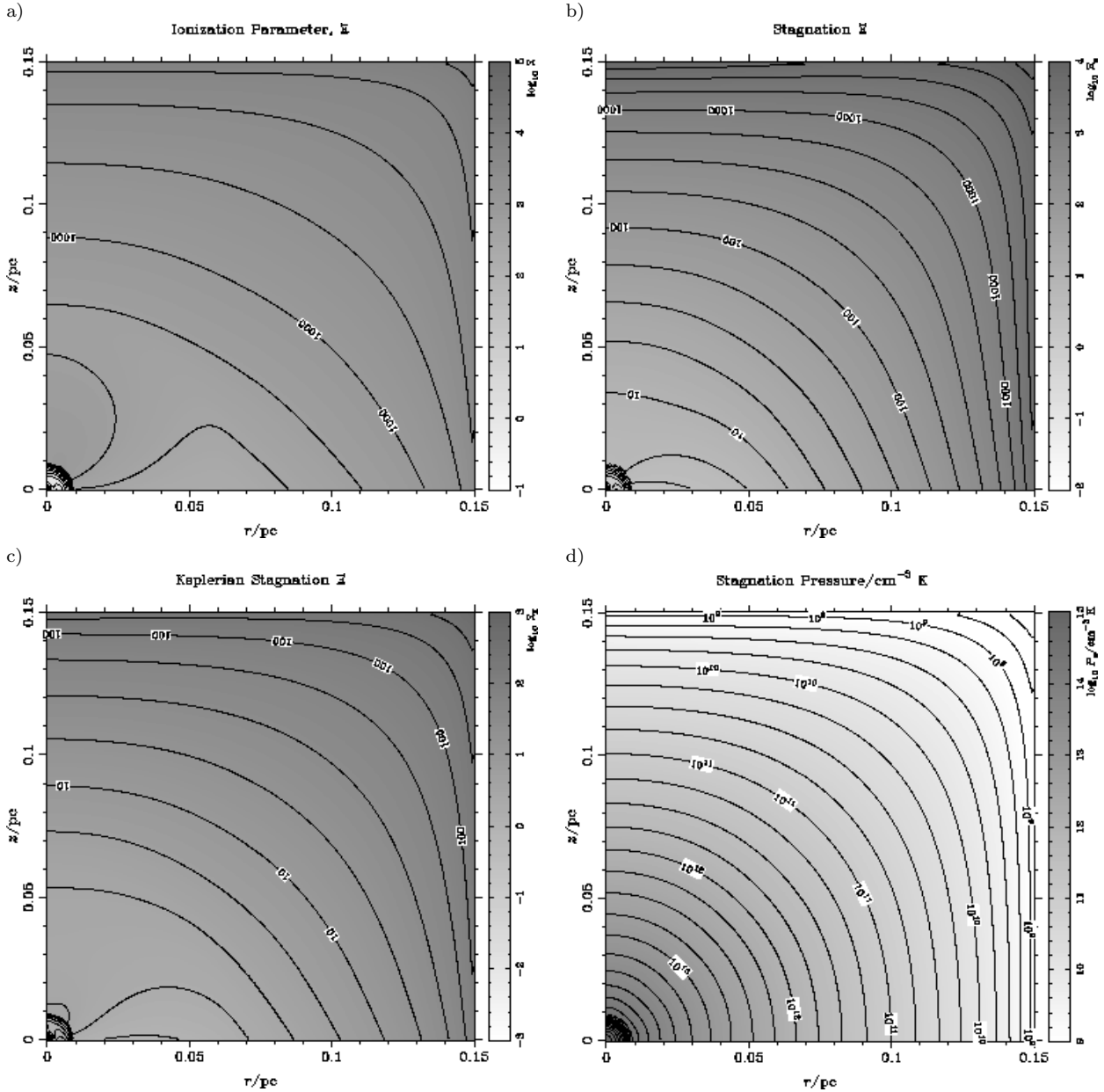


Figure 21. Model Sn at 4.2×10^3 yr. The panels of this plot show a) ionization parameter, Ξ , in the free flow, b) ionization parameter, Ξ_s , at stagnation in the rest frame of the nucleus, c) ‘maximum’ stagnation ionization parameter, Ξ_k , d) gas pressure, p_s , at stagnation in the rest frame of the nucleus (in $\text{cm}^{-3} \text{ K}$). The anisotropic form of the ionization parameter plots results from the variation of nuclear luminosity and spectrum with angle to the nucleus.

$r \lesssim 0.5 \text{ pc}$ and $z \lesssim 1 \text{ pc}$ has an ionization parameter less than unity. This low free-flow ionization parameter puts considerable strains on our assumption of Compton equilibrium. Net heating of the gas in smaller mass-loading shocks may be able to offset some of the bremsstrahlung cooling. In addition, the additional cooling will have the side-effect of increasing the opacity of the gas, and hence the radiative forces on the flow (cf. Section 7.4). As these radiative forces increase, the topology will gradually become more like Model A. This self-regulation will enhance the frequency with which flow structures intermediate between Models A and B are found. The particularly high pressures found in the accretion disc plane will encourage cooling, perhaps lead-

ing to the addition of mass from the free flow to the outer accretion disc, as in Model A'0.25.

As might be expected, the distribution of stagnation ionization parameters, in Model B (Fig. 20b) is rather smoother than the distribution of free-flow ionization parameters discussed above (since gas at rest has the stagnation pressure by definition, slow moving shocks have a less marked effect on the ionization parameter). The stagnation ionization parameter is, however, less than 1 throughout the central 1 pc sphere of the nucleus. In the near-radial inflow region outside the central plume, gas pressures are $\gtrsim 10^{13} \text{ cm}^{-3} \text{ K}$.

The stagnation ionization parameters are far lower than

this in the central plume itself, with pressures reaching more than $10^{16} \text{ cm}^{-3} \text{ K}$. Shocks in the plume will cool fast, and the cool gas will radiate strongly, since this is the region in which the radiation from the central accretion disc is at its strongest.

In Fig. 21, we show the ionization parameters derived from the low Eddington-ratio model with no accretion, Sn (cf. Fig. 18). The free-flow ionization parameter, Ξ_f (Fig. 21a), shows that the nISM is always hot and diffuse. The stagnation ionization parameter, Ξ_s (Fig. 21b), is sufficiently small to allow cooling in only a very small region in the plane of the accretion disc where the radiation field is weak. This region is expanded to fill most of the cluster core when the influence of Keplerian velocities is accounted for (Fig. 21c) – however, the cooling length behind such shocks would be a substantial fraction of the size of these nuclei.

Behind shocks in this region the cooling will be very rapid (Innes & Perry 1999), and consequently the size of the BELR will be close to that derived from variability studies (Perry 1994).

We conclude that the BELR in many AGN must be highly complex, anisotropic, unsteady and irregular. Physical effects not included in the current treatment will modify our results, but the general form of the flows will remain similar to those presented here. Nevertheless, Figs. 19 and 20 give a general impression that the structures should be able to be broken down into a few components, with varying mean properties. We will undertake the detailed modelling required to confirm this in future papers (Albertsson & Perry 1999).

7.4 Column density and opacity

In some of our models, in which mass is retained for several dynamical times, the column depth of the nISM reaches values around 10^{24} cm^{-2} . This will have potentially observable consequences. At these column densities, the nucleus will be getting close to a Thomson optical depth of unity. Electron scattering will weaken the continuum observed along the densest lines of sight to the nucleus, smooth out continuum variability and lead to polarisation of the scattered component. The emission lines will also develop a thermally broadened component, although the optical depth to line-emitting clouds distributed in the nISM will be smaller than that to the central continuum source.

X-ray absorption by highly ionized oxygen and iron, at energies of 0.3–10 keV, is seen in many low luminosity AGN (Nandra & Pounds 1994; Reynolds & Fabian 1995; Krolik & Kriss 1995). The location of the absorbing gas is uncertain: some of the absorption may be from the gas which is observed in Seyfert 2 galaxies to scatter the obscured central radiation source, while some may also be far closer to the nucleus. This ‘warm absorption’ is currently the best diagnostic of gas which is more widely distributed than the locally confined broad emission line clouds.

The observational results are, in general, given in terms of the column density and ionization parameter required for a uniform intervening slab of solar-abundance gas in thermal equilibrium to generate the absorption features seen. Typical column densities are 10^{22} – 10^{24} cm^{-2} and temperatures 10^5 – 10^6 K . Reynolds & Fabian (1995), for instance, base their discussion of the observations of a particular Seyfert on

a column density of 10^{22} cm^{-3} and $L_i/nr^2 = 30 \text{ erg cm s}^{-1}$, where L_i is the total ionizing luminosity and n is the electron density. These values imply that the gas temperature is 10^5 K – they find the gas resides in a toe-hold of thermal stability between the usual cool and hot equilibria. The poor spectral resolution of (all but the most recent) X-ray observations is a valid reason for using this approach to get the most out of the available data. Krolik & Kriss (1995) emphasise that the material observed may well be out of thermal equilibrium, cooled by adiabatic expansion (although it is likely to be in ionization equilibrium). This is an even more important constraint where the gas is being evaporated from a local evaporation centre rather than expanding as part of a global flow.

Until our models are extended to explicitly include the thermal balance of the gas, we cannot model the warm absorber in detail. It is, however, clear that a number of potential locations for the warm absorber arise naturally in these models. The global flow may dense enough that it has begun to cool in some regions, or may be cooled at large distances from the nucleus by adiabatic expansion (Krolik & Kriss 1995). In addition, in the shocks which create the broad-line emitting gas must cool through this temperature range; subsequently the gas will evaporate from the cooled clouds and rejoin the flow. For a plane radiative shock, the column between 10^5 K and 10^6 K is roughly equal to the mass flux multiplied by the cooling time, which is $\lesssim 10^{19} \text{ cm}^{-2}$ for post-shock pressure of $10^{14} \text{ cm}^{-3} \text{ K}$. The Compton heating time is $\sim 10^5$ times longer than this cooling time, and may be lengthened further by adiabatic cooling and residual atomic cooling. However, the evaporation will only occur once the gas has reached a region with substantially lower pressure than behind the radiative shock and further divergence of streamlines will occur while the gas is heating (PD), both of which effects may act to decrease the column of gas available to generate absorption. The heating gas may be a significant component of the absorption (Reynolds & Fabian 1995), but this needs to be studied in greater detail.

7.4.1 Cooling and the effective Eddington ratio

Cooling leads to significantly enhanced opacity and hence radiative forces on nISM gas: in consequence, the densities will be reduced, so an equilibrium may be found with a substantial mass loss rate even where the Eddington ratio is less than unity. The overall radiation force can be expressed as an angle-averaged *effective* Eddington ratio,

$$\langle f_{\text{Edd}}^{\text{Effective}} \rangle = \frac{\bar{\sigma}}{\sigma_T} \langle f_{\text{Edd}} \rangle \simeq 0.4 \frac{\eta_{\text{acc}} \mu_{\text{acc}}}{0.1} \frac{\bar{\sigma}}{\sigma_T} Q_{-8} \frac{M_{\text{cl}}}{M_{\text{h}}}, \quad (27)$$

where η_{acc} is the efficiency with which the central accretion disc radiates the rest-mass energy delivered to it by the global flow; μ_{acc} is the fraction of the mass input from the cluster delivered to this central region, and $\bar{\sigma}$ is the mean effective cross-section for gas close to the black hole. Of all the various uncertainties implicit in the terms of the above equation, the determination of the effective cross-section is perhaps the greatest (cf. Turner et al. 1993).

In most of the models presented here, we assume that the overall Eddington ratio is close to one. Various independent observations suggest that typically $10^{-3} < f_{\text{Edd}} < 1$, given specific model assumptions (see Appendix 2.2.4). As

f_{Edd} approaches unity, the structure of the accretion disc will become bloated by radiation pressure, although this bloating is reduced if the luminosity of the accretion disc is dominated by reprocessing.

We have assumed $\bar{\sigma} \equiv \sigma_T$ (and thus $f_{\text{Edd}}^* \equiv f_{\text{Edd}}$, the classical Eddington ratio) in the models presented here. However, if the density of the gas is high enough, some fraction of the gas may be able to cool, enhancing the radiative driving. For optically thin gas at equilibrium in the BELR (modelled by Cloudy Ferland 1996) the force multiplier $\bar{\sigma}/\sigma_T$ increases to roughly 2 at 10^6 K, 40 at 10^5 K and to 10^4 and beyond when the gas has cooled fully (see also Arav, Li & Begelman 1994). It is reasonable to take $g = 7 \times 10^{14} \rho$ when the gas is cooler than $\sim 5 \times 10^4$ K (cf. Röser 1979; Dyson, Falte & Perry 1981), although this force is dominated by resonance line scattering and will weaken by a factor of a few if the lines are optically thick. Hence even in Seyfert galaxies, where f_{Edd} (determined by electron scattering) may be far smaller than unity, a dynamical feedback may lead to flows of very similar forms to those presented in here.

7.5 Mass budgets: winds and accretion efficiency

Here, we discuss the mass budgets found for the models we have calculated: how much of the mass lost by the stellar cluster – and its associated heavy elements – remains in the nISM, how much is delivered to the accretion disc, and how much is transferred to the wider galaxy. Numerical values for the equilibrium mass processing rates have been given in Table 6.

The mass processing rates of models A and B are shown in Fig. 22 (we do not show Model C, since almost no mass is lost from this nucleus over our integration period). For Model A, the mass loss rate reaches an equilibrium after roughly the sound crossing time of the nucleus. Model B produces a series of explosive mass loss episodes, continuing for times as long as we have simulated. The characteristic timescale of these explosions, typically 10^3 yr, is comparable to the gravitational timescale, $1.6 \times 10^3 r_{\text{c,pc}}^{3/2} M_8^{-1/2}$ yr.

We plot the variation of total mass within the grid of Model B in Fig. 24. This is the integral of the variation shown in Fig. 22b. As we have already described, the flow is highly variable, alternating between times when the input mass is almost entirely retained (the steepest upward slopes in Fig. 24), and epochs of rapid mass loss. In particular, this figure emphasises the long-term chaotic behaviour of the flow structure we have simulated. It also shows how close Model B is to the border between steady-outflow and chaotic flow. During the extended minimum around 2×10^5 yr, the structure and density of the flow is very similar to that shown, for Model H, in Fig. 12. Indeed, we would hope this were so, since the fundamental parameters for Models B and H are identical (cf. Fig. 2) – they differ only in the opening angle of the central outflow cone.

The fraction of stellar mass loss delivered by the flow to the accretion disc depends critically both on the structure of the flow and on details of the processes by which mass is added to the accretion disc. A primary aim of this paper is to address the first of these issues. Therefore, we treat the second by three extreme assumptions – no mass addition to

the disc, or addition only in an inner or outer region of its surface.

The fractional rate of accretion, μ_{acc} , was assumed to be zero in models A, B and C. In models A_{0.005} and A'_{0.25} it was found to be around 40 per cent, while for model A_{0.25} almost all the mass input is accreted. The area of the disc over which accretion took place in models A_{0.005} and A'_{0.25} was chosen so that the accretion rate and wind flux were nearly in balance. In general, μ_{acc} tends to be close either to zero or to unity: we leave the precise elaboration of this dependence as a function of physical parameters for a future paper.

We show the mass fluxes for models A_{0.005}, A_{0.25} and A'_{0.25} in Fig. 23. Fig. 23a shows how the accretion region in model A_{0.005}, which is relatively small, diverts a fraction of the mass which would otherwise have been driven out in the wind, perhaps slightly extending the length of the variable period compared to model A. In contrast, if accretion occurs over a large area (Model A_{0.25}, Fig. 23b), the outgoing wind is suppressed. The solution soon relaxes to a near-equilibrium between mass input and accretion, modulated at a 10 per cent level by the instability of the termination shock and accretion. The evolution of model A'_{0.25} (Fig. 23c), in which accretion takes place in the outermost regions of the disc, is strikingly similar to that of Model A_{0.005}. This can be understood, as already discussed, on the basis of morphological arguments.

To supply the luminosity of a QSO, $L \simeq 1.3 \times 10^{46} f_{\text{Edd}} M_{\text{h},8} \text{ erg s}^{-1}$ requires accretion at a rate

$$\dot{M} \simeq 2.3 \left(\frac{f_{\text{Edd}}}{\eta_{\text{acc},-1}} \right) M_{\text{h},8} \text{ M}_\odot \text{ yr}^{-1}, \quad (28)$$

where $\eta_{\text{acc}} = 0.1 \eta_{\text{acc},-1}$ is the accretion efficiency of the black hole. The accretion rate is given, over the long term, as a fraction of the mass-loading rate from the stellar cluster by μ_{acc} , which is determined by the global hydrodynamics of the nucleus. The fraction of input mass which must be accreted is given by

$$\mu_{\text{acc}} \simeq 0.23 \left(\frac{f_{\text{Edd}}}{\eta_{\text{acc},-1} Q_{-8}} \right) \frac{10 M_{\text{h}}}{M_{\text{cl}}}. \quad (29)$$

Perry (1993a) argues that $\mu_{\text{acc}} \simeq 0.5$. The accurate calculation of this fraction is one eventual aim of this work: some values of μ_{acc} are given in Table 6. To the accuracy of the present treatment, models A_{0.005} and A'_{0.25} are self-consistent, and closest to the case considered by PD and Perry (1993a).

In a Seyfert nucleus residing in a rejuvenated QSO, the ratio of M_{h} to M_{cl} may be substantially larger than 1:10. From equation (29), a self-consistent model (with $\eta_{\text{acc}} < 1$) must be significantly below the Eddington limit unless gas is provided to the black hole from non-stellar sources or the stellar lifetime is very short.

From Table 6, we see that rates for these models range between 3.2 and $8.6 \text{ M}_\odot \text{ yr}^{-1}$. Comparing these with the accretion rate required to fuel the central luminosity, $4.6 \eta_{\text{acc},-1} \text{ M}_\odot \text{ yr}^{-1}$, we see that these models are reasonably self-consistent, i.e. the accretion rate is sufficient to power the central luminosity for a reasonable assumed radiative efficiency. If we impose the condition that the flow is self-consistent over the short-term, then the flow may to relax to one of these solutions, *however sensitive* the dependence of

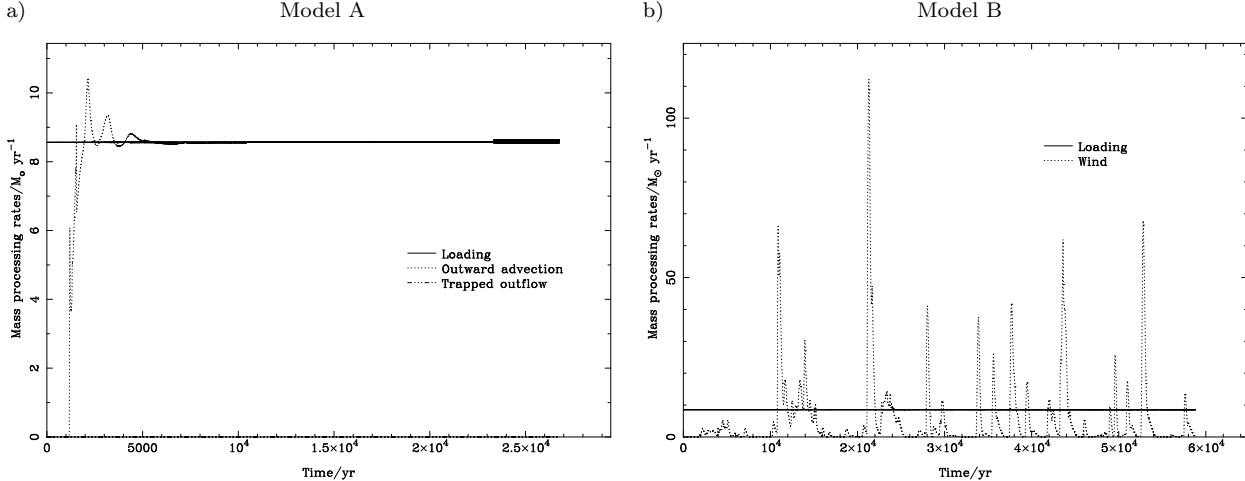


Figure 22. Mass processing rates of models a) A, b) B. Model A soon reaches a steady equilibrium between mass input and mass outflow. In Model B, mass is lost episodically from the nucleus. While as much as 60 per cent of this loss does not have escape velocity, we argue in the text that the effect of assuming this mass is lost to the grid will be small. Model C has no appreciable mass loss in 10⁶ yr.

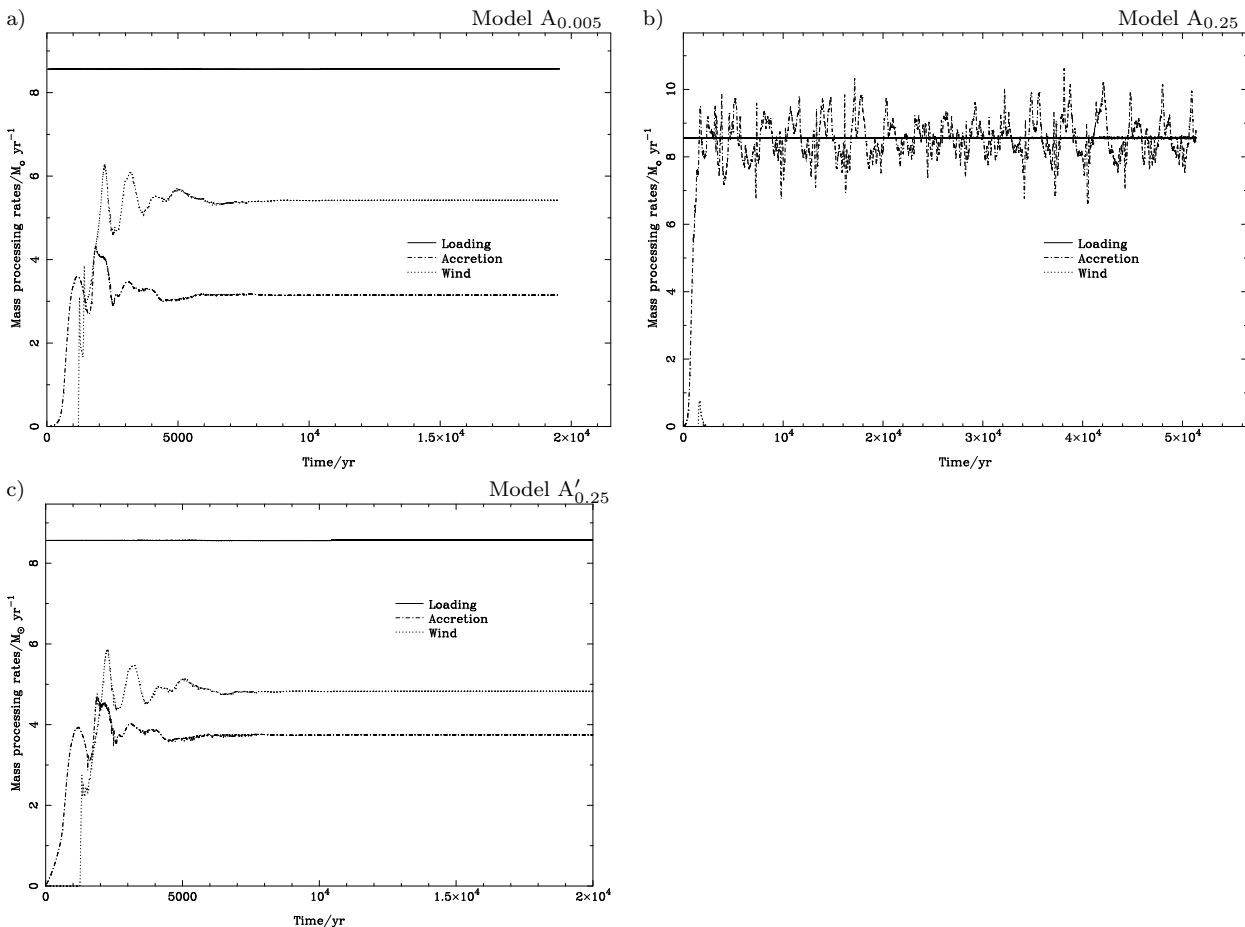


Figure 23. Mass processing rates of models a) A_{0.005}, b) A_{0.25}, c) A'_{0.25}. Models A_{0.005} and A'_{0.25} reach a steady equilibrium solution, very similar to Model A but with a fraction of the mass input diverted into accretion. Model A_{0.25}, on the other hand, has a global structure rather similar to Model C. Only a small fraction of the gas escapes accretion, and the central wind is consequently too weak to drive out through the cluster core. The mass input and accretion rates soon reach equilibrium, modulated by near-periodic instability of the accretion/wind interface.

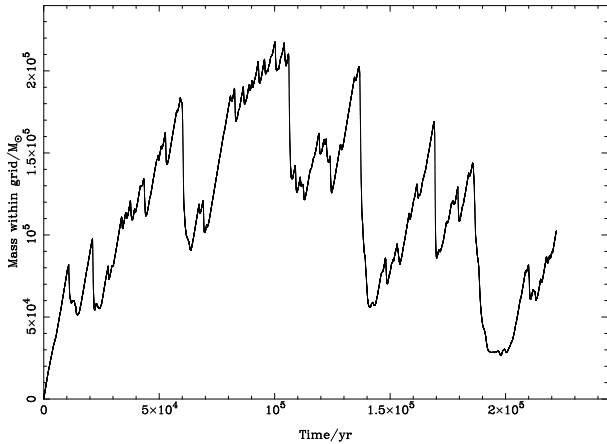


Figure 24. Mass within the grid for Model B, cf. Fig. 6.

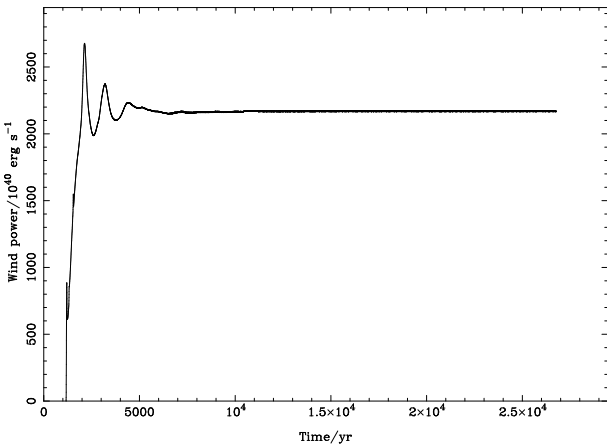


Figure 25. Wind power in Model A.

μ_{acc} on flow parameters. Note, however, that delays in the conversion between mass accretion onto the disc and the output of radiation are likely to imply that the equilibrium is, in fact, unstable.

If all relevant dimensionless quantities, including the Eddington ratio, are kept constant (cf. Section 3.2), the ratio L/\dot{M} varies as $1/\phi$ and is independent of the length and timescales chosen (because $L/\dot{M} \propto M_h/\phi M_{\text{cl}}$; by contrast, if $L \propto \lambda^2$ and $\lambda = \tau$, then $L/\dot{M} \propto \tau/\phi$, and any solution with finite accretion can be made self-consistent). Note, however, that delays and instabilities in the processing of gas through the accretion disc may mean that, on the short timescales, not all AGN are strictly self-consistent, in the formal sense defined above.

7.6 Wind powers

The average wind powers found for ‘mature’ flows in the various models presented here are included in Table 6. As can be seen by comparing Fig. 25 to Fig. 22a, the time variation in the power of the wind out from the nucleus was very similar to the variation in mass loss rate. By contrast, in model B, only a very little of the mass lost to the grid has escape velocity, so the value quoted in Table 6 is very uncertain.

The highest efficiency with which the central luminosity

was converted into outflow power in the models presented here was in Model A, where the efficiency was $L_{\text{wind}}/L_{\text{Bol}} \simeq 8 \times 10^{-4}$. Mass loss rates from the nucleus to the surrounding galaxy vary from effectively nil to $8.6 M_{\odot} \text{ yr}^{-1}$ (or, rather, that the entire of the mass input to the cluster is lost). Rather lower values are typical in most flows. By scaling the models, as discussed in Section 3.2, we see that the wind efficiency varies as $\phi \lambda^2/t^2$: it would seem to be able to be increased to an arbitrary degree. However, the total efficiency obtainable is limited in reality by the Thomson optical depth of the nISM (which limits the column density, $\propto \phi \lambda/t$) and by the onset of relativistic effects as dynamical velocities ($\propto \lambda/t$) approach c . The values of the parameters for Model A were also chosen to reflect those likely in real nuclei, except that the driving radius of the flow (i.e. the smoothing region) is larger than is likely to obtain in real AGN, so values rather greater than $L_{\text{wind}}/L_{\text{Bol}} \sim 10^{-3}$ may be possible.

The effect on the galaxy of the winds from a symbiotic nucleus will be difficult to distinguish from those of winds driven by larger-scale galactic starbursts or of relativistic jets driven from smaller scales (e.g. Veilleux et al. 1994; Colbert et al. 1996). Heckman et al. (1990) observed starburst superwinds with wind powers up to several $10^{43} \text{ erg s}^{-1}$, with overall $L_{\text{wind}}/L_{\text{Bol}} \sim 10^{-2}$ and wind velocities from a few 100 km s^{-1} to above 1000 km s^{-1} (although again the winds in some of their sample may be driven, in part, by AGN). Whether the source is a starburst or an AGN may be distinguished by whether the starburst is strong enough to drive the wind, and to produce the observed gas velocities, or whether the morphology of the wind bubble suggests an unresolved, dynamically distinct source (e.g., if it is misaligned with galactic structure). Ill-collimated winds may be distinguished from jets by the length-to-breadth ratios of the structures which result, and by evidence for relativistic motions (e.g. synchrotron emission or superluminal motion).

A wind with the strength we find can have a major effect on the ISM of the galaxy and on its surroundings. As the wind-blown bubble moves out, it will generate dense shells of gas which may be important for narrow line emission; eventually it may evacuate the ISM completely (Dyson, Falte & Perry 1981; Falte, Perry & Dyson 1981; Taylor, Dyson & Axon 1992; Smith, Kennel & Coroniti 1993; Steffen et al. 1997). As it blows outwards, it will be an important source of energy and processed material to the intergalactic medium (Voit 1994; Silk & Perry 1999).

8 CONCLUSIONS

The central thesis of this paper is that stars are of fundamental importance in the nuclei of active galaxies. The symbiosis between a compact nuclear starburst stellar cluster and a massive black hole can self-consistently explain the properties of active nuclei.

These two simple ingredients – a spherically symmetric starburst stellar cluster and an accreting black hole – conspire symbiotically to produce flows of immense variety and complexity. Where the gravity and radiation field of black hole and accretion disc dominate at the very centre of the nucleus, a bipolar circulation is found. Outflows along the axis perpendicular to the accretion disc coexist with inflow

in a broad flattened structure above the disc. The interaction between this central flow and that in the region where the gravity of the stellar cluster dominates the dynamics results in highly complex nuclear wide flows. These resulting parsec-scaled nISM bipolar flows range from episodic, explosive, percolating structures to well-collimated, narrow, hypersonic hydrodynamic jets. The jets arise when the flow through most of the core is quasi-hydrostatic, while episodic ‘bubbles’ occur when the Keplerian velocity of the cluster is substantially supersonic. It is important to note that these dramatic structures arise as a result of pure hydrodynamics in a relatively simple system; they do not require the intervention of radio-related nuclear phenomena. Our results dramatically illustrate why broad emission line studies have consistently failed to identify any simple, global flow patterns. The real flow structures in AGN are *inevitably* more complex.

Our simulations confirm the overall flow properties of derived by PD and Perry (1993a). We also find details that their treatment overlooked. The gravitational attraction of the stellar cluster can lead to gas being retained within the nucleus for many dynamical times, with the line emission likely to be dominated by gas in a central plume which is retained by the gravity of the cluster.

We propose (see Section 3.4.2) a classification of the flow structures in terms of dimensionless dynamical parameters: the velocity dispersion of the cluster and the outflow velocity from close to the black hole, both expressed as fractions of the sound speed in the nISM. These relate to the gravitational and thermal energies in the nISM. This classification scheme, which is analogous to the Hertzsprung-Russell diagram for stars, will be broadened by the various secondary effects which depend on the dominant parameters. But the morphology of the flows are likely to remain similar and analytic estimates of flow velocities and densities are still readily calculable.

We have discussed other observational diagnostics of these flows. The mass-losing stellar cluster acts as an optically-thin fuel reservoir which chemically enriches the nISM. When we consider the properties we expect in the broad emission line region (BELR) we find that the nISM itself has a multi-component structure. This fact, combined with the close relationship between the accretion disc and the kinematics of the global wind helps explain the observed multi-component structure of the line spectra and the observed correlations between low- and high-ionization broad emission lines. The varied kinematics of the flows seems to explain the contradictory evidence that has been found for inflow, outflow, chaotic or rotating flows by observers. The winds driven from the nuclei will also affect the surrounding galaxy and the IGM.

Our study clearly shows that active galactic nuclei will only be fully understood once the symbiotic relationships between the black hole, the nuclear starburst stellar cluster, and the wider galaxy are considered. Our conceptually simple *Symbiotic* Model provides a self-consistent explanation for the observed complexity of active galaxies.

Acknowledgements.

We thank Sam Falle for providing a version of his hydrodynamic code for us to abuse, and an anonymous referee for a

constructive report which helped clarify the structure of this paper. Computer resources were provided by the University of Leeds and by Starlink (in Cambridge, Cardiff, Leeds and Manchester). ACB and RJRW acknowledge support from PPARC; ACB acknowledges the EU TMR Network (FMRX-CT96-0068) for Infrared Surveys; JJP thanks the Leverhulme Trust for generous support in the early stages of this research.

REFERENCES

Albertsson C., Perry J.J., 1999 (in preparation)
 Arav N., Li Z.-Y., Begelman M.C., 1994, ApJ, 432, 62
 Arav N., Barlow T.A., Laor A., Sargent W.L.W., Blandford R.D., 1998, MNRAS, 297, 990
 Atwood B., Baldwin J.A., Carswell R.F., 1982, ApJ, 257, 559
 Baade W., Minkowski R., 1954, ApJ, 119, 206
 Bahcall J.N., Kirhakos S., Schneider D.P., 1997, in Quasar Hosts, proceedings of the ESO/IAC workshop, eds Clements D.L., Perez-Fournon, I., (Springer)
 Baldwin J.A., Wampler E.J., Gaskell C.M., 1989, ApJ, 338, 630
 Baldwin J.A., Ferland G.J., Korista K.T., Verner D.A., 1995, ApJ, 455, L119
 Balsara D.S., Krolik J.H., 1993, ApJ, 402, 109
 Bardeen J.M., Wagoner R.V., 1969, ApJL, 158, L65
 Barthel P.D., 1989, ApJ, 336, 606
 Begelman M.C., Rees M.J., 1983, MNRAS, 185, 847
 Begelman M.C., McKee C.F., Shields G.A., 1983, ApJ, 271, 70
 Beltrametti M., Perry J.J., 1980, A&A, 82, 99
 Bernlöhr K., 1993, A&A, 268, 25
 Binney J.J., Tabor G., 1995, MNRAS, 276, 663
 Blackman E.G., Yi I., 1996, ApJ, 461, L21
 Blandford R.D., Rees M.J., 1974, MNRAS, 169, 395
 Blandford R.D., Begelman M.C., 1999, MNRAS, 303, L1
 Boroson T.A., Green R.F., 1992, 80, 109
 Boyce P.J., 1997, in Quasar Hosts, proceedings of the ESO/IAC workshop, eds Clements D.L., Perez-Fournon, I., (Springer)
 Brandl B., Sams B.J., Bertoldi F., Eckart A., Genzel R., Drapatz S., Hofmann R., Löwe M., Quirrenbach A., 1996, ApJ, 466, 254
 Bremer M.N., Fabian A.C., Crawford C.S., 1997, MNRAS, 284, 213
 Brotherton M.S., Wills B.J., Francis P.J., Steidel C.C., 1994, ApJ, 430, 495
 Calzetti D., 1997, AJ, 113, 162
 Chevalier R.A., Clegg A.W., 1985, Nat, 317, 44
 Cid Fernandes R., 1997, in Starburst Activity in Galaxies, eds Franco J., Terlevich R.J., Serrano A., Rev. Mex. A. A. Conf. Ser. 6, 201
 Ciotti L., Ostriker J.P., 1997, ApJL, 487, L105
 Colbert E.J.M., Baum S.A., Gallimore J.F., O’Dea C.P., Christensen J.A., 1996, ApJ, 467, 551
 Collin-Souffrin S., Dyson J.E., McDowell J.C., Perry J.J., 1988, MNRAS, 232, 539
 Collin-Souffrin S., 1993, in Central Activity in Galaxies – From Observational Data to Astrophysical Diagnostics, eds Sandqvist Aa., Ray T.P., (Springer-Verlag) p. 97
 Corbin M.R., 1991, ApJL, 371, L51
 Corbin M.R., Francis P.J., 1994, AJ, 108, 2016
 Czerny B., Elvis M., 1987, ApJ, 321, 305
 David L.P., Durisen R.H., Cohn H.N., 1987, ApJ, 313, 556
 Devereux N.A., 1989, ApJ, 346, 126
 Doane J.S., Mathews W.G., 1993, ApJ, 419, 573
 Donea A.-C., Biermann P.L., 1996, A&A, 316, 43
 Durisen R.H., Burns J.O., 1981, MNRAS, 195, 535

Dunlop J.S., Taylor G.L., Hughes D.H., Robson E.I., 1993, MNRAS, 264, 455

Dyson J.E., Falte, S.A.E.G., Perry J.J., 1981, MNRAS191, 397

Edelson R.A., et al., 1996, ApJ, 470, 364

Espey B.R., Carswell R.F., Bailey J.A., Smith M.G., Ward M.J., 1989, ApJ, 342, 666

Faber S.M., et al., 1997, AJ, 114, 1771

Fabian A.C., Guilbert P.W., Arnaud K., Shafer R.A., Tennant A.F., Ward M.J., 1986, MNRAS, 218, 457

Falle S.A.E.G., Perry J.J., Dyson J.E., 1981, MNRAS, 195, 397

Falle S.A.E.G., 1991, MNRAS, 250, 581

Ferland G.J., 1996, Hazy, a Brief Introduction to Cloudy, University of Kentucky Department of Physics and Astronomy Internal Report

Ferland G.J., Baldwin J.A., Korista K.T., Hamann F., Carswell R.F., Phillips M., Wilkes B.J., Williams R.E., 1996, ApJ, 461, 683

Filippenko A.V., ed., 1992, Relationships between Active Galactic Nuclei and Starburst Galaxies, Astro. Soc. Pac. Conference Series, vol. 31

Francis P.J., Hewett P.C., Foltz C.B., Chaffee F.H., 1992, ApJ, 398, 476

Friaça A.C.S., Terlevich R.J., 1998, MNRAS, 298, 399

Genzel R., Townes C.H., 1987, ARAA, 25, 377

George I.M., Fabian A.C., 1991, MNRAS, 249, 352

Gerhard O.E., Binney J.J., 1985, MNRAS, 216, 467

Greenhill L.J., Gwinn C.R., Antonucci R.R.J., Barvainis R., 1996, ApJ, 472, L21

Gull S.F., Northover K.J.E., 1973, Nat, 244, 80

Heckman T.M., Armus L., Miley G.K., 1990, ApJS74, 833

Hook I.M., McMahon R.G., Boyle B.J., Irwin M.J., 1994, MNRAS, 268, 305

Hunter D.A., Shaya E.J., Holtzman J.A., Light R.M., O'Neil E.J., Lynds R., 1995, ApJ, 448, 179

Hure, J.-M., Collin-Souffrin, S., Le Bourlot, J., Pineau des Forêts, G., 1994, A&A, 290, 19

Innes D., Perry J.J., 1999, (in preparation)

Kippenhahn R., Mestel L., Perry J.J., 1975, A&A, 44, 123 (KMP)

Korista K.T., Hamann F., Ferguson J., Ferland G.J., 1996, ApJ, 461, 641

Kormendy J., Richstone D., 1995, ARAA 33, 581

Kormendy J., et al., 1996a, ApJ, 459, L57

Kormendy J., et al., 1996b, ApJ, 473, L91

Krolik J.H., McKee C.F., Tarter C.M., 1981, ApJ, 249, 422

Krolik J.H., Begelman M.C., 1986, ApJL, 308, L55

Krolik J.H., Kriss G.A., 1995, ApJ, 447, 512

Kukula M.J., Dunlop J.S., Hughes D.H., Taylor G., Boroson T., 1997a, in Quasar Hosts, proceedings of the ESO/IAC workshop, eds Clements D.L., Perez-Fournon, I., (Springer-Verlag)

Kukula M.J., Dunlop J.S., Hughes D.H., Rawlings S., 1997b, in Quasar Hosts, proceedings of the ESO/IAC workshop, eds Clements D.L., Perez-Fournon, I., (Springer-Verlag)

Lamb S., 1999, in Lamb S., Perry J.J., Baker, A., eds, *AGN, Dense Stellar Systems and Galactic Environments*. Astronomical Society of the Pacific: San Francisco, in press

Laor A., 1990, MNRAS, 246, 369

Laor A., Netzer, H. 1989, MNRAS, 238, 897

Larson R.B., 1985, MNRAS, 214, 379

Larson R.B., 1986, MNRAS, 218, 409

Lasota J.-P., Abramowicz M.A., Chen X., Krolik J.H., Narayan R., Yi I., 1996, ApJ, 462, 142

Lauer T.R., et al., 1995, AJ, 110, 2622

Lauer T.R., Faber S.M., Ajhar E.A., Grillmair C.J., Scowen P.A., 1998, AJ, 116, 2263

Maeder A., 1992, A&A, 264, 105

Maiolino R., Krabbe A., Thatte N., Genzel R., 1998, ApJ, 493, 650

Mathews W.G., Ferland G.J., 1987, ApJ, 323, 456

McLeod K.K., Rieke G.M., 1994, ApJ, 420, 58

McLeod K.K., Rieke G.M., 1994, ApJ, 431, 137

McLeod K.K., 1997, in Quasar Hosts, proceedings of the ESO/IAC workshop, eds Clements D.L., Perez-Fournon, I., (Springer)

Mellema G., Frank A., 1995, MNRAS, 273, 401

Murphy B.W., Cohn H.N., Durisen R.H., 1991, ApJ, 370, 60 (MCD)

Murphy, B.W., Perry, J.J., 1999 (in preparation)

Mushotzky R.F., Ferland G.J., 1984, ApJ, 278, 558

Muxlow T.W.B., Pedlar A., Wilkinson P.N., Axon D.J., Sanders E.M., de Bruyn A.G., 1994, MNRAS, 266, 455

Nandra K., Pounds K.A., 1994, MN 268, 405

Narayan R., Yi I., 1994, ApJ, 428, L13

Neff S.G., Hutchings J.B., 1992, AJ, 103, 1746,

Netzer H., 1990, in Active Galactic Nuclei, Blandford R.D., Netzer H., Woltjer L., Springer Verlag: Berlin, 57

Netzer H., Peterson B.M., 1997, in Astronomical Time Series, Proceedings of the Wise Observatory 25th Anniversary Symposium, eds. Maoz D., Sternberg A., Leibowitz E.M., Kluwer: Dordrecht, p. 85

Newman J.A., Eracleous M., Filippenko A.V., Halpern J.P., 1997, ApJ, 485, 570

Norman C.A., Scoville N.Z., 1988, ApJ, 332, 124

Norman M.L., Smarr L., Wilson J.R., Smith M.D., 1981, ApJ, 247, 52

Osterbrock D.E., 1991, Rep. Prog. Phys., 54, 579

Padovani P., Burg R., Edelson R.A., 1990, ApJ, 353, 438

Penston M.V., et al., 1990, A&A, 236, 53

Perry J.J., Dyson J.E., 1985, MNRAS, 235, 665 (PD)

Perry J.J., 1992, in Relationships between Active Galactic Nuclei and Starburst Galaxies, ed. Filippenko A.V., (Astro. Soc. Pac. Conference Series) p. 169.

Perry J.J., 1993a, in Central Activity in Galaxies – From Observational Data to Astrophysical Diagnostics, eds Sandqvist Aa., Ray T.P., (Springer-Verlag) p. 25

Perry J.J., 1993b, in Rocca-Volmerange B., Dennefeld M., Guidoroni B., Tran Thanh Van J., eds, First Light in the Universe – Stars or QSOs? Éditions Frontières, Gif-sur-Yvette, 225

Perry J.J., Williams R.J.R., 1993, MNRAS, 260, 437

Perry J.J., van Groningen E., Wanders I., 1994, MNRAS, 271, 561

Perry J.J., 1994, in Reverberation mapping of the broad-line region in Active Galactic Nuclei, eds. Gondhalekar, P.M., Horne, K., Peterson, B.M., (ASP Conf. Series) 69 357

Perry J.J., 1999, in Lamb S., Perry J.J., Baker A.C., eds, *AGN, Dense Stellar Systems and Galactic Environments*. Astronomical Society of the Pacific: San Francisco, in press

Perry J.J., Williams R.J.R., Dyson J.E., (in preparation)

Pettini M., Smith, L.J., Hunstead, R.W. King, D.L., 1994, ApJ, 426, 79

Pettini M., Smith, L.J., King, D.L. Hunstead, R.W., 1997, ApJ, 486, 665

Quinlan G.D., Shapiro S.L., 1990, ApJ, 356, 483

Quirk J.J., 1994, International Journal for Numerical Methods in Fluids, 18, 555

Rees M.J., Netzer H., Ferland G.J., 1989, ApJ, 347, 640

Reynolds C.S., Fabian A.C., 1995, MN 273, 1167

Rieke G.H., Lebofsky M.J., Thompson R.I., Low F.J., Tokunaga A.T., 1980, ApJ, 238, 24

Rieke G.H., Loken K., Rieke M.J., Tamblyn P., 1993, ApJ, 412, 99

Röser H.-J., 1979, A&A, 80, 179

Sanders D.B., Soifer B.T., Elias J.H., Madore B.F., Matthews K., Neugebauer G., Scoville N.Z., 1988, ApJ, 324, 74

Sanders D.B., Phinney E.S., Neugebauer G., Soifer B.T., Matthews K., 1989, ApJ, 347, 29

Sanders D. B., Mirabel, I. F., 1996, ARAA, 34, 749

Scalo J.M., 1990, in Windows on Galaxies, eds. Fabbiano G., Gallagher J.A., Renzini A., Kluwer: Dordrecht, 125

Shlosman I., ed., 1994, Mass-Transfer Induced Activity in Galaxies, Cambridge U.P.: Cambridge

Shakura N.I., Sunyaev R.A., 1973, *A&A*, 24, 337

Shields G.A., 1978, *Nat*, 272, 706

Shull J.M., 1983, *ApJ*, 264, 446

Shlosman I., Begelman M.C., Frank J., 1990, *Nat*, 345, 679

Shull J.M., Saken J.M., 1995, *ApJ*, 444, 663

Silk J., 1977, *ApJ*, 214, 718

Silk J., 1995, *ApJ*, 438, L41

Silk J., Perry, J.J., 1999 (in preparation)

Smith M.D., Smarr L., Norman M.L., Wilson J.R., 1981, *Nat*, 293, 277

Smith M.D., Smarr L., Norman M.L., Wilson J.R., 1983, *ApJ*, 264, 432

Smith S.J., Kennel C.J., Coroniti F.V., 1993, *ApJ*, 412, 82

Steffen W., Gómez J.L., Raga A.C., Williams R.J.R., 1997, *ApJ*, 491, L73

Steidel C.C., Giavalisco M., Pettini M., Dickinson M., Adelberger K.L., 1996, *ApJ*, 462, L17

Suchkov A.A., Berman V.G., Heckman T.M., Balsara D.S., 1996, *ApJ*, 463, 528

Sulentic J.W., Marziani P., Dultzin-Hacyan D., Calvani M., Moles M., 1995, *ApJL*, 445, L85

Sun W.-H., Malkan M.A., 1989, *ApJ*, 346, 68

Taylor D., Dyson J.E., Axon D.J., 1992, *MNRAS*, 255, 351

Taylor G.L., Dunlop J.S., Hughes D.H., Robson E.I., 1996, *MNRAS*, 283, 930

Terlevich R.J., 1990, in Windows on Galaxies, eds. Fabbiano G., Gallagher J.A., Renzini A., p87

Turner T.J., Nandra K., George I.M., Fabian A.C., Pounds K.A., 1993, *ApJ*, 419, 127

Turnshek D.A., 1988, in QSO Absorption Lines, Blades J.C., Turnshek D.A., Norman C.A., eds, Cambridge U.P., 17

Tytler D., Fan X.-M., 1992, *ApJS*, 79, 1

Veilleux S., Cecil G., Bland-Hawthorn J., Tully R.B., Filippenko A.V., Sargent W.L.W., 1994, *ApJ*, 433, 48

Voit G.M., 1994, *ApJL*, 432, 19

Wanders I., Peterson B.M., 1996, *ApJ*, 466, 174

Watson A.M., 1999, in Lamb S., Perry J.J. Baker A.C., eds, *AGN, Dense Stellar Systems and Galactic Environments*. Astronomical Society of the Pacific: San Francisco, in press

Wiita P.J., 1978a, *ApJ*, 221, 41

Wiita P.J., 1978b, *ApJ*, 221, 436

Williams R.J.R., Dyson J.E., 1994, *MNRAS*, 270, L52

Williams R.J.R., Perry J.J., 1994, *MNRAS*, 269, 538

Williams R.J.R., 1999, in Lamb S., Perry J.J. Baker A.C., eds, *AGN, Dense Stellar Systems and Galactic Environments*. Astronomical Society of the Pacific: San Francisco, in press

Woods D.T., Klein R.I., Castor J.I., McKee C.F., Bell J.B., 1996, *ApJ*, 461, 767

Zepf S.E., Silk J., 1996, *ApJ*, 466, 114

Zheng W., Malkan M.A., 1993, *ApJ*, 415, 517

Zycki P.T., Collin-Soufrin S., Czerny B., 1995, *MNRAS*, 277, 70

APPENDIX A: DETAILS OF THE PHYSICAL ASSUMPTIONS

In this appendix, we discuss in more detail the assumptions of our model. The presentation progresses from the structures within the nucleus – the black hole, starburst stellar cluster and accretion disc – to the properties of the radiation field, thermal equilibrium of the nISM and treatment of accretion.

A1 Black Hole

Since the bolometric luminosities of most AGN can be determined to order-of-magnitude or better, the combined issues of black hole masses and Eddington ratios are strongly linked.

Indications of the masses of dark objects in nearby galaxies have been obtained from the brightness distribution and stellar kinematics in their cores. The masses inferred to reside in dark, unresolved cores vary from $2 \times 10^6 M_\odot$ in the Galaxy and M32 to around $3 \times 10^9 M_\odot$ in M87 (Kormendy & Richstone 1995). The sample of galaxies observed is at the moment rather sparse and heterogeneous, but the presence of these ‘dark objects’ suggests that there may be enough nuclear black holes of sufficient mass to satisfy our model.

Limits on have also been derived on black hole masses in active AGN. Some attempts have been made to estimate the mass function using simple estimates of the black hole mass (e.g. Padovani, Burg & Edelson 1990), but has only been very recently that radio observations of maser emission and detailed line profile studies have begun to give well-constrained dynamical masses for black holes, in the range 10^7 – $2 \times 10^8 M_\odot$ (Greenhill et al. 1996; Lasota et al. 1996; Newman et al. 1997).

A2 The Stellar Cluster

Dynamics We base our assumptions about the dynamics of the nuclear stellar cluster in the models of MCD. They modelled the evolution of the stellar cluster around a central black hole by a multi-mass energy-space Fokker-Planck code, including the effects of tidal disruption, physical collisions between stars and of stellar evolution.

As our aim is to model the hydrodynamics of the nuclei, we only include their results in a schematic fashion. MCD find that the dynamical evolution of the stellar clusters occurs, for the most part, in the cluster cores. For initial stellar densities below $10^7 M_\odot \text{ pc}^{-3}$, the dynamical evolution of the cluster is dominated by tidal disruption, leading to a core density law $s = 7/4$ (as predicted by early models of this process), while for higher stellar densities collisions dominate the core evolution and mass loss, giving a core power-law of $s = 1/2$.

Beyond the core, the density law in the models presented by MCD remains roughly constant, except for the effects of stellar evolution. In their initial Plummer model, MCD take the halo power-law index to be $h = 5$. Beyond 10 pc, the stellar density will be dominated by the normal stellar distribution of the central regions of the galaxy. The precise form of the halo power law and the surrounding galactic bulge are not well determined. However, they will have only a small effect on the hydrodynamic models of the flows inside the BELR that we present here.

The relationship between the enclosed mass and radius in the Galactic centre between 1 and 100 pc is roughly $M \simeq 3 \times 10^6 r_{\text{pc}}^{1.2} M_\odot$ (Genzel & Townes 1993), implying stellar densities $n_\star \simeq 10^5 (M_\star/1 M_\odot)^{-1} r_{\text{pc}}^{-1.8} \text{ pc}^{-3}$. Within the Galactic centre, the cluster of 10^8 or $10^9 M_\odot$ which we discuss here would be a dynamically independent system. Indeed, any such cluster would dominate the dynamics of at least the central 100 pc of the Galaxy. In NGC 3115, a dense stellar cluster of mass $\sim 4 \times 10^7 M_\odot$, distinct from

the core of the galaxy, appears to surround a dark object (perhaps black hole) of mass $\sim 10^9 M_\odot$ (Kormendy et al. 1996a), although such distinct stellar clusters are not found around all candidate massive dark objects (Kormendy et al. 1996b).

HST observations have provided evidence for stellar densities at least $> 10^7 M_\odot \text{ pc}^{-3}$ in M32 (Lauer et al. 1998). It is more difficult to observe such dense compact clusters in more distant galaxies, but the properties at larger radii seem similar to M32, and nuclear clusters of $10^7 L_\odot$ are certainly observed (Lauer et al. 1995), although there is no strong evidence for stellar densities above $10^6 M_\odot \text{ pc}^{-3}$ (Faber et al. 1997). Faber et al. find that the density decreases quite strongly as the mass of the cluster increases, while the velocity dispersion in the clusters varies only weakly; they also suggest that the cluster masses in these objects are between 3 and 6 times those of the massive dark objects they harbour. A cluster with mass $\sim 6 \times 10^7 M_\odot$ contained within 6 pc of an $4 \times 10^6 M_\odot$ black hole is seen in the Circinus galaxy, the most nearby known Seyfert 2 (Maiolino et al. 1998).

The clusters which we discuss here would only be resolvable in nearby galactic nuclei (although their gravitational effects would extend over a larger radius). While the nucleus was active, their presence would be masked by the active QSO and at later epochs much of their mass may have been lost to the nucleus in a wind or accreted by a black hole as a result of stellar evolution or stellar collisions. Clusters with these high densities are a requirement of the PD model if stellar mass loss envelopes are to generate the required covering fractions of cool gas within the BELR. However, clusters at least as dense are required by many models of the formation of the central massive black hole (e.g. Begelman & Rees 1978; Quinlan & Shapiro 1990), so it is not unreasonable to consider the properties of a black hole surrounded by the flotsam of its formation.

The stellar cluster models of MCD are, as a matter of computational necessity, spherically symmetric. In the initial hydrodynamic models presented here, we follow this assumption. In general, if the young star cluster were to form as a thin disc, non-axisymmetric instabilities will thicken its central regions substantially within a dynamical timescale, to generate a bulge-disc structure reminiscent of a spiral galaxy. If the clusters remain aspherical enough to influence our models, they would either consist of stars on plunging box-type orbits or have significant net angular momentum. In the first case, the aligned orbits would rapidly be randomised by the influence of the central black hole (Gerhard & Binney 1985). In the second case, for self consistency, we should then also include the angular momentum of the flow, a topic we leave for a subsequent paper.

Even in the core of a nuclear starburst, the pressure, typically 10^7 K cm^{-3} (Suchkov et al. 1996), is significantly less than the pressure in the BELR of AGN. We have chosen to neglect this extranuclear gas in the simulations presented here, as the rate of mass input into the central parsec-scale region will depend strongly on the transport of angular momentum. Detailed simulations of the gas dynamics of galaxies with active nuclei will allow us to correct this in future papers.

Stellar mass loss The manner in which mass is lost from stars and added to the flow has an effect on our simulations on various scales. The overall normalization of the stellar mass loss, within our assumptions, sets the overall normalization of the density, but does not alter the kinematics of the flow. Variations in mass input across the core (for instance, if the stellar cluster is oblate rather than spherical) will alter the form of the flow, but we argue (in Appendix A2) that this will not have a major influence on the structure of the flow. The graininess of the mass input, on the scale of the individual interactions between stars and the global ISM, is determined by the mode of stellar mass loss (through supernovae, stellar winds, collisions, etc.). This can have consequences for the thermal structure of the flow. Perhaps the most important consequence of these interactions will be the production of cool gas which will emit optical and UV emission lines (PD).

In all the models presented above, we take the input rate of gas into the cluster to be proportional to the stellar density. The scaling chosen, $\dot{q} = Q\rho_*$ with $Q = 3 \times 10^{-16} \text{ s}^{-1} \simeq 10^{-8} \text{ yr}^{-1}$, is appropriate for mass loss from a young stellar cluster with a lower mass cut off above $4 M_\odot$ (Shull 1983; Williams & Perry 1994, in particular their Fig. 3b). In this way, our assumptions differ from those of MCD who used a broad IMF, extending from stellar masses as low as $M_* = 0.3 M_\odot$. For IMFs extending to such low masses, collisional mass loss exceeds stellar mass loss at the very smallest radii (Murphy & Perry 1999).

Rieke et al. (1980) suggested that IMFs with lower mass cutoffs above a few solar masses were necessary to explain the high supernova rates and $2 \mu\text{m}$ luminosities for the derived dynamical mass in the best studied starburst galaxy, M82 (see also Rieke et al. 1983; Doane & Mathews 1993; Bernlöhr 1993). Studies of the variation of the mass-to-light ratio and metallicity with galaxy mass for ellipticals also suggest that ‘bimodal’ star formation occurs in some circumstances (Larson 1986; Zepf & Silk 1996). High-biased IMFs may be particularly favoured in the highly sheared environment of a galactic nucleus, if the increase in pre-collapse density required for higher shears is outweighed by increased internal energy resulting from turbulence and heating of the cloud gas (cf. Silk 1977, 1995; Larson 1985).

It should be noted that the observational evidence for high-biased IMFs is not clear cut (Scalo 1990). Detailed models of the distribution of dust can explain the broad band spectra at the required mass-to-light ratio with normal IMFs (Devereux 1989; Calzetti 1997). In M82, the distribution of sizes of the radio supernova remnants (and the unchanged population over a 10 year period) suggest that the supernova rate was initially overestimated (Muxlow et al. 1994). While some Galactic open clusters are deficient in the $1-10 M_\odot$ range (Scalo 1990), in the best nearby analogue of a starburst system, the central region of 30 Doradus, imaging studies find populations of stars down to $3 M_\odot$ with no sign of differences in the global IMF (Hunter et al. 1995; Brandl et al. 1996).

Note that we assume the formation of the cluster occurs on a timescale of a few million years or less. Many of the constraints described on the number of quiescent low-mass stars in the starburst IMF become yet more stringent if stars have formed over a period significantly longer than the main sequence lifetime of the massive stars, since they depend

not on the rate of formation but on the total mass of low-mass stars. There is good evidence that the formation of massive stars in OB associations is coeval to within 20 Myr (Shull & Saken 1995), with the massive stars destroying their nascent star forming region (perhaps encouraging further generations of massive stars to form at a larger distance). It is not unreasonable for closely synchronized star formation to have occurred in the compact stellar clusters we discuss, since the dynamical timescales are short, and even at 10^4 K the sound-crossing time of the nucleus is only 10^5 yr.

Less high-biased stellar IMFs will decrease the mass input rate, and hence the density scale will be lower. Different modes of stellar mass loss, driven by stellar collisions, tidal disruption or the effects of the nuclear radiation, will boost the mass input rate, albeit with a different spatial distribution. It does become difficult to produce the required luminosity in such low-loading models, unless the cluster mass is extremely large.

Stellar mass-loss through collisions is a threshold process: the collisions lead to disruptions when the impact velocity is greater than the surface binding energy of the stars (cf. MCD). If the velocity dispersion varies with radius, this implies that collisional mass loading can occur from any individual class of stars wherever the dispersion is greater than the stellar escape velocity. From the above discussion, we see that within the core, head-on collisions are likely either to be disruptive through most of the core (where $v_K > v_*$), or not at all. The collisional mass-loading term may then be given by

$$\dot{q}_{\text{coll}} = M_* n_*^2 v_K A_* \quad (\text{A1})$$

when $v_K > v_*$, and zero otherwise. For our purposes, this only need be applied to main sequence stars, since giants will soon lose their extended envelopes as a result of stellar winds and supernovae. Collisional mass loss will thus only be important when $\tau_{\text{coll}} = 1/n v_K A_* < \tau_*$. Since for a uniform cluster $\tau_{\text{coll}} \simeq 10^{10} r_{\text{pc}}^{7/2} M_{\text{c},8}^{-3/2}$ yr, roughly independent of stellar mass (Perry & Williams 1993), collisions are only likely to be an important factor in stellar mass loss only for the small fraction of stars in the central density cusp, or in the densest of nuclear clusters (cf. MCD, Murphy & Perry 1999).

Close to the central black hole there is an exceptional region of increased velocity dispersion. An ‘extended loss cone’ may form, for which the vigour of the stellar environment in the velocity cusp performs a similar destructive role to the high tidal field of the black hole at yet smaller radii. This region, together with that in which mass is input by tidal disruption, is not resolved by our simulations. Central collisions could most easily be catered for by an unresolved central mass addition term, to be traded off against the condensation of mass onto an accretion disc.

Effects of Loading Distribution We assume spatially smooth mass loading. The validity of this assumption depends on the efficiency of mixing between mass input and global flow, and on the manner in which stars lose mass. Supernovae, tidal disruption and head-on collisions will add mass in very localized regions, but initially with a wide range of velocities. Smooth mass loading may be a rather rough approximation where these effects dominate the mass input: indeed in Seyfert nuclei, individual supernovae will

be rare, but may be able to blow away much of the nISM (PWD). However, sufficiently many supernovae should occur in a QSO that smooth loading is a reasonable first approximation (PD).

Mass loss by stellar winds will result in a smoother spatial distribution of mass-loading, as many sources are active at any time, and each one is active for many dynamical timescales. Maeder (1992) suggests that for solar-abundance stars over $25 M_\odot$, most of the stellar mass is ejected in before the supernova explosion. For stars of $40 M_\odot$ or over, the mass of the pre-supernova star is less than $8 M_\odot$. The fraction of mass lost pre-supernova may be further increased by the higher metallicities expected in nuclear stellar clusters. Glancing collisions, particularly with the envelopes of giant stars, will also load the region in a gradual fashion.

The large-scale distribution of loading is important when $r\dot{q} \gtrsim \rho v$ [from comparison of terms in the equations of mass conservation and motion, eqs (13) and (14)]. Hence, the details of the mass input distribution are important in the outer accretion flow and close to stagnation points (where $v \sim 0$). If, in the absence of accretion, the central convective region has size r_{con} at time t (where r_{con} saturates at r_c at time t_{fill} when the wind mass loss becomes equal to the mass input, after which time we should substitute $t = t_{\text{fill}}$ in the following expression), we find that within the convective structure

$$\frac{r_{\text{con}} \dot{q}}{\rho v} \simeq \left(\frac{r_{\text{con}}}{r_c} \right)^3 \frac{t_{\text{dyn}}}{t}, \quad (\text{A2})$$

where $t_{\text{dyn}} = r_{\text{con}}/v$. Unless the onset of outflow is prompt (i.e. within a dynamical timescale), the precise form of mass loading distribution through the cluster core will be unimportant. Even if the outflow is prompt, its structure will be simple: the central outflow will still be independent of the form of the mass loading, and the outer structures will be ballistic (cf. Model A). We will investigate these assumptions in more detail in a future paper.

A3 The Accretion Disc

In the limit of low external pressure, a thin accretion disc will have a corona-wind structure similar to stellar wind models. The rate of mass loss in the wind would depend on the incident flux (whether direct from the nucleus or back-scattered from the nISM) and the structure of the disc (self-gravity may well lead to a rather clumpy structure at these radii), and will be influenced by magnetic fields and angular velocities.

However, the models we have calculated show that the flow pressure tends to be high in the plane of the disc. The radiation intensity is low in the disc plane. Confined, high pressure gas may cool, adding gas to the disc. The importance of this process depends on the ratio of the cooling time of the shocked gas to the flow time through the high-pressure region. In one limit, essentially all the gas will ‘collapse’ onto the disc surface. In the other, mass addition from the wind would have a negligible effect.

To treat these processes accurately requires detailed heating/cooling models of the flow in and around the disc. The length- and time-scales important for such models are difficult to include in a global model for the nuclear flow. Woods et al. (1996) treat the evaporation of gas from the

disc surface, using an adaptive grid technique. In their model, the regions of cool gas are localized near the disc surface: in general, where the unstable *cooling* of the gas may be important, complicated turbulent structures would quickly overwhelm any adaptive grid model with irrelevant detail. To study these cases, local results on the detailed structure of the flow must be smoothed to predict the mean properties of gas on a global scale.

A4 Gravity

The gravitational forces are dominated by the central accreting black hole (point source), and the nuclear starburst stellar cluster. We discuss observational constraints on the masses of these components in Appendices A1 and A2, respectively.

We do not include the gravitational field of the interstellar gas. At any time, the integrated mass in the ISM interior to 1 pc is far smaller than that of the stellar cluster, since gas will not be retained in the nuclear ISM for longer than the average stellar lifetime $\gtrsim 10^6$ yr. If the mass of the ISM were gravitationally significant, the nucleus would be optically thick to Thomson scattering and X-ray absorption, and the ISM would rapidly cool by bremsstrahlung.

The accretion disc is limited by its vulnerability to local self-gravitating instabilities, to have a density no greater than the tidal density,

$$\rho_T = \frac{M_h + M_{\text{cl}}(< r)}{(4/3)\pi r^3}, \quad (\text{A3})$$

and hence it can contribute no more than H/r of the gravitating mass.

For the model stellar cluster given by equation (2), the cluster mass is given by

$$M_{\text{cl}} = \frac{h-s}{(3-s)(h-3)} 4\pi \rho_{\star,c} r_c^3 = \frac{h-s}{h-3} M_c, \quad (\text{A4})$$

where the core mass M_c is

$$M_c = \frac{1}{3-s} 4\pi \rho_{\star,c} r_c^3. \quad (\text{A5})$$

The gravitating mass of stars inside radius r is then $\mu_{\star}(r/r_c)M_{\text{cl}}$, where

$$\mu_{\star}(r/r_c) = \begin{cases} \frac{h-3}{h-s} \left(\frac{r}{r_c}\right)^{3-s} & r < r_c \\ 1 - \frac{(3-s)(r/r_c)^{3-h}}{(h-s)} & r > r_c. \end{cases} \quad (\text{A6})$$

A5 Radiation

The dynamical effects of the black hole are not limited to its gravitational attraction – the high luminosity generated by accretion will generate a significant outward radiation force. Accretion on to a black hole at a rate \dot{M}_a will produce a luminosity of

$$L_{\text{Bol}} = \eta_{\text{acc}} \dot{M}_a c^2 \quad (\text{A7})$$

where η_{acc} is an efficiency factor, of order 0.1. In this paper, we have taken the driving to result from optically thin Thomson opacity only, as it is the dominant opacity when the nISM is at the Compton temperature. The dynamical

effect of this radiation can be parameterised in terms of the angle-averaged Eddington ratio

$$\langle f_{\text{Edd}} \rangle \equiv L_{\text{Bol}} / L_{\text{Edd}}, \quad (\text{A8})$$

between the central bolometric luminosity and the Eddington limit luminosity, cf. equation 6.

The broadband continua of many AGN are dominated by a quasi-thermal ‘bump’ at UV wavelengths (Sanders et al. 1989; Zheng & Malkan 1993), which is believed to be emitted by the central regions of an accretion disc (Shields 1978; CDMP). If this is so, the intensity of the UV radiation field will have an angular dependence similar to $F(\theta) \propto (\cos \theta)^{\alpha}$, with $\alpha = 1$. Netzer (1990) suggests that using $F(\theta) \propto \cos \theta (1 + 1.5 \cos \theta)$ better accounts for the effects of limb-brightening at optical wavelengths (Laor & Netzer 1989; Penston et al. 1990) find that for NGC 4151, intrinsic continuum anisotropy (as opposed to reddening) must be part of the reason for the decrement in ionizing luminosity by a factor ~ 13 between that observed and that inferred to excite the ENLR emission in the galaxy. While using $\alpha = 1.5$ gives an almost identical $F(\theta)$ to this, we can also obtain a very similar fit (at the important angles where the net force is outward) by rescaling the hole mass and Eddington ratios, keeping $\alpha = 1$. For example, as a test case, we treated a model in which $\alpha = 1.5$, with all other parameters as in Model B, were almost identical to those for Model A with $\alpha = 1$ (with flow velocities about 15 per cent smaller, as expected). Hence we will only present results the simplest model here.

We smooth the radiation field close to the centre of the nucleus, principally for numerical reasons. However, the radiation field may be physically smoothed in many sources, if the nISM is optically thick to scattering close to the nucleus. The anisotropic component of the radiation will mostly be emitted within a radius roughly determined by the black body emission law

$$r_{\text{emit}} \simeq (L_{\text{disc}} / 2\pi\sigma_{\text{SB}} T_{\text{m}}^4)^{1/2} \simeq 0.017 L_{46}^{1/2} T_{\text{m},4}^{-2} \text{ pc}, \quad (\text{A9})$$

where σ_{SB} is the Stefan-Boltzmann constant, and $T_{\text{m},4} \simeq 3$ for observed accretion discs (with a broad scatter, Zheng & Malkan 1993). The temperature profile $T(r)$ of a geometrically-thin, optically-thick disc heated either by external irradiation or viscous dissipation is

$$T \simeq 500 L_{46}^{3/8} T_{\text{m},4}^{-1/2} r_{\text{pc}}^{-3/4} \text{ K}. \quad (\text{A10})$$

It should be noted that $\langle f_{\text{Edd}} \rangle$, f_{disc} and M_h are not actually independent parameters of the hydrodynamical model. The net force close to the centre (taking account of radiative forces) can be described by an equivalent gravitating mass

$$M_{\text{net}}(\theta) = M_h - [1 - f_{\text{disc}} + 2f_{\text{disc}} \cos \theta] \langle f_{\text{Edd}} \rangle M_h, \quad (\text{A11})$$

which is determined by only two parameters. However, we retain all three parameters, because of their physical relevance – processes outside the domain of our hydrodynamic models, such as the stellar dynamics close to the black hole or the details of the inner accretion disc do, of course, depend on the separate values of these parameters.

A6 The thermal state of the nISM

The thermal equilibrium of the nISM is controlled by Compton heating and cooling. Neglecting relativistic and occupation number effects, the net Compton heating rate, per unit volume, is

$$Q_C = \frac{4\pi n_e \sigma_T}{m_e c^2} \left[\int J_\nu h\nu d\nu - 4k_B T_e \int J_\nu d\nu \right]. \quad (\text{A12})$$

The ratio between the Compton cooling time and the flow time ($\simeq r_{\text{pc}}/\mathcal{M}T_7^{1/2}10^{11}$ s) is

$$\frac{t_{C,v}}{t_f} \approx 8 \times 10^{-2} \frac{r_{\text{pc}} \mathcal{M} T_7^{1/2}}{f_{\text{Edd}} M_{h,8}}, \quad (\text{A13})$$

where \mathcal{M} is the flow Mach number, and T_7 its temperature in units of 10^7 K. The Compton heating time is T/T_C times $t_{C,v}$. Only at velocities comparable to or smaller than the sound speed can the temperature structure of the ISM gas have a significant dynamical effect on the gas flows. Thus, adiabatic expansion can begin to cool the global gas flow substantially below the Compton temperature only at large radii ($\gtrsim 10$ pc). The wind velocity will already be supersonic by the time gas reaches radii large enough that it can cool – it will coast outwards on its residual momentum until it hits the galaxy ISM.

We have taken the Compton temperature as uniform throughout the flow. This approximation may break down for a variety of reasons. The variation in the contribution of the accretion disc compared to the direct radiation from the central source will almost certainly change the spectrum; indeed, the spectrum of the accretion disc itself depends on azimuthal angle in some models (Sun & Malkan 1989), although not all (Czerny & Elvis 1987). It may also vary with distance from the nucleus as a result of, for instance, photoelectric absorption or oblique scattering by moving gas (although these processes will only be important once the Thomson optical depth though the ISM is close to unity). The temperature will also increase, at smaller distances than our simulations resolve, as a result of stimulated Compton scattering (cf. Rees, Netzer & Ferland 1989).

The likely variation in Compton temperature of the gas with the strength of the accretion disc component may be investigated by varying the strength of the UV bump in the spectrum, and solving equation (A12) (or, in these results, more accurately by including relativistic corrections to the cross section, as in Rees, Netzer & Ferland 1989). We compared the results for the default spectrum given in Cloudy (Ferland 1996) with the same spectrum with a power-law interpolation under the UV bump component. Without the bump, the Compton temperature increases from 1.3×10^7 K to 2.6×10^7 K, and the luminosity is cut to 0.52 of its previous value: the UV bump has a negligible effect on Compton heating, so $T_C \propto 1/(1 + f_{\text{disc}})$. Thus, the variation in the Compton temperature with azimuthal angle is likely to be small enough to be negligible (if the broad-band continuum is isotropic). This also suggests that, taking this mean spectrum to correspond to a population average, the luminosity of the reflected component is characteristically equal to the broad-band component (detailed studies of form of the X-ray spectrum, as determined by Compton reflection, suggest a similar result, e.g. George & Fabian 1991).

Whether Comptonization is sufficient to maintain strict isothermality or not, it is likely that the flow will remain hot, at least until bremsstrahlung cooling becomes comparable to Comptonization, which occurs when the flow density increases above

$$n_{\text{Br}} \simeq 3 \times 10^5 \frac{f_{\text{Edd}} M_{h,8}}{r_{\text{pc}}^2 T_7^{1/2}} \text{ cm}^{-3}, \quad (\text{A14})$$

i.e. the hot phase ionization parameter decreases below $\Xi \simeq 50T_7^{-3/2}$. In some of the simulations presented here, particularly where gas is retained for many dynamical times, the densities violate this limit in some places. The extension of the models presented here to treat the effects of gas with cooling not dominated by Compton upscattering is discussed in Section 7.4.

We can, however, maintain the physical relevance of our models either by rescaling dimensional parameters – loading rates, sizes, sound speeds – or by accepting that the gas will cool (thereby increasing the mean opacity and the effective radiative driving force). We discuss these implications more fully in Section 7.4 – for the present, it sufficient to warn that scale of the densities in the models we present must be treated with caution: relative values and flow topologies are likely to accurate nevertheless.

APPENDIX B: EVOLUTION OF ISOTHERMAL FLOWS IN STELLAR CLUSTERS

In this appendix, we derive an approximate analytic model for the transient behaviour of an isothermal ($c_s = \text{const}$) flow in a uniform, spherical stellar cluster with no black hole. This model serves as a test case for our numerical models. It also illustrates that even in spherical symmetry, the flows within stellar clusters can take very many dynamical timescales to reach equilibrium.

We consider the case where the Keplerian velocity at the edge of the cluster is supersonic, $v_K \gtrsim c_s$. When this is not the case, gravitational effects are negligible, and the flow will relax to equilibrium on a sound-crossing timescale. Here, we derive how this relaxation timescale increases as the gravitational field increases.

We take the stellar cluster to have a uniform core and no halo, i.e. $s = 0$ and $h = \infty$. The mass loading rate, \dot{q} , is uniform throughout the cluster following its abrupt turn-on at time $t = 0$. The gravitational force is then

$$g = \begin{cases} \left(\frac{v_K}{r_c}\right)^2 r & \text{for } r \leq r_c \\ \left(\frac{v_K}{r}\right)^2 r_c & \text{for } r > r_c, \end{cases} \quad (\text{B1})$$

where $v_K^2 \equiv GM_c/r_c$.

If there were free accretion at the centre of the cluster, the flow would relax to a doubly-sonic equilibrium solution. This solution has an outward-going sonic point at a radius $r_s^+ \simeq (v_K^2/2c_s^2)r_c$ (where the flow density is ρ^+), and an inner sonic point within the cluster. The ratio of mass fluxes between outer and inner sonic radii is

$$\frac{4\pi(r_s^+)^2 \rho^+ c_s}{4\pi(r_s^-)^2 \rho^- c_s} = \left(\frac{r_s^+}{r_s^-}\right)^2 \frac{\rho^+}{\rho^-}. \quad (\text{B2})$$

While the area ratio increases between the sonic radii, the

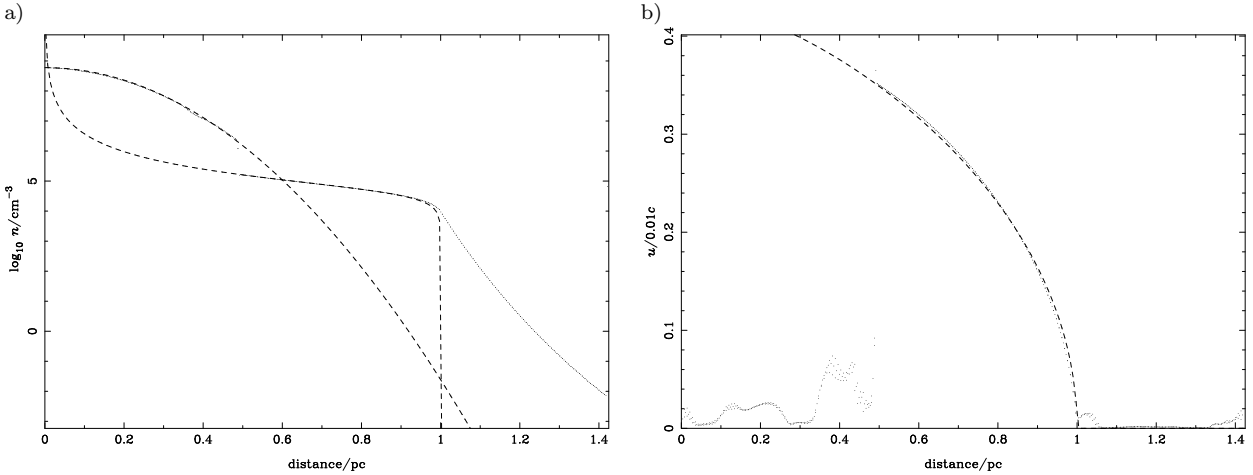


Figure B1. A section through Model \mathcal{O} , shown in Fig. 4 (in which $m_K = 7$). The points plotted show a) density b) total velocity, along the line $r = z$. In a), dashed lines show the density derived from the hydrostatic model for the core and the ballistic model for the accreting halo. The velocity profile in the accreting halo model is shown in b). The numerical results agree well with the core model inside the shock at $r \simeq 0.5$ pc, and with the accreting halo model beyond it. Small deviations in the core probably result from vibrations or some supra-thermal support by turbulence.

density decreases exponentially in the near-hydrostatic region between the sonic points and the total mass flux ratio is small, so little mass is lost to the cluster at this stage. The stagnation radius, r_0 , (where the flow velocity is zero) is only just inside the edge of the cluster core.

To determine the flow within the cluster, we use the mass and momentum equations, equation (13) (integrated, assuming the stagnation radius is coincident with the edge of the cluster) and (14), to obtain

$$3r^2\rho v = -\dot{q}(r_c^3 - r^3) \quad (B3)$$

$$(v^2 - c_s^2) \frac{dv}{dr} = -\frac{v_K^2}{r_c^2} rv - \frac{\dot{q}}{\rho} (v^2 + c_s^2) + 2\frac{vc_s^2}{r}. \quad (B4)$$

Below, we use dimensionless variables $m = v/c_s$ and $x = r/r_c$ (so that $m_K = v_K/c_s$ is the Mach number at the Keplerian velocity).

We approximate the accretion flow by free-fall collapse. This will be strictly applicable only when there is an inner sonic point, which we find is at x_s given by

$$(m_K^2 x_s^2 - 2)(1 - x_s^3) = 6x_s^3. \quad (B5)$$

This equation has no solutions for x_s between 0 and 1 if $m_K < 2 \times 2^{2/3} \simeq 3.17$. For $m_K > 3.2$, the relevant solution, x_s^- , may be approximated by expanding equation (B5) about $x_s^- = 1$:

$$x_s^- \simeq \frac{m_K^2 - 4}{m_K^2 - 2}. \quad (B6)$$

Assuming $x < x_s^- \sim 1$, we take $c_s \simeq 0$ in equation (B4) to obtain

$$m \frac{dm}{dx} = -m_K^2 x + \frac{3x^2 m^2}{1 - x^3}. \quad (B7)$$

Taking $m = 0$ at $x = 1$ we find the inward velocity is

$$v = -v_K \times (1 - x^3)^{-1} \sqrt{\frac{9 - 20x^2 + 16x^5 - 5x^8}{10}}. \quad (B8)$$

When the accretion rate at the centre is less than that

at which mass is added throughout the flow, gas will pile up in a hydrostatic core, surrounded by an accretion shock. The density distribution in the core (assuming $u \simeq 0$ here) is

$$\rho = \rho_s \exp \left[\left(\frac{v_K^2}{2c^2} \right) (x_s^2 - x^2) \right], \quad (B9)$$

where ρ_s, x_s are the values just inside at the accretion shock. These may be found, at any time, by equating $\rho_s c^2$ with the ram pressure of the accretion flow, ρv^2 , and by setting the mass accumulated in the core equal to the total mass input prior to t :

$$\frac{4\pi}{3} r_c^3 \dot{q} t \simeq r_c^3 \int_0^{x_s} \rho(x) 4\pi x^2 dx. \quad (B10)$$

The fit between equations (B8) and (B9) and the time-dependent numerical model, Model \mathcal{O} above, is illustrated in Fig. B1.

Together, these equations (B9 and B10) give the time at which the accretion shock reaches $x_s, t(x_s)$, as a function of m_K . The function $t(x_s)$ is zero at $x_s = 0$ and $x_s = 1$, with a maximum at $t = t_{\text{merge}}$ at a value of x_s close to the edge of the stellar cluster for large m_K . At times later than t_{merge} , the inner sonic point merges with the accretion shock, and supersonic inflow ceases. After this time, the stagnation radius begins to move inwards within the cluster (when equilibrium is finally reached, the stagnation radius is at the centre of the cluster).

For large m_K , the timescale over which the hydrostatic core fills the central stellar cluster can be approximated by

$$t_{\text{fill}} \simeq 3\sqrt{2\pi} t_K e^{m_K^2/2} / m_K^3, \quad (B11)$$

where $t_K = r_c/v_K$ is the free-fall timescale within the stellar cluster. When $m_K = 3$, the filling timescale is roughly 25 times the free-fall timescale, rising to roughly 350 times for $m_K = 4$ and very rapidly thereafter. A yet longer time, roughly $4t_K/m_K^5 e^{m_K^2/2}$, is then taken to fill the region beyond the cluster core out to the outer sonic radius, $r_c m_K^2/2$.

Only after this time, far longer than any of the obvious dynamical timescales, is equilibrium finally achieved throughout the subsonic region. The wind through the sonic radius, which has gradually been strengthening, then removes a mass flux equal to the mass input in the core.

This paper has been produced using the Royal Astronomical Society/Blackwell Science L^AT_EX style file.